学位論文

Search for hidden photon cold dark matter in sub-meV range
by using a millimeter-wave spectrometer

（ミリ波スペクトロメータを用いた
sub-meV 領域における Hidden Photon Cold Dark Matter 探索 ）

平成 28 年 12 月　博士（理学）申請

東京大学大学院理学系研究科
物理学専攻

富田望

Search for hidden photon cold dark matter in sub-meV range by using a millimeter-wave spectrometer

Nozomu Tomita

Department of Physics, School of Science,
University of Tokyo

February 8, 2017

Abstract

We searched for hidden photon cold dark matter at 115.79 μeV – 115.84 μeV mass region based on a dish antenna method. We achieved a sensitivity to exceed the cosmological constraints based on a combination of a cryogenic receiver and a condition of small thermal radiation under the atmospheric radiation. We detected no signal in data sets of 9.3 hours with 26 cm^2 aperture. We set upper limits $\chi < 1.5 - 3.9 \times 10^{-10}$ at 95% confidence level. This is the most stringent limit to date at this mass range.

Contents

Chapter 1

Introduction

To reveal properties of cold dark matter is one of the most important subjects in both the fields of particle physics and the cosmology. Experimental results today determine that its composition in the universe is one forth of total energy budget [1]. We also understand the dark matter is the dominant gravity source in galaxies, i.e. it is massive particle and its momentum is in equilibrium state in the current universe [2]. Experimental searches for heavy mass candidates at least above MeV scale, Weakly Interacting Massive Particles (WIMPs), have been major research topic. However, there is no convincing results yet [3]. Light mass particles, Weakly Interacting Slim Particles (WISPs), are recently suggested, and many experimental efforts are ongoing [4].

This thesis focuses on "hidden photon", one of the WISP candidates. The misalignment mechanism allows the hidden photon becomes to be the cold dark matter [5]. The hidden photon weakly couples with the electromagnetic field. This coupling results in a transition from the hidden photon to the ordinary photon and the opposite transition. Cosmological observations such as a blackbody spectrum of cosmic microwave background radiation (CMB) and astronomical knowledge like the age of the Sun give constraints for its coupling with ordinal photons as a function of its mass. Thus far, experimental upper limits which exceed the the cosmological constraints are given at the mass region from 10^{-6} eV to 10^{-4} eV. Our experiment is the first experiment to exceed the cosmological constraints at 115.79 μeV – 115.84 μeV region based on a dish antenna method [6]. A combination of a plane mirror and a parabolic antenna is recently suggested[7, 8]. Similar to this, we employ a method with a combination of the plane plate and a horn antenna. To achieve a low system noise, we use a cryogenic receiver under the atmospheric radiation. An effective radiation temperature at this frequency range is low ($\sim$ 100 K). It results in low thermal noise condition compared

with the setup under the radiation of room temperature. photon search.

The structure of this thesis is as follows. In Chapter 2, we describe details of the hidden photon. Motivations for the particle physics as well as the properties as the cold dark matter candidate are discussed. We review direct detection methods for the hidden photon cold dark matter (hereafter, HPCDM). Their search results are also reviewed. In Chapter 3, we describe details of our experimental setup. In Chapter 4, we define our data sets as well as measurement condition. We also explain about basic treatments prior to analysis. In Chapter 5, we describe details of calibrations. In Chapter 6 we explain methodology of analysis including validation tests and systematic error studies. In Chapter 7, we show our results. We conclude in Chapter 8.

Chapter 2

Hidden photon cold dark matter

2.1 Existence of cold dark matter

There are cosmological observations that conclude the existence of the cold dark matter. Its classical evidence is a homogeneous speed of galaxy rotation as a function of distance from each center. The velocity $v(r)$ of objects (stars and gases) in the galaxy should follow Newtonian mechanics,

$$v(r)^2 = G\frac{M(r)}{r}, \tag{2.1}$$

where $M(r)$ is the total mass within the radius r and G is the gravitational constant. We expect simple relation; $v(r) \propto r^{-1/2}$. However, measured velocity curve is flat up to far outside of the visible components as shown in Fig. 2.1. This results lead an interesting conclusion, there should be invisible massive halo in the galaxy. Density distribution of the halo is $\rho \propto r^{-2}$. Therefore, it satisfies the observed results, $M \propto r$.

Our galaxy also has a halo, and a recent analysis [9] shows the density of cold dark matter near the Solar system is

$$\rho_{\mathrm{CDM}}^{\mathrm{local}} = (0.39 \pm 0.03)\frac{\mathrm{GeV}}{\mathrm{cm}^3}. \tag{2.2}$$

2.2 Hidden photon

2.2.1 Theoretical motivation of hidden photon

The standard model in the particle physics precisely explains many experimental results. Despite of its remarkable success, it is not ultimate theory

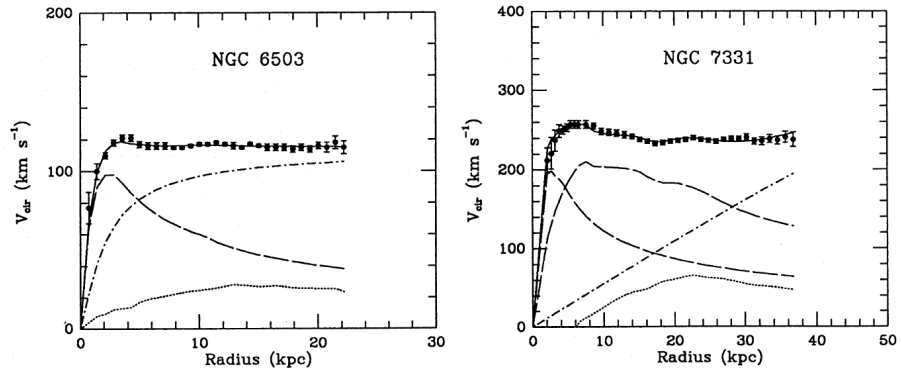

Figure 2.1: Rotational speeds of spiral galaxies as a function of radius. Points are observational results, and solid line is a fitted result with floating compositions of matters: visible star, gas, and dark matter halo. Curves for each component are shown with dash-dot line (the dark matter halo), dashed line (visible components), and dot line (gas). They are taken from [2].

because it does not explain the existence of the dark matter, strong CP problem and so on. Therefore, various extensions of the standard model have been proposed to solve these issues. In the many extension theories, an extra $U(1)$ symmetry frequently arises. This symmetry should be in a hidden sector because we do not observe its contribution. The gauge boson corresponding to this hidden sector symmetry is referred to as hidden photon, para photon, dark photon, or sterile photon. The hidden photon was originally proposed by Okun as a test of electromagnetic force [10]. Then, Holdom discussed its mixing with ordinary photon through mediation of fermions [11]. This model is represented by the following lagrangian:

$$\mathcal{L} = -\frac{1}{4}F_{\mu\nu}F^{\mu\nu} - \frac{1}{4}X_{\mu\nu}X^{\mu\nu} + \frac{m_{\gamma'}^2}{2}X_\mu X^\mu - \frac{\chi}{2}F_{\mu\nu}X^{\mu\nu} + J^\mu A_\mu, \qquad (2.3)$$

where A_μ and $F_{\mu\nu}$ are ordinary photon field and field strength, X_μ is the hidden photon field, $X_{\mu\nu} = \partial_\mu X_\nu - \partial_\mu X_\mu$ is strength of the hidden photon field, χ is a dimensionless parameter describing kinetic mixing, $m_{\gamma'}$ is the mass of the hidden photon, and J^μ is the ordinary electromagnetic current. There are two additional parameters to the standard model, i.e. $m_{\gamma'}$ and χ. Higgs mechanism or Stückelberg mechanism explains the mechanism of its mass generation. Preferred mass range in the string theory with the Stückelberg mechanism is typically $\gtrsim 10^{-4}$ eV [4]. The kinetic mixing term $-\frac{\chi}{2}F_{\mu\nu}X^{\mu\nu}$ is generated from a one-loop contribution from heavy mass messengers which have both of ordinary and hidden $U(1)$ charges.

We can choose bases eliminating the kinetic mixing term by following re-definitions,

$$(1) \quad A \to \tilde{A}^\mu - \chi X^\mu, \tag{2.4}$$

$$(2) \quad X^\mu \to \tilde{X} - \chi A^\mu. \tag{2.5}$$

Each of them provides two different physical pictures described in following subsections.

2.2.2 Picture (1): Mass basis

The equation (2.4) results in the following Lagrangian.

$$\mathcal{L} = -\frac{1}{4}\tilde{F}_{\mu\nu}\tilde{F}^{\mu\nu} - \frac{1}{4}X_{\mu\nu}X^{\mu\nu} + \frac{m_{\gamma'}^2}{2}X_\mu X^\mu + J^\mu(\tilde{A}_\mu - \chi X_\mu). \tag{2.6}$$

In this picture, $\tilde{A}$ and X are the massless and massive states, The hidden photon field (X) interacts with the ordinary matter through the term $-\chi J^\mu X_\mu$. This massive boson field modifies the Coulomb potential in short distance approximately below $1/m_{\gamma'}$. Tests for this effect exclude the hidden photon parameter region as shown in Fig. 2.3.

2.2.3 Picture (2): Interaction basis

The equation (2.5) results in the following Lagrangian.

$$\mathcal{L} = -\frac{1}{4}F_{\mu\nu}F^{\mu\nu} - \frac{1}{4}\tilde{X}_{\mu\nu}\tilde{X}^{\mu\nu} + \frac{m_{\gamma'}^2}{2}(\tilde{X}_\mu^\mu - 2\chi A_\mu\tilde{X}^\mu + \chi^2 A_\mu A^\mu) + J^\mu A_\mu. \tag{2.7}$$

A and $\tilde{X}$ are identified to be fields with and without interaction with ordinary matter in this picture. The mass term is not diagonal in this picture. This means oscillation between these two states along propagation similar to neutrino oscillation. Experimental approach to search for the hidden photon is detection of the ordinal photon generated from this mixing.

LSW (Light Shining through a Wall) experiments, schematically shown in Fig. 2.2, use a intense source of the ordinary photon. A part of the photons oscillates to the hidden sector ($\tilde{X}$) at an upstream of the wall. The oscillated hidden particles through the wall oscillate to the ordinal photons, again. The detection of regenerated photons is an evidence of the hidden photon. The most stringent limit by this method is given by ALPS[12] as shown in Fig.2.3.

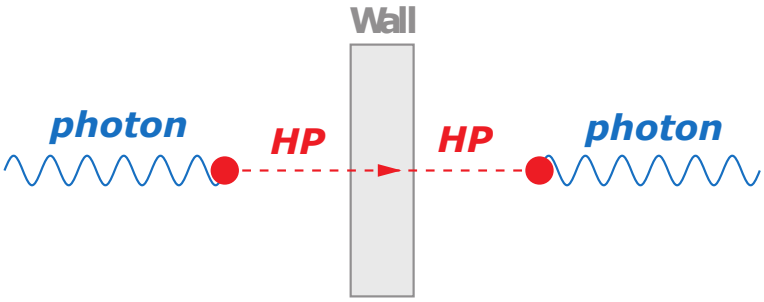

Figure 2.2: Schematic of LSW experiments. Taken from [13].

Helioscope experiments use the Sun as a source of hidden photon. An effective mass caused by plasma in the Sun generates the hidden photon. Experiments in this method, include SHIPS[14], CAST[15, 16](results translated from axion search), and Tokyo[17, 18](the first experiment for solar hidden photon search), give limits as shown in Fig.2.3.

The lifetime of the Sun also set constraint for the hidden photon. A coincidence between the effective mass of the ordinal photon and the hidden photon mass enhances their oscillation. WIMP search experiments with low energy threshold also give constraint to the hidden photon from the Sun [19, 20, 21].

2.3 Hidden photon as a dark matter candidate

2.3.1 Generation scenarios as Cold Dark Matter

The possibility of hidden photon as the cold dark matter (hereafter HPCDM) is pointed out by several authors[24, 4]. Constraints assuming the dark matter is dominated by the hidden photon are shown in Fig. 2.4. In this allowed region, the thermal production scenario makes inconsistency of the cold condition (i.e., non-relativistic momentum). One of possible scenarios of non-thermal generation is the misalignment mechanism. A field which has random initial value was frozen at the early stage of the universe . This field is expanded from small patch into large volume. This is the same scenario as axion dark matter [4].

Another possibility for non thermal scenario is proposed recently gravitational generation of hidden photon [25]. This scenario explains abundance of HPCDM mass ($m_{\gamma'}$) by Hubble scale at inflation era (H_I), $m_{\gamma'} \approx 10^{-5}\mathrm{eV} \times (10^{14}\mathrm{GeV}/H_I)^4$. Current constraint for H_I favor $m_{\gamma'} \gtrsim 10^{-5}$ eV.

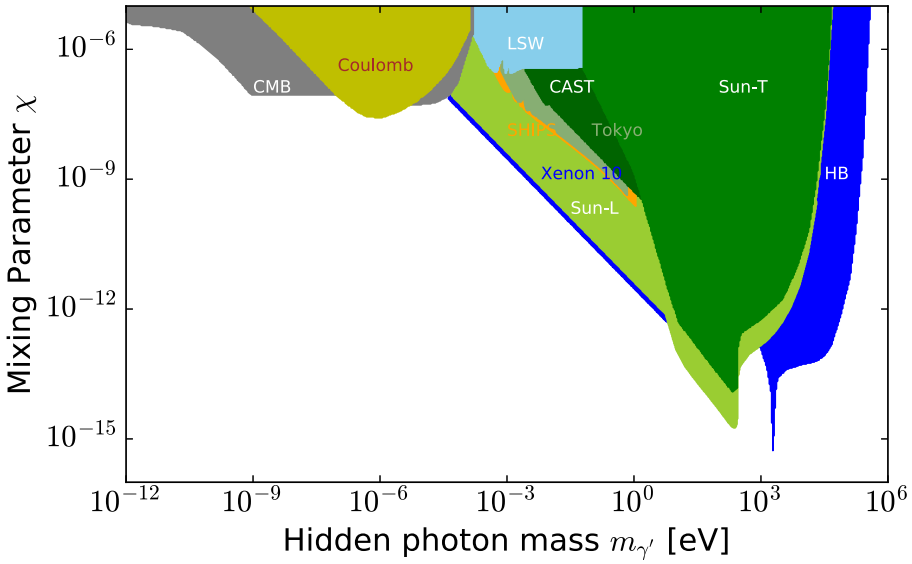

Figure 2.3: The regions and current limits for hidden photon parameter space. The region denoted as "Coulomb" excluded by experiments examining Coulomb law precisely. The region "LSW" is excluded by LSW experiment. "Sun-T" is excluded when considering only contribution from transverse modes of hidden photon, whereas "Sun-L" is the excluded region when longitudinal mode is also considered[22, 23]. "HB" is the region excluded from the lifetime of stars of horizontal branch. "CAST", "Tokyo", "SHIPS" are region excluded from helioscope experiments. "CMB" is the region excluded from observation of CMB spectrum.

Note that, although this scenario generates longitudinal mode, the relation between the momentum direction and polarization is lost because the momentum direction is determined by the gravitational potential. In this scenario, the detection of HPCDM implies the existence of the cosmic inflation.

2.3.2 Constraints from cosmological and astronomical observations

Universe was in plasma state in its early age. The ordinary photons have effective mass m_γ in plasma, and their conversion to the hidden photons is enhanced in the condition of $m_\gamma \simeq m_{\gamma'}$. This condition generates additional number of the ordinal photons from the initial HPCDM. This effect should make deviations in various cosmological observations. The effective number

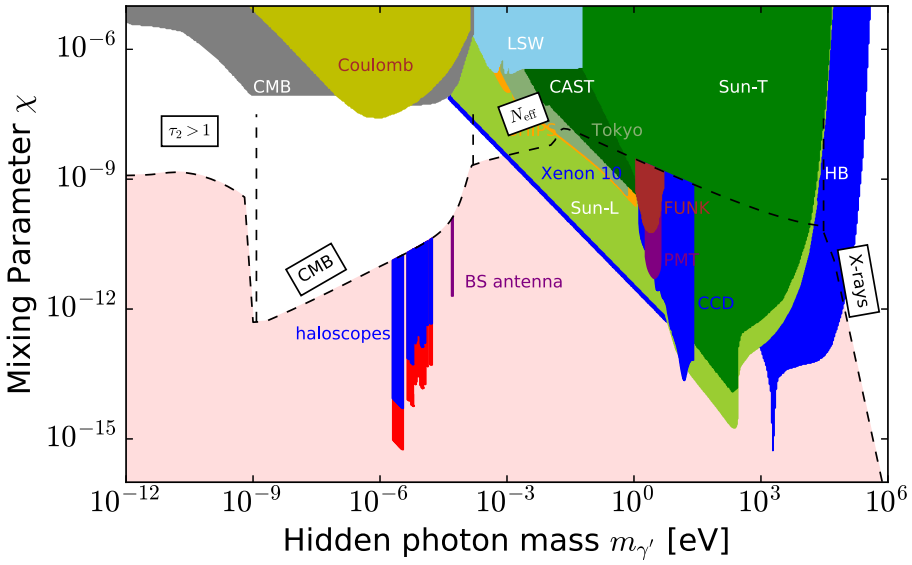

Figure 2.4: Constrains for HPCDM parameters. The region shaded pink represents the space where hidden photon can be the main component of dark matter. Regions designated as "BS antenna"[8, 7, 26], "PMT"[27, 7], and "FUNK"[28] is region excluded using dish antenna method. "CCD" is excluded using the experiment of photo-electric-type effect. "Haloscope"2.4 is the limit translated from cavity experiments.

of relativistic neutrino species $N_{\rm eff}$, and the CMB spectrum distortion give constraints shown in Fig. 2.4. In case of $m_{\gamma'} < 10^{-9}$ eV, this effect happened after the recombination era. On the other hand, HPCDM decays into three photons if hidden photon is heavy ($\gg 10^4$ eV) [29]. Observation of the diffuse X-ray background constraints for this scenario. These constraints are also shown in Fig. 2.4.

2.4 Direct search for hidden photon cold dark matter by dish antenna method

2.4.1 Dish antenna method principle

Detection of HPCDM by using dish antenna is proposed by Horns[6]. We explain the principle based on the lagrangian Eq. (2.7). Assuming the plane

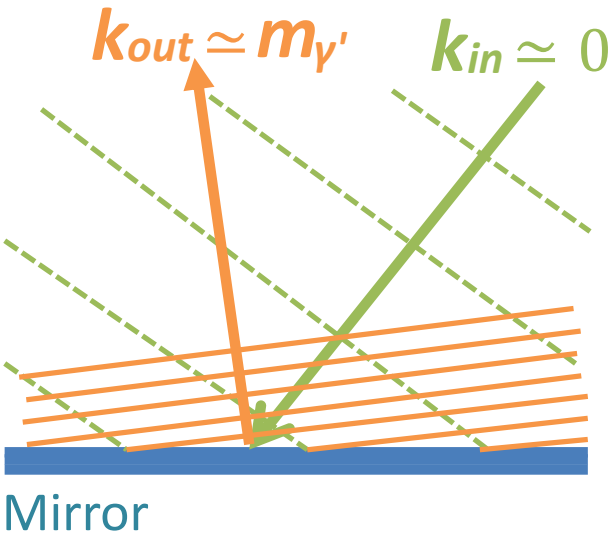

Figure 2.5: Schematic for reason of near-perpendicular emission of conversion photon. The four momentum conservation causes the direction of a converted photon almost perpendicular to the mirror surface.

wave solution, the equation of motion derived from the lagrangian is,

$$\left[(\omega^2 - k^2)\begin{pmatrix}1 & 0\\ 0 & 1\end{pmatrix} - m_{\gamma'}^2\begin{pmatrix}\chi^2 & -\chi\\ -\chi & 1\end{pmatrix}\right]\begin{pmatrix}\mathbf{A}\\ \tilde{\mathbf{X}}\end{pmatrix} = \begin{pmatrix}0\\ 0\end{pmatrix}, \tag{2.8}$$

where ω is frequency and k is momentum. Since HPCDM is non-relativistic ($k \ll \omega$), we can take suitable gauge choice and neglect the 0th component[30]. We obtain $A^0 \approx X^0 \approx 0$ by choosing Lorenz gauge ($\partial_\mu A^\mu = 0$ and $\partial_\mu X^\mu = 0$, hence $A^0 = \mathbf{k}\cdot\mathbf{A}/\omega$ and $X^0 = \mathbf{k}\cdot\mathbf{X}/\omega$).

This equation has two nontrivial solutions. The massive one ($\omega = \sqrt{m_{\gamma'}^2 + \mathbf{k}^2}$) corresponds to the dark matter state (DM):

$$\left.\begin{pmatrix}\mathbf{A}\\ \tilde{\mathbf{X}}\end{pmatrix}\right|_{\mathrm{DM}} = \tilde{\mathbf{X}}_{\mathrm{DM}}\begin{pmatrix}-\chi\\ 1\end{pmatrix}\exp(-i\omega(\omega t - \mathbf{kx})). \tag{2.9}$$

For the case of the misalignment mechanism described in Sec. 2.3.1, the direction of the generated HPCDM field $\mathbf{X}_{\mathrm{DM}}$ is the same everywhere. However, The direction might be influenced by the structure formation[4]. Two possibilities for the direction can be considered.

(i) $\mathbf{X}_{\mathrm{DM}}$ has the same orientation everywhere.

(ii) $\mathbf{X}_{\mathrm{DM}}$ is random in its direction.

In this thesis we assume the case (ii). The same argument also applies for the gravitational scenario, because HPCDM is generated before structure formation. Assuming hidden photon is the main component of dark matter, we find

$$\rho_{\rm HP} = \frac{m_{\gamma'}^2}{2}\langle|\tilde{\mathbf{X}}_{\rm DM}^2|\rangle = \rho_{\rm CDM}^{\rm local} = (0.39 \pm 0.03)\ {\rm GeV/cm^3}, \tag{2.10}$$

where we use the value of Eq. 2.2 for $\rho_{\rm CDM}^{\rm local}$. This dark matter component has small electromagnetic field,

$$\mathbf{E}_{\rm DM} = -\partial_0 X_{\rm DM} = \chi m_{\gamma'}\tilde{\mathbf{X}}_{\mathbf{DM}}. \tag{2.11}$$

Combining Eq. (2.10) and (2.11), we obtain the amplitude of electric field from HPCDM, which can be used for experimental search.

$$\sqrt{\langle|\mathbf{E}_{\rm DM}|^2\rangle} = \chi\sqrt{2\rho_{\rm CDM}^{\rm local}} \sim 3.3\times10^{-9}\frac{\rm V}{\rm m}\left(\frac{\chi}{10^{-12}}\right)\left(\frac{\rho_{\rm CDM}^{\rm local}}{0.3{\rm GeV/cm^3}}\right). \tag{2.12}$$

To explain experimental method using dish antenna, let us assume we have a highly conductive surface at $z = 0$. Then the boundary condition on the plane is given by

$$\mathbf{E}_{\parallel} = 0, \tag{2.13}$$

where the suffix $\parallel$ means directions parallel to the plane. As a result, an ordinary electric field with the same frequency ω is required:

$$\begin{pmatrix}\mathbf{E}\\ \mathbf{E}_{\rm hid}\end{pmatrix}_{\rm out} = \mathbf{E}_{{\rm DM},\parallel}\exp\left(-i(\omega t - \mathbf{px})\right)\begin{pmatrix}1\\ \chi\end{pmatrix}. \tag{2.14}$$

Then the boundary condition

$$\begin{pmatrix}\mathbf{E}\\ \mathbf{E}_{\rm hid}\end{pmatrix}_{\rm total,\parallel} = \mathbf{E}_{{\rm DM},\parallel}\left[\begin{pmatrix}1\\ \chi\end{pmatrix}\exp(-i(\omega t - \mathbf{px})) + \frac{1}{\chi}\begin{pmatrix}-\chi\\ 1\end{pmatrix}\exp(-i(\omega t - \mathbf{kx}))\right]|_{z=0} \tag{2.15}$$

$$= \mathbf{E}_{{\rm DM},\parallel}\frac{1}{\chi}\begin{pmatrix}0\\ 1\end{pmatrix}. \tag{2.16}$$

From this we obtain

$$\mathbf{p}\cdot\mathbf{x}|_{z=0} = \mathbf{k}\cdot\mathbf{x}|_{z=0} \tag{2.17}$$

$$\Leftrightarrow \mathbf{p}_{\parallel} = \mathbf{k}_{\parallel}. \tag{2.18}$$

We determined two components of the momentum for the conversion photon. The remaining components is determined from energy conservation

$$|\mathbf{p}| = \omega = \sqrt{m_{\gamma'} + \mathbf{k}^2}. \tag{2.19}$$

Therefore we arrive to the formula

$$\mathbf{p} = \sqrt{m_{\gamma'}^2 + \mathbf{k}_\perp^2}\mathbf{n} + \mathbf{k}_\parallel \tag{2.20}$$

where $\mathbf{k}$ is the perpendicular component of $\mathbf{k}$ to the mirror, and $\mathbf{n}$ is a unit vector of the same direction as $\mathbf{k}$. The outgoing wave is nearly perpendicular to the surface, because HPCDM is non-relativistic. By using a spherical reflector, the emitted waves can be focused to the center of the sphere, as shown in Fig. 2.6. The concentrated power is

$$P_{\text{center}} \approx \langle |\mathbf{E}_{\text{DM},\parallel}|^2 \rangle \langle \alpha^2 \rangle_{\text{dish}} \chi^2 \rho_{\text{CDM}}^{\text{local}} A_{\text{dish}}, \tag{2.21}$$

where A_{dish} is the area of dish, and $\alpha = \cos\theta$ with θ is the angle between $\mathbf{n}$ and $\mathbf{E}_{\text{DM}}$. We assume the case (ii), which means $\alpha = \sqrt{2/3}$. From Eq. (2.12) and (2.21), we measure $\mathbf{X}_{\text{DM}}$ as follows,

$$\chi = 4.5 \times 10^{-14} \left(\frac{P_{\text{det}}}{10^{-23}\text{W}}\right)^{1/2} \left(\frac{0.3\text{GeV/cm}^3}{\rho_{\text{CDM,halo}}}\right)^{1/2} \left(\frac{1\text{m}^2}{A_{\text{dish}}}\right)^{1/2} \left(\frac{\sqrt{2/3}}{\alpha}\right), \tag{2.22}$$

where P_{det} is the detected power. The uncertainty of the detected power (ΔP_{det}) determines the sensitivity for χ. This uncertainty is proportional to the noise equivalent power of the system (NEP), and it is also inversely proportional to the square root of observation time (t), i.e., $\Delta P_{\text{det}} \propto \text{NEP}/\sqrt{t}$.

2.4.2 Methodology of the experiment

An experimental search for HPCDM using the dish method were carried out by Horie. et al [8, 7, 26], where a large parabolic antenna for satellite broadcast reception was used to search HPCDM at the mass region around 50 μeV.

Set up

A spherical antenna is not commercially readily available in BS or CS region. To overcome this problem, they invented a method of using a parabolic antenna which is more easily available. The method is shown schematically in

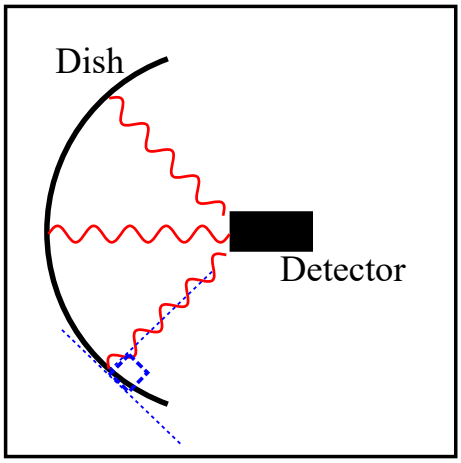

Figure 2.6: Schematic of the original dish antenna method proposed by Horns. The converted photons are emitted perpendicular to the mirror surface, focusing to the center of the dish.

Fig. 2.7. In this method, an plane mirror is used as a plane wave source which converts HPCDM to ordinary photons. Then a parabola antenna is used only for collecting the outgoing wave. Figure 2.8 shows the pictures of the setup of this experiment, including a plane mirror (upper left), a parabolic antenna (upper right), and the frame for combining and fixing their relative positions (bottom). 4 aluminum plates were combined to form a reflector as a plane wave source. The flatness of the plates are confirmed using a theodolite. The parabolic antenna is 2.2 m diameter and 77 cm. Its gain was calibrated using the intensity of satellite broadcast signal, and the result agrees with the value provided by the manufacturer. A low noise block down-converter with feed horn (Norsat 4506B, Fig. 2.9) was employed as receiver. The receiver accepts 12.25 GHz to 12.75 GHz and down convert the signal to 950 –1450 MHz. The amplifier gain of the receiver was calibrated using a ECCOSORB AN-73 as a blackbody source. The down-converted signal were feeded to a signal analyzer (FSU-4, Rohde&Schwarz).

Measurement

As described in Sec. 3.1., the signal from HPCDM have a frequency of $\omega \sim m_{\gamma'}$, and its width is $\Delta\nu/\nu \sim O(10^{-6})$. The resolution of spectrum analyzer was set to resolve this signal shape effectively.

The measurement was carried out from November 24th to 28th, 2014. They found no peak except for spurious peaks which are not from HPCDM. To examine if the spurious peaks are HPCDM origin, they carried out mea-

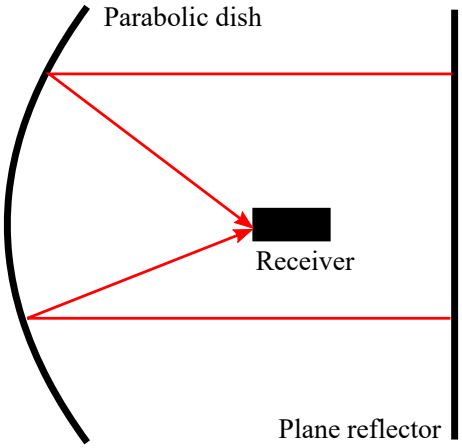

Figure 2.7: The method employed by Horie et al. Converted photons are emitted from a plane mirror and collected using a parabola antenna.

surement changing the distance between the mirror and parabola antenna and checked if the peaks appear at the same position. The result is shown in Fig. 2.4 designated as "BS antenna".

Figure 2.4 also shows upper limits of experiments which employ this method [27, 7, 28].

2.5 Other experimental limits

Microwave cavity

The haloscope results for axion can be translated into that of hidden photon [4]. The constraints is shown in Fig. 2.4, in red and blue regions. The red part assumes random direction of HPCDM, and the blue part assumes fixed direction of HPCDM.

Photoelectric type effect

Contrary to the case of dish antenna method, where material with good conductivity is used, HPCDM also interacts with lossy material in a manner of photoelectric effect. A search using CCD[31] excludes $m_{\gamma'} \sim 10$ eV region as shown in Fig. 2.4.

Hidden photon "radio" in future

Another method, hidden photon "radio" is proposed[32, 33]. This method amplifies the signal using a LC resonator. The prospects of the sensitivity is

Figure 2.8: The set up of the HPCDM search experiment by Horie et al. A plane mirror (upper left) was made of 4 pieces aluminum plate. A parabola antenna (upper right) is used for collecting converted plane wave from the mirror. They are combined in HPCDM search measurement (bottom).

Figure 2.9: The block converter (Norsat 4506B) which was used as receiver in the experiment by Horie et al.

shown in Fig. 2.10.

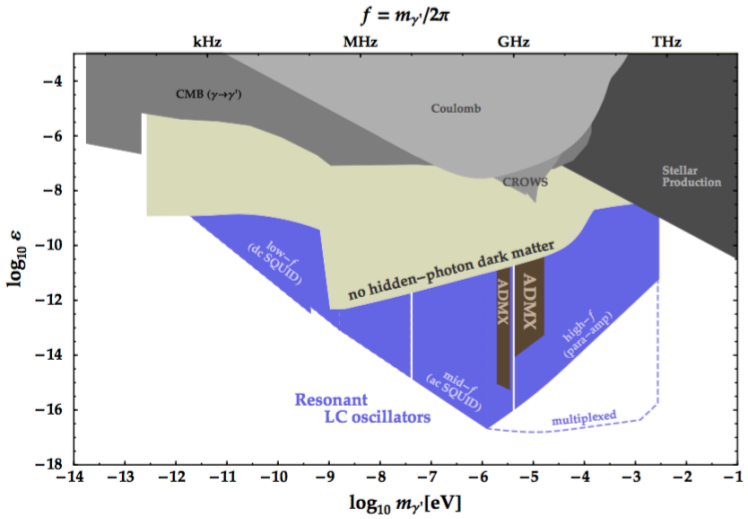

Figure 2.10: The expected sensitivity of HPCDM search using LC circuit [33].

Chapter 3

Overview of experiment and instruments

We employ the dish antenna method similar to that of Horie et al. (described in Sec. 2.4.2). We use a plane mirror for conversion of HPCDM to ordinal photons as shown in Fig. 3.1. We achieve a low noise condition using a cryogenic receiver under the blue sky.

We search HPCDM in the mass range just above 10^{-4} eV, which is higher than $\sim 5 \times 10^{-5}$eV of Horie et al. This mass region is interesting in some models. String theory with Stückelberg mass typically favors $m_{\gamma'} \gtrsim 10^{-4}$ eV (as noted in Sec. 2.2.1). In addition, in gravitational production scenario of HPCDM limits $m_{\gamma'} \gtrsim 10^{-5}$eV (Sec. 2.3.1). In this mass region upper limit for mixing angle ($\chi \sim 10^{-9}$ at 95% C.L.) comes from observation of CMB spectrum.

In this chapter, we first discuss the spectral shape of the signal converted from HPCDM. Then, we introduce our experimental briefly, then in detail.

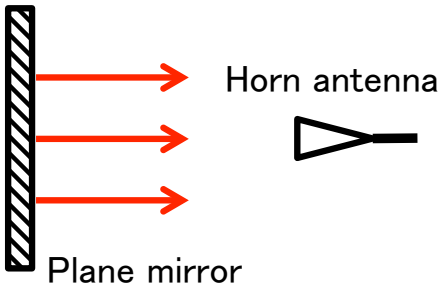

Figure 3.1: The method of our experiment. A plane mirror emits converted photons as plane wave. A horn antenna collects the emitted photons.

3.1 The distribution function of HPCDM signal

Photons converted from HPCDM have a sharp distribution because of low velocity ($\beta \simeq 10^{-3}$). Its distribution is calculated with HPCDM mass ($m_{\gamma'}$) and their speed. We assume the velocity distribution obeys the Maxwell-Boltzmann distribution (isothermal model) with the velocity dispersion v_0, with an offset of the Earth's velocity v_E relative to the dark matter halo:

$$f_{\mathrm{MB}}(\mathbf{v}, \mathbf{v}_E) = \frac{1}{(\pi v_0)^{3/2}} e^{-|\mathbf{v}+\mathbf{v}_E|^2/v_0^2}. \tag{3.1}$$

The value of v_0 is discussed in several literatures[34, 35]. We took v_0 as 220km/s, which is commonly used value. The velocity of Earth v_E can be described by

$$|\mathbf{v}_E| = v_\odot + v_{\mathrm{orb}} \cos\gamma \cos(\Omega t), \tag{3.2}$$

where $v_\odot$ is the solar system velocity the $\gamma \simeq 60^\circ$ is the inclination angle of the plane of earth orbit between the galactic plane, $\Omega = 2\pi/\mathrm{year}$, t is the time from June 2nd in years. In case of our measurement, we use the value for 26th Oct. 2016,

$$v_E \simeq 220\mathrm{km/s} \tag{3.3}$$

throughout the analysis. The photon converted from HPCDM with velocity v_{DM} have frequency of

$$\nu(v_{\mathrm{DM}}, m_{\gamma'}) = \frac{1}{h} \frac{m_{\gamma'}}{\sqrt{1 + (v_{\mathrm{DM}}/c)^2}}. \tag{3.4}$$

Combining Eq. 3.4 and 3.1 we obtain a narrow peak in frequency starting at ν_0 and width of about $(v_0/c)^2 = O(10^{-6})$, as shown in Fig. 3.2. The hidden photon mass of our interest $m_{\gamma'} \sim 10^{-4}$ corresponds to $\nu_0 = 20$–30 GHz (0.8–1.2×10^{-4} eV).

3.2 Experiment overview

As described in the previous chapter, HPCDM is converted into the ordinal photons at the surface of a metal mirror. The generated plane wave is expected to be very faint. Therefore, we have to gather and amplify the signal for its detection. Because HPCDM has small momentum distribution (we

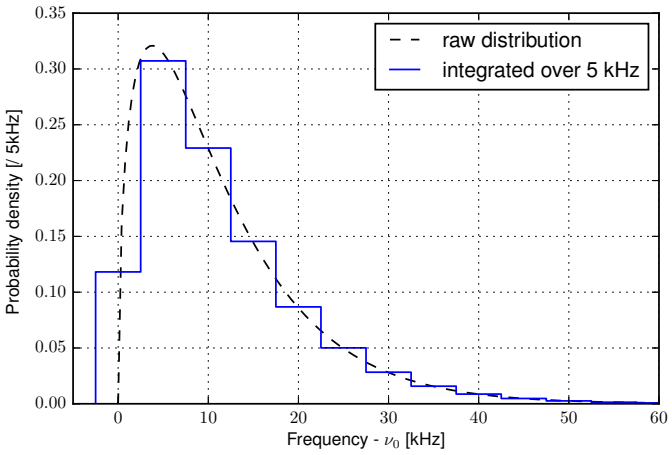

Figure 3.2: The peak shape of HPCDM signal. The black dashed curve is the distribution assuming isothermal model. The blue solid line shows histogram integrated over 5 kHz, which is used for fitting. $\nu_0 = 28.003$ GHz is assumed in this plot.

assume isothermal model), the conversion signal has sharp ($\sim$ 100 kHz) distribution as a function of electromagnetic wave frequency with corresponding peak at the mass of HP. Power spectrum measurements provides us high signal to noise ratio. We extract the power of the converted photon for each frequency by using a fit for corresponding HPCDM mass and its momentum distribution. The schematics of apparatus is shown in Fig. 3.3. The faint conversion signal from the mirror is collected by a horn antenna, then amplified by a low-noise cryogenic amplifier, and further amplified a room-temperature amplifier. Finally the power spectrum of the signal is measured by a signal analyzer.

Our measurement apparatus locates at the rooftop of Building No.4 of KEK, at East longitude 140°04′26″, North latitude 36°08′53″. The mirror is aligned horizontally. We explain each of these components further in this section.

3.3 HPCDM to photon converter

3.3.1 Mirror material

For the conversion of ordinal photons from HPCDM, we need a mirror which is high conductivity (i.e., high reflectance) and thin skin depth material.

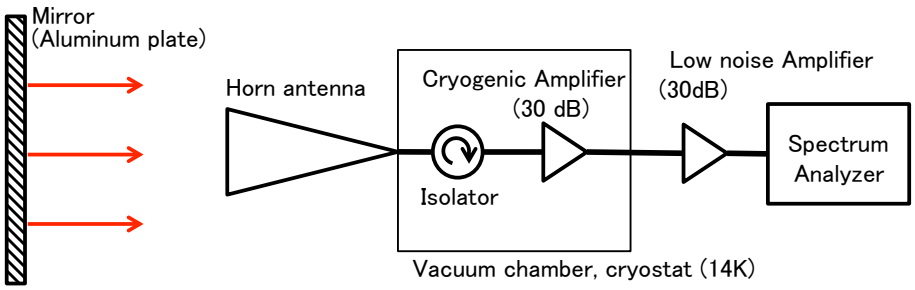

Figure 3.3: Schematics of the experiment setup. The mirror converts HPCDM to ordinary photons. The converted photons are coherent over the mirror plane (because mirror is smaller than HPCDM coherent length ~ 10 m), resulting in plane wave. This plane wave is collected using a horn antenna. The collected power is amplified by a cryogenic low-noise amplifier. Then it is further amplified by a room-temperature amplifier, and the power spectrum of the signal is measured by a spectrum analyzer. The measured spectrum is fit by a peak shape at hidden photon mass $m_{\gamma'}c^2/h$. As the mass is unknown, this fitting is tried changing the assumed mass, within the measured frequency range.

We choose an aluminum plate (500 mm $\times$ 500 mm $\times$ 6 mm, A5052-H112 purchased from MISUMI) shown in Fig. 3.4. The reflectance ($P_{\rm ref}$) and skin depth (δ) at a conductive surface are approximated as follows,

$$P_{\rm ref} \simeq 1 - 4\sqrt{\frac{\pi\nu\varepsilon_0}{\sigma}}, \tag{3.5}$$

$$\delta \simeq \sqrt{\frac{1}{\pi\sigma\nu\mu}}, \tag{3.6}$$

where ν is the frequency of electromagnetic waves, ε_0 is the permittivity in vacuum, σ is conductivity, and μ is magnetic permeability. The conductivity of this plate is $\sigma = 2.03 \times 10^7/\Omega\cdot\mathrm{m}$. By using $\varepsilon_0 = 8.85 \times 10^{-12}\mathrm{F/m}$ and $\mu \simeq \mu_0 = 1.26 \times 10^{-6}\mathrm{A}\cdot\mathrm{m}$, we obtain,

$$1 - P_{\rm ref} = 4\sqrt{\frac{\pi f\varepsilon_0}{\sigma}} \simeq 7.8 \times 10^{-4} \qquad (\text{at } \nu = 28\mathrm{GHz}), \tag{3.7}$$

$$\delta = 6.7 \times 10^{-7}\mathrm{m}. \tag{3.8}$$

The conversion loss of this mirror is at most $7.8 \times 10^{-2}\%$, which is negligible for our experiment.

The conversion photon should be plane waves under a condition that the size of mirror is small compared with the coherent length of hidden

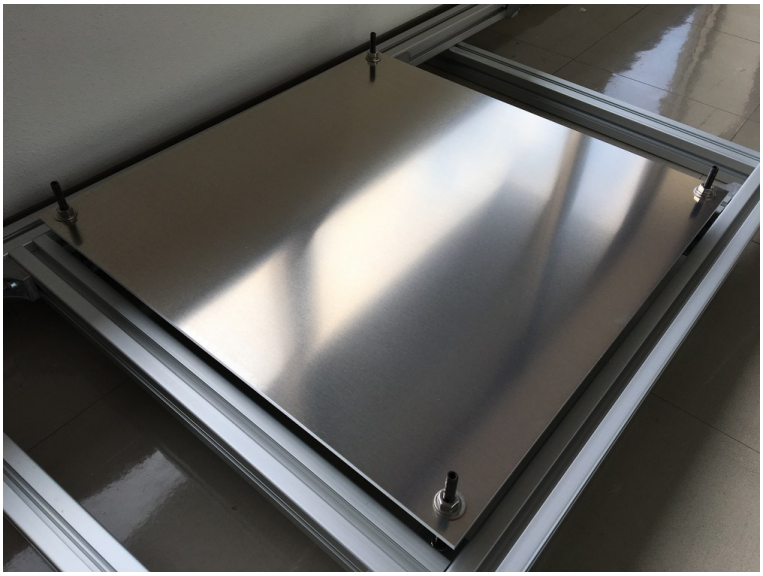

Figure 3.4: The aluminum plate mirror used in our experiment.

photon field. For standard dark matter velocity profile, $v \sim \Delta v \sim 10^{-3}c$, the coherent length of HPCDM is $\lambda_{\rm coherent} \approx \dfrac{1}{\nu v} \approx 100{\rm km} \times (10^{-8}{\rm eV}/m_{\gamma'})$ [33], which is approximately 10 m at ν = 20–30 GHz. Our mirror is 1/20 of the coherent length. Our experiment conserves the condition of the plane wave emission.

3.3.2 Support structure

We construct a support structure of the mirror along the receiver (explained in the next section) as shown in Fig. 3.5. The structure materials are aluminum frames (MISUMI). We set the aluminum plate at its top section. We make 4 holes on the aluminum plate, and we hang the plate using screws and nuts(Fig. 3.6). We align the horn antenna of receiver by using a pocket gradient meter (PL-150, TRUSCO) as shown in Fig. 3.8. This gradient meter has sensitivity of 0.5 mm/m = 0.0286°. Hidden photon has velocity dispersion of $10^{-3}c$, which results in an angular dispersion of 10^{-3}rad = 0.057°. Therefore, alignment precision is sufficient.

Our setup satisfies "far field condition". We do not need to consider effects of standing waves as well as possible interference between the conversion signal from the mirror and the signal from inside of the horn antenna. This condition can be preserved to maintain the distance between the mirror and the antenna is longer than $2D^2/\lambda$ (D is the largest aperture of antenna).

Dimensions of our experiment, $D = 58$mm and $\lambda = 10.7$mm, require the distance more than 670 mm. We take the distance of 1030 ± 9 mm. Here, the uncertainty of the length is incorporated into the calibration uncertainty of an antenna effective area (Sec. 5.2).

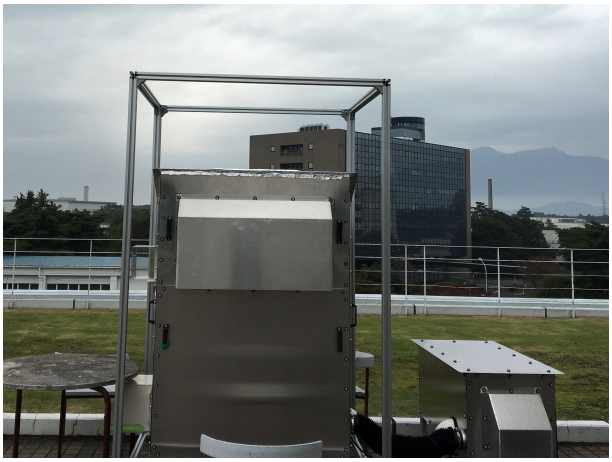

Figure 3.5: Support structure of the mirror above the receiver.

3.4 Cryogenic receiver

We employ a cryogenic receiver for the detection of the faint conversion signal. It has capability to measure the power spectrum as a function of the frequency. In KEK, a low-noise millimeter spectrometer was practically developed, for a meteorological application[36, 37]. It is named KUMODeS (Fig. 3.12). This spectrometer consists of two bands, 20 to 30 GHz and 50 to 60 GHz. KUMODeS measures characteristic spectra of atmospheric radiations from water vapor and Oxygen molecules. We use the system for 20–30 GHz band in our HPCDM experiment. Hereafter, we simply call it "receiver". Its specifications are summarized in Table 3.1. The intrinsic noise level of the system is defined with "receiver temperature" which is defined as an effective intensity of the thermal radiation. Figure 3.13 shows the receiver temperature as a function of frequency. Responsivity of the receiver (amplifier gain) is shown in Fig. 3.14.

3.4.1 Horn antenna

We use a horn antenna SGH-42-SC000 (millitech), to collect plane waves. Its geometry is shown in Fig. 3.20 and typical specifications are summarized

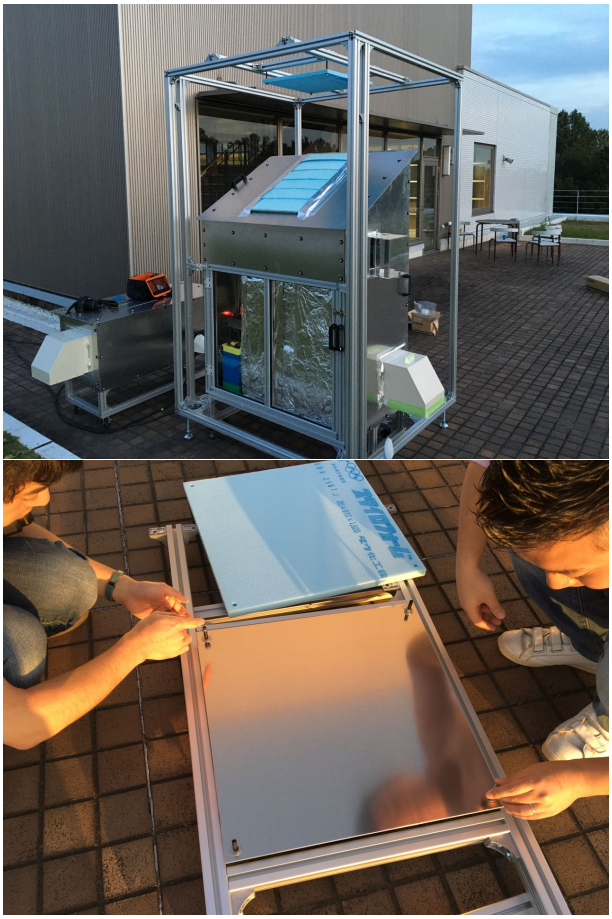

Figure 3.6: The aluminum mirror is hinged above the receiver. We replace the mirror to styrofoam plate for antenna area calibration described in Section 5.2. Plates have four holes at their corners. We used screws and nuts to set them with alignment for their direction to the line of sight of the receiver.

in Table 3.2. "Gain" is the ratio of effective aperture area to that of an ideal isotropic antenna. This term is confusing with the gain of amplifier. Therefore, we use "effective area" ($A_{\rm eff}$) in the following discussion. The effective area of antenna is the power it can collect compared with the power flux it sees. This parameter should be measured to determine the absolute scale of measured flux. Details are described in Sec. 5.2. The antenna has axisymmetric dependence on angle. The "Beam width" is defined as the angle where the power diminishes to half.

Figure 3.7: Photograph for the corner of mirror. It is fixed using a screw and washers and nuts.

Parameter	Value
Frequency range	20 – 30 GHz
Gain	60 dB
Noise temperature	50 K

Table 3.1: Rough characteristics of the receiver.

3.4.2 Amplifiers

We use two amplifiers. The first one is maintained at approximately 10 Kelvin (LNF-LNC15_29A, Low Noise Factory). The second one is maintained at the ambient temperature (ALM-1826S210, ALDETEC). Their specifications are summarized in Tab. 3.4 and 3.5.

3.5 Spectrum analyzer

The amplified signal is measured by using a spectrum analyzer. We use the N9010A, Agilent Technologies shown in Fig. 3.18. Its specification is also summarized in Table 3.6. This spectrum analyzer measures power for each frequency bin based on Fast Fourier Transform method[1]. The time-

[1]The spectrum analyzer has another measurement mode, Swept mode (contrary to FFT mode). However, we do not use this mode because it looses measurement time effectively.

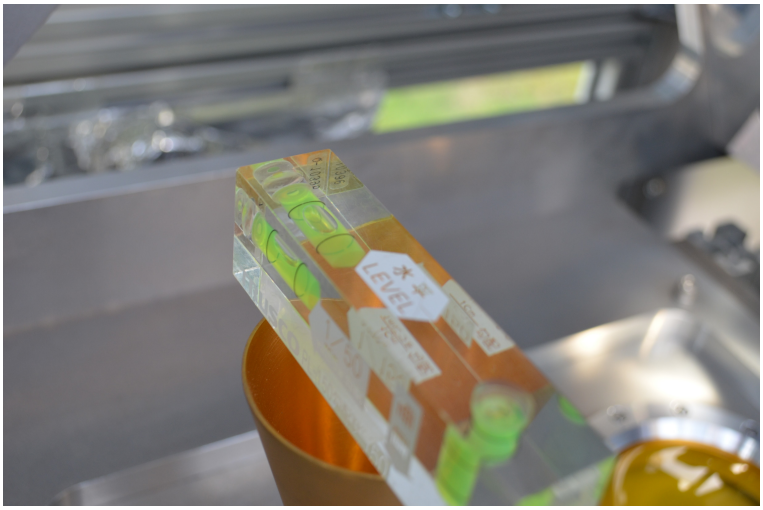

Figure 3.8: We align the direction of horn antenna by using a pocket gradient meter PL-150. We measure gradients in two orthogonal direction. The horn antenna and mirror are separately aligned in horizontal direction within the precision of 0.03°. This is smaller than angular dispersion of signal (0.057°).

Parameter	Value
Frequency range	18-26.5 GHz
Midband gain	21 dB Typ.
Midband beam width	16° Typ.
VSWR	1.2:1

Table 3.2: Specifications of the conical horn antenna, SGH-42-SC000 (millitech).

domain data of input power within "analysis bandwidth" is once collected. Then, the collected data is transformed into the frequency-domain space. A window function defined with "resolution bandwidth" is applied in this calculation. We take the frequency bin width and resolution bandwidth to be identical. The adjacent frequency bins are correlated because of sideband effect of the window function. As shown in Fig. 3.17, we see its effect in re-Fourier transformed spectrum (therefore returning to time-domained data). To avoid this effect, we set the resolution bandwidth and the bin width should be finer than analysis bin width, and we diminish the correlation in analysis stage. We choose the analysis bin width of 5kHz and the resolution band of 1 kHz. We sum up 5 bins prior to the analysis.

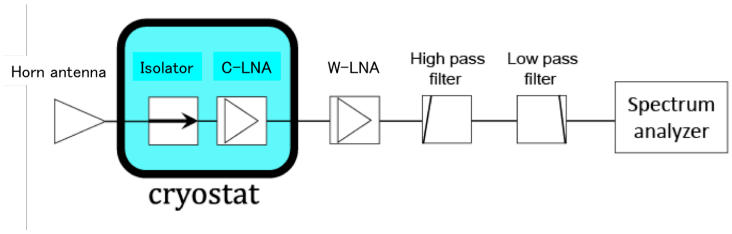

Figure 3.9: Block diagram of the receiver. Horn antenna receives radiation. Cold amplifier (C-LNA) provides gain of about 30 dB with low noise. Isolator rejects return power from C-LNA. Another amplifier at room temperature (W-LNA) has 40 dB amplification gain.

Parameter	Value
Frequency range	20.0-30.0 GHz
Isolation	18 dB MIN
Insertion loss	0.70 dB MAX
VSWR	1.40 MAX

Table 3.3: The specification for cryogenic isolator D3I2030 (DITOM MICROWAVE INC.).

3.6 Environmental monitors

We attach a thermocouple to the warm amplifier, and connected it to a logger, as shown in Fig. 3.19. We also measure temperature and humidity inside and outside of our apparatus. The background noise level is driven by emissions from atmosphere and leakage emission from the ground. Because there is a broad emission peak from water molecules around 20-30 GHz range (the peak center is 22 GHz), the background noise level depends on the weather. The temperatures inside receiver housing are recorded using thermocouples and logger as shown in Fig. 3.19. The ambient temperature and humidity are measured by a thermometer/hygrometer shown in Fig. 3.21. We record them every a few hours. This is the timing of the gain calibration explained in Sec. 5.1.

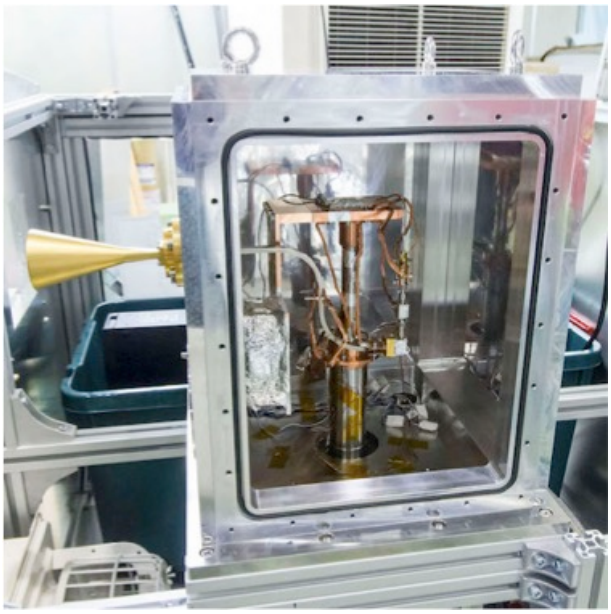

Figure 3.10: A cryostat of the cold receiver. The signals in millimeter wave range are collected by the horn antenna which is set on the left wall in this picture. Then, the signals go into an isolator via waveguide. A cryogenic amplifier amplifies the intensity of the signal. The amplified signals go outside of the receiver by using a coaxial cable and a feed through. A mechanical refrigerator maintains the isolator and the amplifier at the cold condition of $\simeq$ 10 K.

Parameter	Test condition	Value
Gain	15-26 GHz	28 dB
Noise	15-26 GHz	9.9 K
IRL	15-26 GHz	12 dB
ORL	15-26 GHz	17 dB
P_{1dB}	15-26 GHz	-7 dBm
OIP3	1-12 GHz	3 dBm

Table 3.4: The typical RF characteristics of Cryogenic Low Noise Amplifier LNF-LNC15_29A (LOW NOISE FACTORY).

Figure 3.11: The housing of the receiver. The horn antenna sees sky through a microwave-transparent window. This housing holds the cryostat (Fig. 3.10) and other facilities, such as spectrum analyzers, room temperature amplifiers, computers, an uninterruptible power supply (UPS).

Figure 3.12: KUMODeS (the receiver). The housing protects facilities inside from rains and winds.

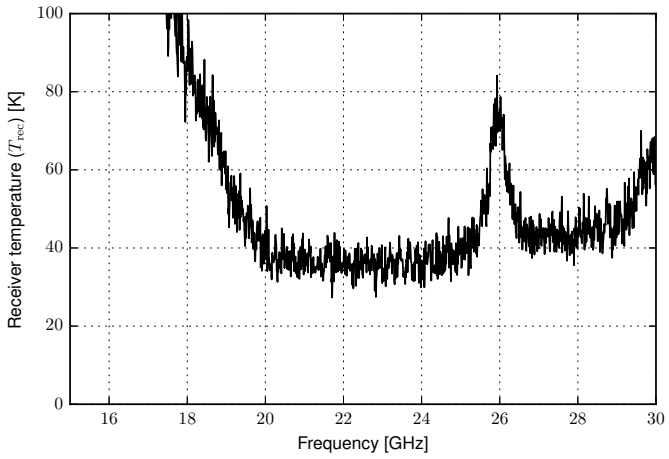

Figure 3.13: Receiver temperature (intrinsic noise level in a unit of effective blackbody temperature) as a function of frequency.

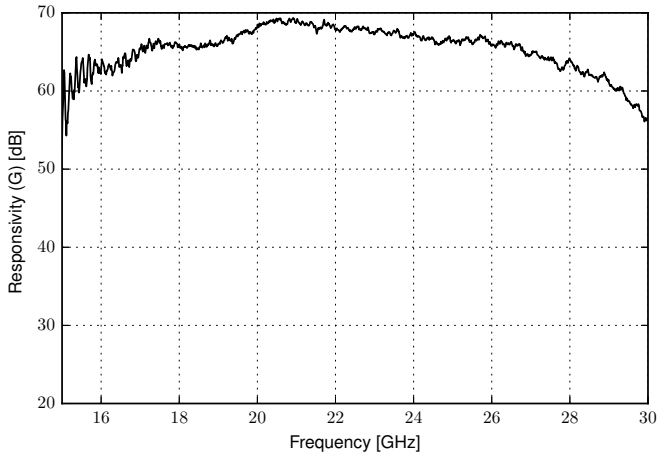

Figure 3.14: Typical responsivity (amplifier gain) of the receiver.

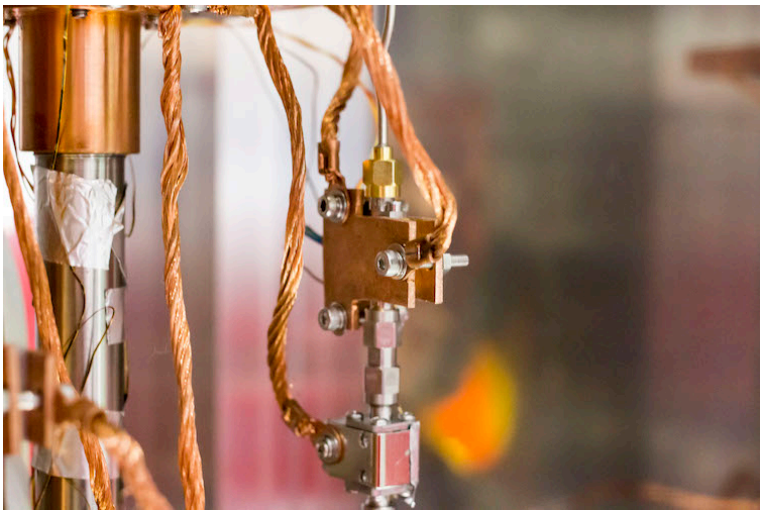

Figure 3.15: Cryogenic Low Noise Amplifier, LNF-LNC15_29A (LOW NOISE FACTORY). This is set in the cryostat. Photo Courtesy of KEK IPNS/Shota Takahashi.

Parameter	Value
Frequency range	18.0–26.5 GHz
Gain	38-44 dB
Gain Flatness	± 2.5 dB
Noise Figure	4.0 dB Typ.
P1dB	10 dBm min.
IP3	20 dBm Typ.
VSWR In	2.2:1
VSWR Out	2.2:1
+12 Vdc	300

Table 3.5: The specification of room temperature amplifier ALM-1826S210 (Aldetec).

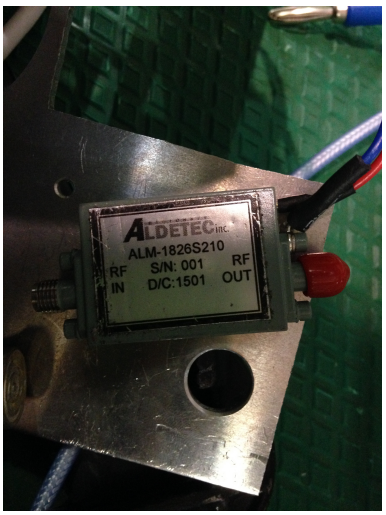

Figure 3.16: Room temperature amplifier, ALM-1826S210 (Aldetec).

Frequency range	10 Hz – 32 GHz
Resolution bandwidth	1 Hz – 8 MHz
Signal analysis bandwidth	10 Hz – 10 MHz
Displayed average noise level (DANL)	
20–26.5 GHz	−142 dBm Spec., −145 dBm Typ.
26.4–34 GHz	−140 dBm Spec., −144 dBm Typ.
Phase noise (1 GHz Carrier frequency)	−101 dBc/Hz nominal at 1 kHz offset
Carrier frequency accuracy	±[(time since last adjustment × aging rate) + temperature stability + calibration accuracy)]
aging rate	$\pm\ 1 \times 10^{-6}$ / year
temperature stability	$\pm\ 2 \times 10^{-6}$, 0 to 55 ℃
achievable initial accuracy	$\pm\ 1.4 \times 10^{-6}$

Table 3.6: Specification of spectrum analyzer N9010A (option 532)

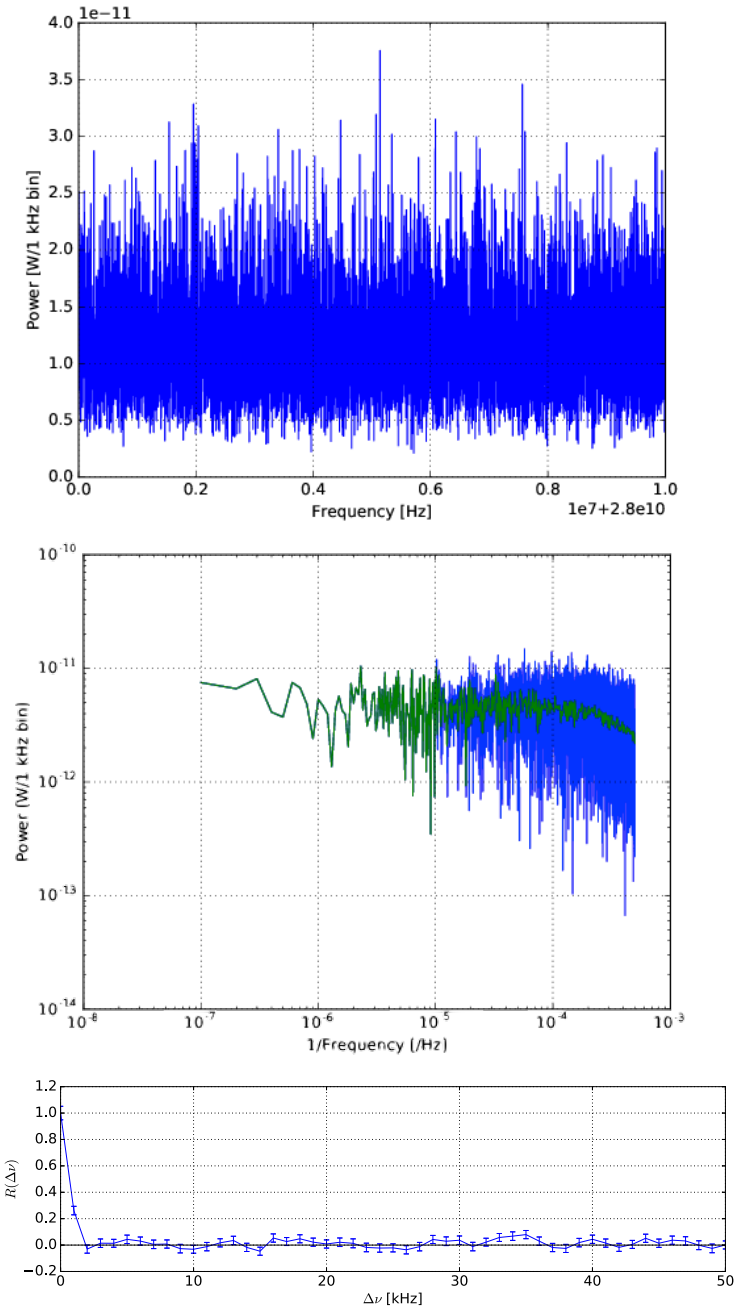

Figure 3.17: Raw data of the spectrometer (top panel). We set both resolution band width and the bin width at 1 kHz. Therefore, we have 10,001 samples in the range of 1 MHz. The adjacent bins may have correlation. We check correlation in Fourier space. If the correlation exists, it appears as a cut off at certain frequency. The Fourier transformed spectra are shown in the middle panel. Green curve is averaged spectrum to be smooth. The cut off which arise from correlation between adjacent bins can be seen above $O(10^{-4})$ /Hz. The bottom panel shows self correlation coefficients between bins, calculated using the first 1000 points of data.

Figure 3.18: Spectrum analyzer N9010A (Agilent Technologies).

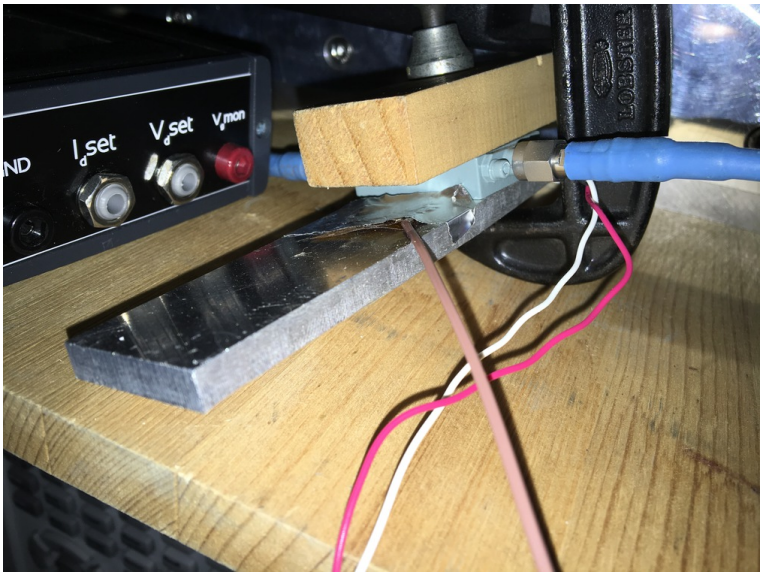

Figure 3.19: The room temperature amplifier is clamped to an aluminum plate as a heat radiator. A temperature sensor is attached here with an adhesive tape.

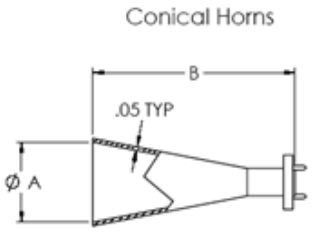

Figure 3.20: Schematics of the conical horn SGH-42-SC000 (millitech). A=59.690 mm and B=111.354 mm [38].

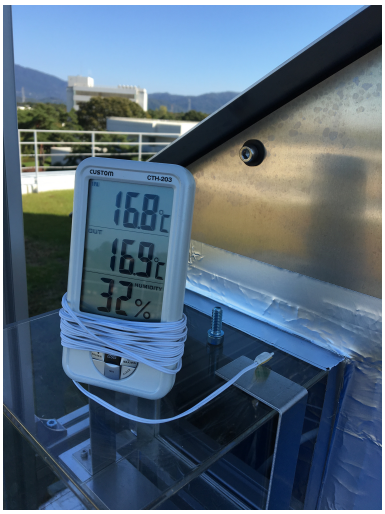

Figure 3.21: Thermometer/hygrometer CTH-203 (CUSTOM) to monitor ambient condition.

Chapter 4

Data sets

This chapter describes about our data sets. Configuration of spectrum analyzer setting, and basic data treatments prior to the analysis are also defined here. They are identical both in HPCDM search and calibration.

4.1 Weather conditions

We took HPCDM search data from 18:17 on 26th to 11:34 AM on 28th in Oct. 2016. As shown in Fig. 4.1, the data was taken under the sky to minimize the effect of background noise. The weather during the measurements is shown in Tab. 4.1. As noted in Sec. 3.6, the noise level is related to the weather condition, because of the broad emission peak of water molecules. We select data in analysis stage to maintain its quality.

Figure 4.1: The receiver system and mirror, for HPCDM search.

time \ date	10/26				10/27				10/28			
	Temp. ℃	Hum. %	Weather	T_{load} K	Temp. ℃	Hum. %	Weather	T_{load} K	Temp. ℃	Hum. %	Weather	T_{load} K
1:00	12.3	90	cloudy		18.1	86	rainy	235	8.6	93	sunny	141
2:00	12.7	85	cloudy		17.2	90	cloudy	209	8.0	94	sunny	140
3:00	13.0	86	cloudy		15.5	95	cloudy	193	7.6	92	sunny	140
4:00	13.1	89	cloudy		14.7	97	sunny	196	7.6	94	sunny	147
5:00	13.5	89	cloudy		14.3	97	sunny	202	8.5	94	cloudy	148
6:00	14.1	91	cloudy		13.1	97	sunny	207	9.4	91	cloudy	147
7:00	14.6	81	cloudy		14.7	98	sunny	214	11.1	82	cloudy	154
8:00	16.3	73	sunny		17.7	85	sunny		12.6	72	cloudy	148
9:00	18.0	67	sunny		19.7	62	sunny		11.5	81	cloudy	170
10:00	20.1	63	sunny		19.9	62	sunny		11.0	80	cloudy	174
11:00	21.7	63	sunny		20.5	52	sunny		11.3	79	cloudy	177
12:00	22.4	58	sunny		21.3	39	sunny		11.6	81	rainy	
13:00	23.4	57	sunny		22.2	27	sunny		10.9	91	rainy	
14:00	24.7	54	sunny		21.9	26	sunny		11.3	95	rainy	
15:00	25.4	59	sunny		22.0	24	sunny	142	12.6	97	rainy	
16:00	24.0	63	sunny		20.2	25	sunny	140	12.5	96	rainy	
17:00	20.3	84	sunny		17.5	62	sunny	143	11.3	97	rainy	
18:00	20.1	86	sunny		15.9	70	sunny	145	11.9	97	rainy	
19:00	19.2	89	sunny	155	14.9	72	sunny	142	12.0	97	rainy	
20:00	19.3	88	sunny	150	11.8	89	sunny	139	11.8	97	rainy	
21:00	19.2	84	cloudy	159	11.0	91	sunny	139	11.8	97	rainy	
22:00	18.1	91	cloudy	168	10.3	94	sunny	140	11.7	98	rainy	
23:00	17.8	92	cloudy	160	9.7	95	sunny	142	11.8	98	rainy	
24:00	17.9	90	cloudy	167	9.8	95	sunny	139	12.1	98	sunny	

Table 4.1: The weather conditions including temperature and humidity during the HPCDM search. They were monitored at Tateno(East longitude 140°07.4′, North latitude 36°3.4′, Tsukuba Prefecture), which is about 10 km distance from our experiment site [39]. The loading temperature ($T_{\mathrm{load}} = T_{\mathrm{sys}} - T_{\mathrm{rec}}$), the noise level as effective thermal load, is also quoted. T_{load} depends on the weather because of emission peak from water molecules.

4.2 Settings of spectrum analyzer

Settings of the spectrum analyzer is summarized in Table 4.2. They are identical for all data acquisition, HPCDM search, calibrations, and systematic error studies about frequency responses. The spectrum analyzer has two measurement modes, Swept mode and FFT mode. We choose FFT mode, as it provides effectively longer measurement time. We can choose an upper limit value of FFT analysis bandwidth from 9 different settings: 25 MHz, 10 MHz, 7.99 MHz, 411.9 kHz, 167.4 kHz, 28.81 kHz, 4.01 kHz. Based on the comparison of noise level, we choose the setting of 7.99 MHz. We also choose the bin width is 1kHz. It takes 4 seconds to measure the spectrum whose dynamic range is 10 MHz. The duty factor is approximately 1/300 in these parameters.

Frequency Range	27.998 – 28.012 GHz
Frequency span	10 MHz
Sweep mode	FFT mode
Resolution Band Width	1 kHz
Band width shape	Flat-top
number of points	10001
FFT analysis bandwidth	< 7.99 MHz

Table 4.2: Setting parameters of spectrum analyzer for our experiment.

4.3 Basic data treatments prior to analysis

4.3.1 Avoiding the structure from analysis bandwidth

There is a baseline gap at the center of the frequency range (the 5001th point of 10001 points). They corresponds to edges of the FFT analysis bandwidth. This gap arises at 5001th point even if we slightly change the starting frequency. The spectrum analyzer makes this gap. The spectrum analyzer internally divides their data every 5 MHz range, the boundary point is calculated as the average of each edge. This is the reason to make the gap. This gap has potential risk to make a fake signal peak.

To avoid this effect, we take data in two steps. First, we measure over three over-wrapping frequency ranges, with frequency shifts of $\Delta f = -2$ MHz, 0 MHz, +2 MHz as described above. Second, we divide the 10001 points into two regions and treat the two regions as separate measurements. After binning the spectrum as described in Sec. 4.3.2, we discard a bin

which contains the 5001 th point. These treatments result in 6 frequency regions as shown in Fig. 4.3. For HPCDM search, we repeat 9 times of the measurements for these 6 regions. We call "run" for each measurement set of 6 regions, and we call "sub-run" for each 6 region measurement. We have $9 \times 6 = 54$ sub-runs for each run. We perform analysis for each sub-run, separately. Then, we combine the all sub-run results, and we obtain the results for each frequency bin.

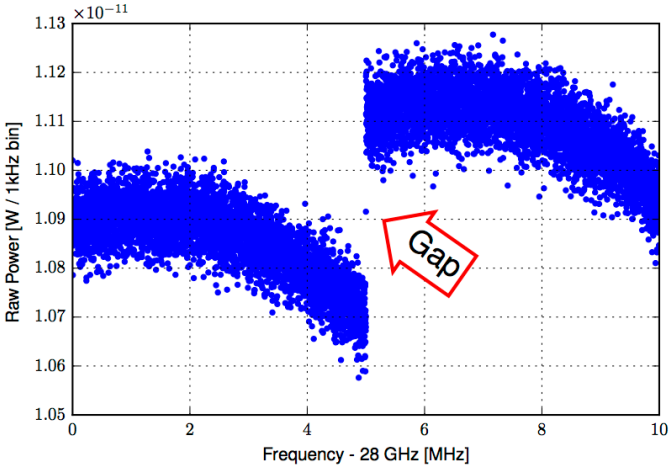

Figure 4.2: Average of 10000 measurements of 10 MHz span sweeps. There is a gap at the 5001th point in 10001 points. We do not use a bin which contains this gap point in our analysis.

4.3.2 Rebin

The raw data has correlation between adjacent bins. We add 5 points to diminish this effects as mentioned in 3.5.

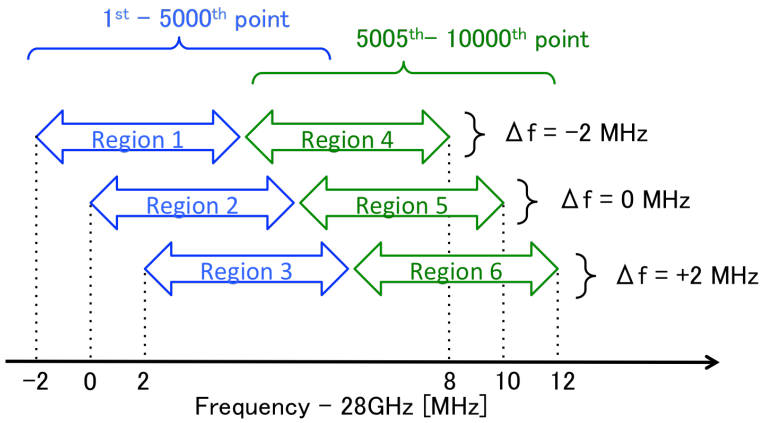

Figure 4.3: Definition of 6 frequency regions. The regions 1 and 4 are simultaneously measured, the regions 2 and 5 are measured in next, then the regions 3 and 6 are measured. We repeat measurements for these 6 regions.

Chapter 5

Calibration

In this chapter, we describe details about calibrations: the responsivity of the receiver, the effective area of the antenna, and precision of the frequency. Precisions of the responsivity and the effective area of the antenna determine the uncertainty of measured power (i.e. HPCDM - photon coupling constant χ). The frequency response determines HPCDM mass ($m_{\gamma'}$), and its instability potentially causes inefficiency of the measured power.

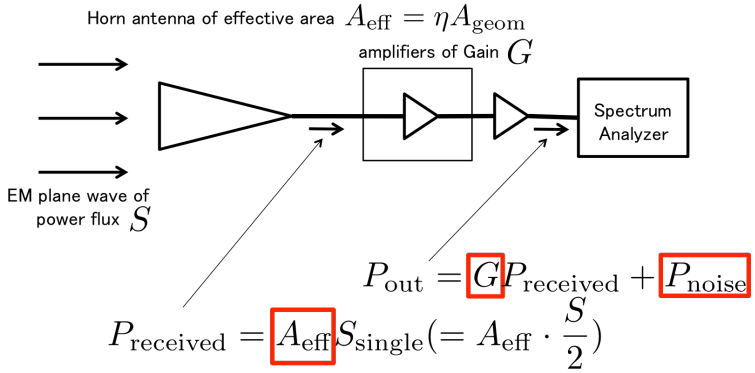

Figure 5.1: The schematics of power at each part of system. Assuming an unpolarized plane wave of power flux density S, the horn antenna collects one of the two polarization components (thus $S_{\mathrm{single}} = S/2$), within its effective area A_{eff}. The collected power (P_{received}) is amplified by a factor of G. We also have an extra power derived from the intrinsic noise of the system (P_{noise}).

5.1 Responsivity and receiver temperature

There are two amplifiers in the receiver system. Suppose the antenna is covered by blackbody of temperature T, the output power from the system is represented by

$$P_{\rm out} = GP_{\rm received} + P_{\rm noise} = G \times k_B(T + T_{\rm rec})\Delta\nu, \tag{5.1}$$

where G is the responsivity which is a dimensionless amplification factor, $P_{\rm received}$ is the power collected by antenna, $P_{\rm noise}$ is power of noise from system itself, k_B is Boltzmann constant, $\Delta\nu$ is band width of measurement, and $T_{\rm rec}$ is the receiver temperature. The responsivity is frequently represented in the unit of dB:

$$G[\mathrm{dB}] = 10\log_{10} G. \tag{5.2}$$

The comparison of response for two different temperature determines them as shown in Fig. 5.2. We take an average of 5 measurements for each calibration. Typical results are $G \simeq 63$dB and $T_{\rm rec} \simeq 45$K at 28 GHz as shown in Fig. 3.13 and 3.14.

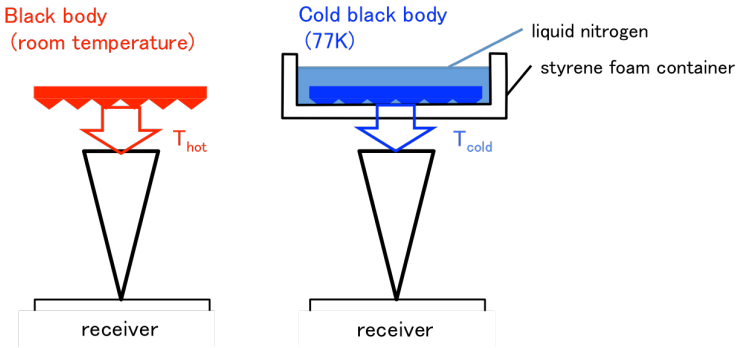

Figure 5.2: The schematics of gain calibration measurement.

We calibrate the responsivity every a few hours during the HPCDM search. We also calibrate the responsivity before and after the antenna effective area measurements. The measured results for each frequency region are summarized in Fig. 5.3, Table 5.1 and 5.2. A drift of the responsivity is mainly caused by changing of the ambient temperature as shown in Fig. 5.4 while there is hysteresis in time response. We adopt linearly interpolated numbers for each run. We assign a systematic error as an uncertainty of this model. It is conservatively assigned half numbers of difference among two calibrations. The level of drift is also used for the data selection to maintain the data quality (see 6.1).

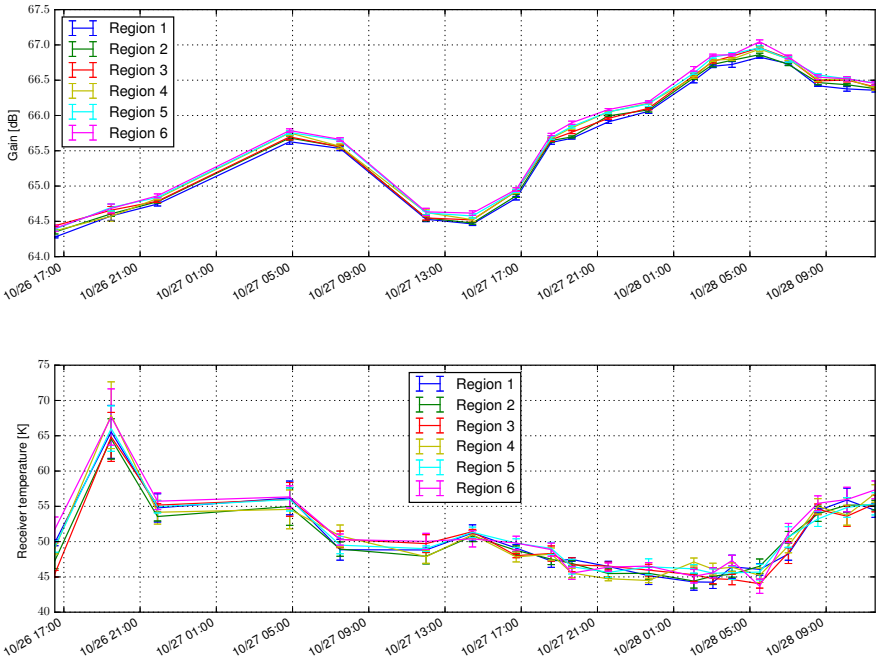

Figure 5.3: The gain calibration results during HPCDM measurement. The top is for gain and the bottom is for receiver temperature. Linearly interpolated gain is used for measurements between any two calibration. If two calibrations discrepancy cannot be ignored, the measurements between the two are rejected as explained in Sec. 6.1.

	G [dB]					
Date \ Region #	1	2	3	4	5	6
2016-10-26 16:31:28	64.276(11)	64.348(28)	64.437(8)	64.365(9)	64.388(25)	64.401(42)
2016-10-26 19:28:57	64.577(63)	64.607(38)	64.658(52)	64.572(69)	64.697(49)	64.683(62)
2016-10-26 21:54:51	64.745(28)	64.778(19)	64.785(19)	64.825(18)	64.838(6)	64.862(28)
2016-10-27 04:50:51	65.628(35)	65.681(29)	65.697(41)	65.753(34)	65.759(24)	65.787(24)
2016-10-27 07:29:45	65.533(32)	65.557(21)	65.556(26)	65.563(34)	65.647(19)	65.661(24)
2016-10-27 12:00:22	64.530(34)	64.548(42)	64.547(29)	64.626(48)	64.620(29)	64.634(51)
2016-10-27 14:26:36	64.464(23)	64.476(17)	64.521(24)	64.523(23)	64.576(31)	64.617(32)
2016-10-27 16:44:08	64.828(25)	64.862(24)	64.927(11)	64.927(28)	64.931(22)	64.952(25)
2016-10-27 18:34:39	65.618(26)	65.645(22)	65.657(25)	65.676(17)	65.688(23)	65.731(16)
2016-10-27 19:39:13	65.677(11)	65.696(14)	65.763(21)	65.827(22)	65.844(20)	65.897(23)
2016-10-27 21:34:22	65.910(22)	65.994(14)	65.959(13)	66.049(11)	66.052(19)	66.084(14)
2016-10-27 23:41:04	66.059(29)	66.080(31)	66.102(21)	66.174(12)	66.164(35)	66.195(14)
2016-10-28 02:03:32	66.494(31)	66.536(26)	66.568(31)	66.542(14)	66.601(16)	66.661(33)
2016-10-28 03:03:29	66.697(19)	66.724(35)	66.765(22)	66.784(19)	66.827(14)	66.856(14)
2016-10-28 04:03:42	66.723(40)	66.782(10)	66.840(19)	66.799(18)	66.872(19)	66.860(15)
2016-10-28 05:30:38	66.827(16)	66.862(20)	66.960(14)	66.941(31)	66.960(28)	67.045(26)
2016-10-28 07:01:18	66.735(21)	66.723(17)	66.809(33)	66.803(21)	66.794(37)	66.830(26)
2016-10-28 08:33:58	66.421(9)	66.466(31)	66.490(18)	66.508(27)	66.575(18)	66.543(33)
2016-10-28 10:05:34	66.377(32)	66.436(14)	66.503(27)	66.517(26)	66.519(23)	66.521(30)
2016-10-28 11:34:20	66.357(25)	66.381(10)	66.404(30)	66.387(30)	66.461(34)	66.453(26)

Table 5.1: Responsivity (amplifier gain) of the receiver. They were measured every 1–2 hour during the HPCDM search.

	Receiver temperature [K]					
Date \ Region #	1	2	3	4	5	6
2016-10-26 16:31:28	49.85(44)	47.29(114)	45.43(47)	49.01(78)	49.28(79)	51.74(175)
2016-10-26 19:28:57	65.55(375)	64.55(286)	64.84(347)	67.91(473)	66.01(322)	67.65(399)
2016-10-26 21:54:51	54.78(200)	53.56(63)	55.17(21)	54.17(168)	54.95(89)	55.73(119)
2016-10-27 04:50:51	56.19(239)	54.98(267)	55.98(239)	54.57(275)	55.97(163)	56.34(157)
2016-10-27 07:29:45	48.85(148)	48.94(102)	50.32(118)	50.81(155)	49.50(122)	50.29(79)
2016-10-27 12:00:22	48.82(25)	47.92(108)	49.71(127)	47.86(93)	48.99(40)	50.03(114)
2016-10-27 14:26:36	51.23(115)	50.79(80)	51.41(32)	51.00(58)	51.32(74)	50.39(115)
2016-10-27 16:44:08	49.09(51)	48.76(64)	48.02(30)	47.83(70)	49.78(62)	49.80(97)
2016-10-27 18:34:39	47.26(91)	47.51(77)	48.31(108)	48.24(87)	49.04(86)	48.86(93)
2016-10-27 19:39:13	47.47(26)	46.92(38)	46.71(98)	45.54(68)	46.45(104)	45.54(89)
2016-10-27 21:34:22	46.48(73)	45.48(66)	46.53(56)	44.74(29)	45.65(72)	46.39(58)
2016-10-27 23:41:04	45.18(126)	45.51(90)	45.96(84)	44.49(32)	46.43(113)	46.53(50)
2016-10-28 02:03:32	44.29(117)	44.41(100)	45.31(95)	47.11(56)	46.14(60)	45.09(96)
2016-10-28 03:03:29	44.25(89)	45.12(120)	44.76(73)	46.10(84)	45.52(62)	45.59(71)
2016-10-28 04:03:42	46.43(164)	45.38(41)	44.63(74)	46.37(62)	45.58(94)	47.33(73)
2016-10-28 05:30:38	46.07(83)	46.51(103)	44.04(63)	45.22(100)	45.68(111)	43.68(101)
2016-10-28 07:01:18	48.24(88)	50.61(83)	48.46(156)	49.41(99)	50.66(145)	51.21(137)
2016-10-28 08:33:58	54.40(32)	53.95(107)	54.57(75)	54.99(109)	53.20(105)	55.43(105)
2016-10-28 10:05:34	55.90(168)	55.17(105)	53.60(142)	53.75(141)	54.84(140)	55.96(174)
2016-10-28 11:34:20	54.42(98)	55.18(68)	55.39(117)	56.82(124)	55.36(158)	57.34(126)

Table 5.2: The receiver temperatures calibrated during HPCDM measurement.

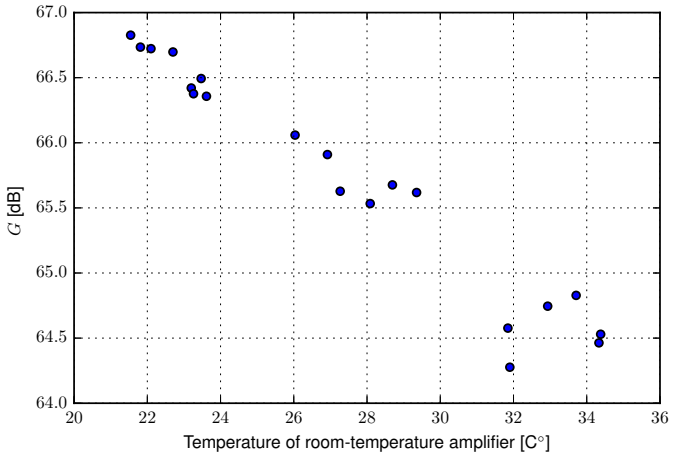

Figure 5.4: The relation between gain of receiver and temperature of room-temperature amplifier. The shown is result of frequency region 1, and results of other regions are similar.

5.2 Antenna effective area and beam profile

We measure the horn's effective area. We also measure the angular dependence of the effective area to estimate the systematic error caused by an angular uncertainty (alignment and hidden photon angular dispersion).

5.2.1 Radiation from blackbody and Sky temperature

Brightness temperature and sky temperature

Brightness is a quantity defined as power divided by solid angle, area, and frequency. The brightness of blackbody of temperature T, in the low frequency region $h\nu/k_BT \ll 1$, is proportional to T and described by Reighley-Jeans law,

$$I_\nu = \frac{dP}{d\nu dA d\Omega} = \frac{2\nu^2 k_B T}{c^2}, \tag{5.3}$$

where ν is the frequency, k_B is Boltzmann constant, T is the temperature of blackbody, A is the area of the destination, Ω is solid angle the source blackbody extends from the destination. The "brightness temperature" T_b is a variable used in astronomical observation, which is defined as

$$T_b = \frac{I_\nu c^2}{2k_B\nu^2}, \tag{5.4}$$

even in the case the source is not blackbody. In case the entire view of the antenna is covered with a blackbody of T, T_b coincides with T in the Reighley-Jeans' region. From Eq. 5.1, we can calculate this brightness temperature using G and $T_{\rm rec}$ obtained from gain calibration,

$$T_b = \frac{P_{\rm out}}{Gk_BB} - T_{\rm rec}, \tag{5.5}$$

where $P_{\rm out}$ is output power of the receiver, k_B is Boltzmann constant, B is the band width of measurement, $T_{\rm rec}$ is the receiver temperature.

The "sky temperature" $T_{\rm sky}$ is the brightness temperature of the sky. $T_{\rm sky}$ is calculated using this equation, from measurement data taken without blackbody, and takes value of ≈ 50 K with low humidity at up sky. The measured power is proportional to brightness temperature because our condition satisfies: $h\nu/k_BT \ll 1$ holds for ν =28GHz and $T = 300$ or ≈ 50 K.

Power from blackbody

Assume an antenna is oriented vertically upwards, under the sky of sky temperature $T_{\rm sky}$. When a blackbody of temperature $T_{\rm BB} = 0$ K is placed in front of the antenna, it blocks a part of atmospheric radiation. From the definition of sky temperature, the power that arrives an antenna changes by,

$$-\frac{2\nu^2 k_B T_{\rm sky}}{c^2} A_{\rm geom} \cdot \Omega \cdot \Delta\nu, \tag{5.6}$$

where $A_{\rm geom}$ is the geometrical aperture of antenna, Ω is the solid angle the blackbody source extends, $\Delta\nu$ is the bandwidth. Therefore, if $T_{\rm BB}$ is within Reighley-Jeans' region, the difference of powers that arrives antenna between two conditions (with and without blackbody) is described as follows,

$$P_{\rm diff,0} = \frac{2\nu^2 k_B (T_{\rm BB} - T_{\rm sky})}{c^2} A_{\rm geom} \cdot \Omega \cdot \Delta\nu. \tag{5.7}$$

The ratio between the geometrical area $A_{\rm geom}$ of horn aperture and effective area $A_{\rm eff}$ is "antenna efficiency" η, which is obtained by

$$\eta = \frac{2P_{\rm diff,obs}}{P_{\rm diff,0}}, \tag{5.8}$$

where $P_{\rm diff,obs}$ is the difference of power received by antenna, between the two conditions. The factor of two in Eq. 5.8 comes from the fact the antenna receives only one component of polarization.

5.2.2 Set up

We place a small blackbody source at the same location of the mirror. It satisfies far-field condition, and the distance from the horn aperture is 1030±9 mm. We use ECCOSORB AN-72 as blackbody source. We cut it to be round shape of 60 mm diameter. We carry out two types of measurements: one is antenna beam pattern measurement, and the other is consistency check about the area of blackbody source. In beam pattern measurement, we measure power from blackbody at various locations, by measuring power received by antenna with and without blackbody and take the difference between them. As sky temperature fluctuates with atmospheric condition, we conduct measurement alternatively and use the difference between the nearest measurements.

The schematics of measurement setup is shown in Fig. 5.5. We measure output power from horn antenna, with and without blackbody source, and take the difference between them at each blackbody positions. We built the

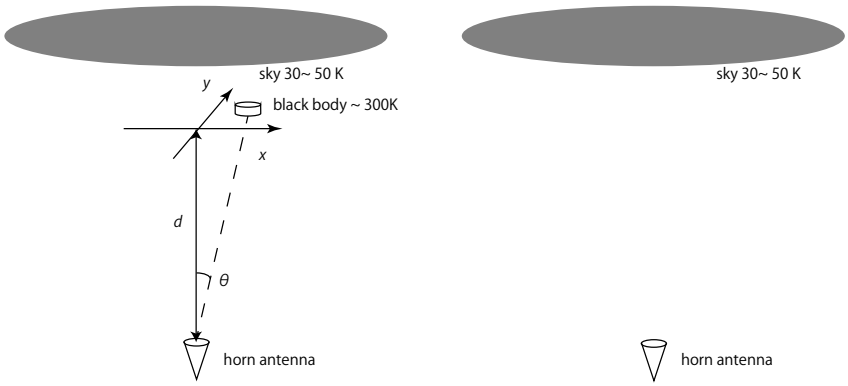

Figure 5.5: Setup schematic of antenna calibration measurement. We measure difference of output power from horn antenna between two condition: with and without blackbody source. We repeat the measurement at various locations of the blackbody source.

measurement setup as shown in Fig. 5.6. On top of the frame, a styrofoam plate (t = 21 mm) is placed above horn. A 50 mm grid is imprinted on the plate for the purpose of alignment of the blackbody (Fig. 5.7). The attenuation from the styrofoam plate is estimated and we found it negligible [40]. We also use styrofoam piece (100 mm × 100 mm) as the blackbody source folder because we use various size of them for the variation of our measurements 5.8. The blackbody is attached on this folder by using double-sided adhesive tape. We varied the size of the blackbody source. We confirmed the measured power is properly proportional to the area of blackbody (Fig. 5.10).

We measured the antenna effective area on 24th and 26th in Oct. 2016. The temperature of blackbody target are measured several times during measurement by using a thermometer CTH-203 (CUSTOM). Measured blackbody temperatures are summarized in Table 5.3. Average temperatures during the calibration in each day are 299 K in Oct. 24th and 302 K in Oct.26th, respectively. For the sky temperature, measured results are summarized in Fig. 5.15. Their averages are 31.6 ± 1.7 K in Oct. 24th and 42.2 ± 1.6 K in Oct. 26th, respectively.

We calibrate the responsivity of the receiver before and after each measurement. We adopt interpolated responsivity model as described in Sec. 5.1. The position of source is aligned based on grid lines marked on the styrofoam board. As shown in Fig. 5.11, we measure at 25 locations in total; 5×5 steps along x and y axes with a spacing of 50 mm. Figure 5.12 shows example of these measurements.

Figure 5.6: Photograph of antenna measurement setup.

5.2.3 Analysis

Angular response of the antenna (hereafter "beam") is modeled by two-dimensional Gaussian function. We fit measured data by using a formula,

$$f(x, y; x_0, y_0, \sigma, P_{\mathrm{diff,obs}}) = P_{\mathrm{diff,obs}} e^{-\frac{(x-x_0)^2+(y-y_0)^2}{2\sigma^2}} \cos\theta, \tag{5.9}$$

where $\theta = \arctan\left(\frac{\sqrt{(x-x_0)^2+(y-y_0)^2}}{d}\right)$ is the angle between the line of sight to the blackbody and the axis of horn antenna. We multiply $\cos\theta$ as a correction factor for the blackbody area. The error for d is contained in

date	T_{BB} [K]
10/24 10:52	297.9
10/24 11:12	300.7
10/24 11:20	299.9
10/24 11:27	299.1
10/26 15:42	302.9
10/26 15:52	302.0
10/26 16:00	301.7

Table 5.3: The temperatures of blackbody source (T_{BB}) during the antenna calibration measurements. The precision of the record time of is about 3 minutes.

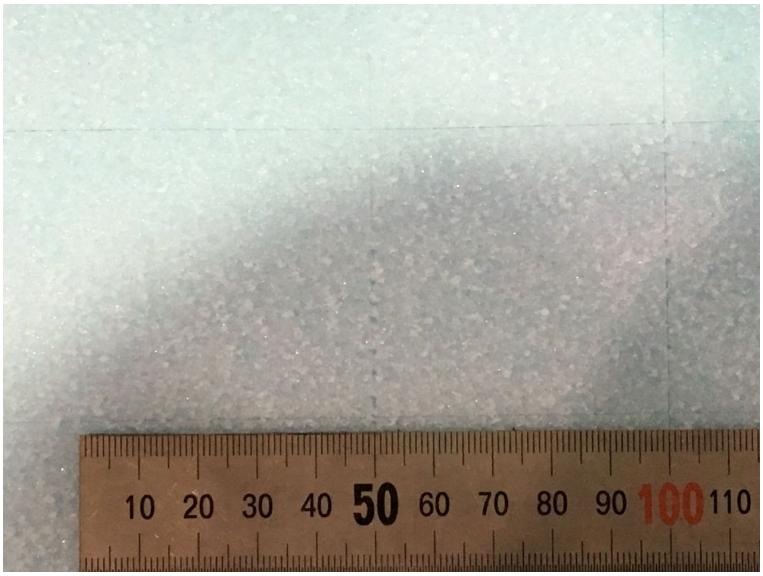

Figure 5.7: Grid lines are marked on styrofoam board for the beam calibration.

$\cos\theta$, while its effect is a second order, $(\Delta d/d)^2$. The first order effect, $(\Delta d/d)^1$, is included in the systematic error for $P_{\mathrm{diff},0}$ (Eq. 5.7, through Ω). There are 4 parameters in this fit; $P_{\mathrm{diff,obs}}$ is the maximum output power difference, x_0 and y_0 are coordinate of the center of beam relative to the center of styrofoam board, and σ is a beam width. We have 300 sub-runs in total for this calibration in each day: 6 (frequency regions) $\times$ 25 (blackbody locations) $\times$ 2 (with or without blackbody). We use averaged number for each frequency region. We extract the parameters for each of them. Fit results are summarized in Table 5.4 and 5.5. Examples of fit results are shown in Fig. 5.13.

We have 6 fit results in each day. We combine these 12 results to obtain the value η. Fit errors for each 12 measurement is independent because they are statistical error. On the other hand, parts of systematic errors are not independent among the measurements.

- Common systematic errors for each day

  The systematic error from temperatures and amplifier gain are common in a day.

  1. Amplifier gain (G)

     We calibrated the amplifier gain before and after antenna measurement, and take the half of difference as ΔG, in the same manner

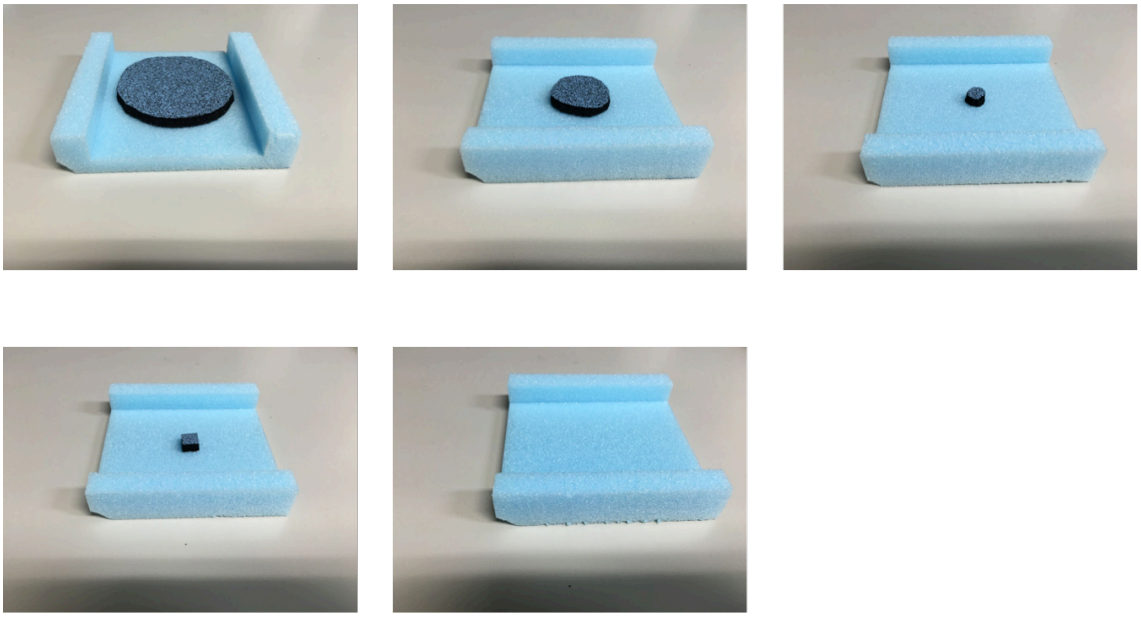

Figure 5.8: We use black body piece in various dimensions for the purpose of linearity check of the measurements. Their dimension are (from top left to top right, and bottom left to bottom right), circle of ϕ 60 mm, circle of ϕ 30 mm, circle of ϕ 10 mm, 10mm x 10mm square. They are attached on a styrofoam socket piece in photos, and they are aligned along the grids as shown in Fig. 5.9.

as in HPCDM measurement. The calibration results are shown in Fig. 5.14. We used $\Delta G = 0.17$ dB (3.9 %) for 24th Oct. and 0.10 dB (2.4 %) for 26 th Oct.

2. Sky temperature ($T_{\rm sky}$)

   We have 6 $\times$ 25 measurements for $T_{\rm sky}$ in total, as shown in Fig. 5.15. We conservatively take half number of their maximum difference of 25 for each frequency region. We used the maximum of 6 values of $\Delta T_{\rm sky}/T_{\rm sky}$, 5.4% (1.7 K / 31.6 K) for 24th Oct. and 3.9% (1.6 K / 42.2 K) for 26th Oct.

3. Black body temperature ($T_{\rm BB}$)

   We conservatively assign the maximum difference during each calibration. Based on Table 5.3, we assign systematic errors $\Delta T_{\rm BB}$. $\Delta T_{\rm BB}/T_{\rm BB}$ are 0.9% for 24th Oct. and 0.4% for 26th Oct., respectively.

- Common systematic error among 12 measurements

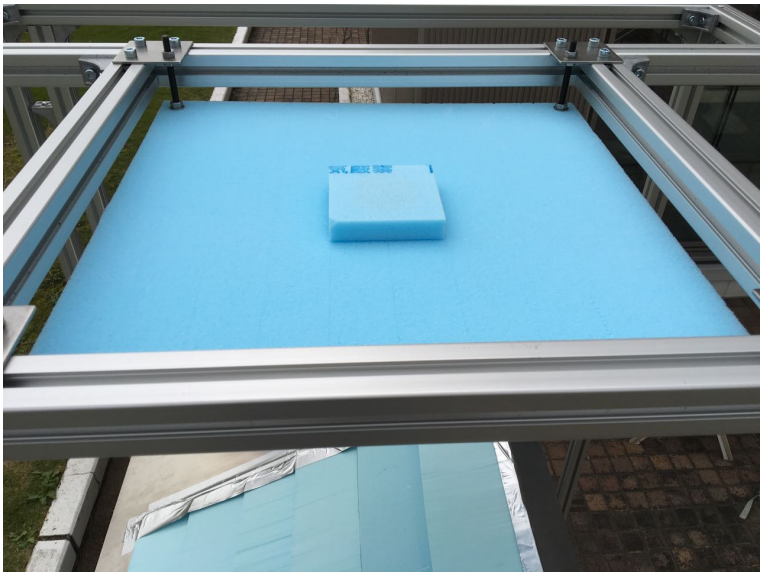

Figure 5.9: The socket containing black body piece (Fig. 5.8) is placed on the styrofoam board. Here, we aligned it at the center, $(x, y) = (0, 0)$.

Uncertainty of solid angle (Ω) is common for all measurements. We assign the error of the distance d ($= 1030 \pm 9$ mm) and the diameter of the black body source $\phi_{\rm BB}$ ($= 60 \pm 1$ mm), because $\Omega = A_{\rm BB}/d^2 = \pi(\phi_{\rm BB}/2)^2/d^2$, where $A_{\rm BB}$ is the area of the black body source. We obtain

$$\Omega = (2.67 \pm 0.10) \times 10^{-3}.$$

5.2.4 Results

The results of 12 measurements are summarized in Fig. 5.16. We calculate weighted average for each day, i.e. 6 measurements for each. Then, we take average of two numbers for each day with weights of the systematic errors for each day. Finally, we obtain $\eta = 0.560 \pm 0.032$. The effective area for the horn antenna is,

$$A_{\rm eff} = \eta A_{\rm geom} \tag{5.10}$$
$$= (1.48 \pm 0.08) \times 10^{-3} [{\rm m}^2]. \tag{5.11}$$

We also obtain the beam width ($\theta_{1/2}$) using the fitting results (Tab. 5.4, 5.5). Combining the fitting results, the radius of beam at the styrofoam board is $\sigma = 95.9 \pm 1.7$mm. Combining this and the distance $d = 1030 \pm 9$mm

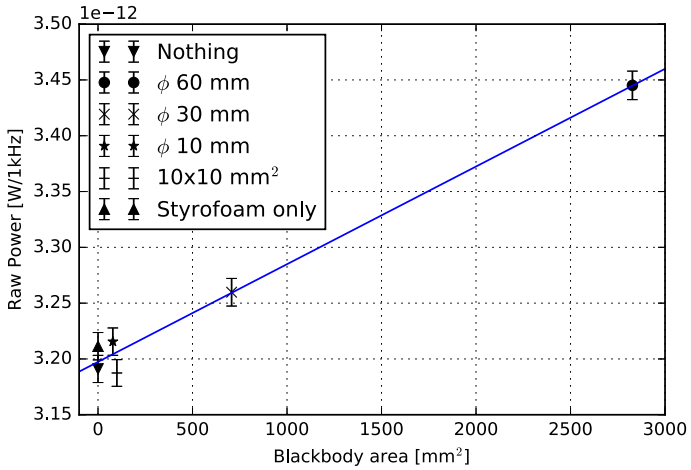

Figure 5.10: Power from blackbodies of various sizes.

between the horn antenna and the blackbody source, we obtain the beam width

$$\theta_{1/2} = 2 \arctan\left(\sqrt{2\log 2} \cdot \frac{\sigma}{d}\right) = 12.52 \pm 0.05 \quad \text{deg.} \tag{5.12}$$

The beam width is inversely proportional to frequency. In the specification of this horn antenna (Tab. 3.2), the beam width is 16° at the center of its band, 23 GHz. Therefore the beamwidth at 28 GHz is 16°/(28GHz/23GHz) = 13°, which is roughly consistent with the obtained result.

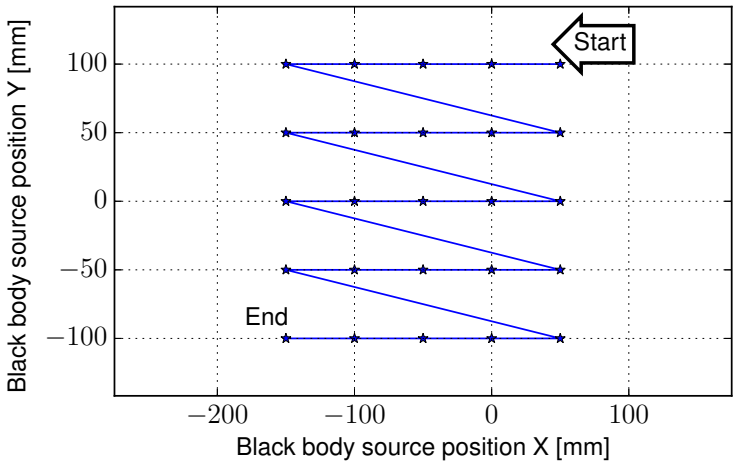

Figure 5.11: Locations of blackbody source for measurement on 24th October. For each of this positions, measurement was carried out with and without blackbody. The coordinate is relative to the center of styrofoam board. The resulting measurement data are shown in Fig. 5.12.

Region #	x_0 [mm]	y_0 [mm]	σ [mm]	$P_{\mathrm{diff,obs}}$ [W/kHz]
1	-67.9 ± 3.8	-10.9 ± 3.7	101.8 ± 4.3	$1.253(43)\times10^{-19}$
2	-65.7 ± 3.6	-2.6 ± 3.5	95.7 ± 3.8	$1.235(45)\times10^{-19}$
3	-60.9 ± 3.6	-12.9 ± 3.6	99.0 ± 4.0	$1.276(44)\times10^{-19}$
4	-55.9 ± 3.5	-10.2 ± 3.5	97.8 ± 3.9	$1.284(45)\times10^{-19}$
5	-69.8 ± 3.3	-11.1 ± 3.2	91.6 ± 3.3	$1.366(47)\times10^{-19}$
6	-55.1 ± 3.4	-12.4 ± 3.4	96.0 ± 3.6	$1.329(46)\times10^{-19}$

Table 5.4: The fitting results for each frequency regions, for 24th Oct., 2016.

Region #	x_0 [mm]	y_0 [mm]	σ [mm]	$P_{\mathrm{diff,obs}}$ [W/kHz]
1	-64.6 ± 4.9	1.1 ± 4.7	103.2 ± 5.5	$1.129(49)\times10^{-19}$
2	-77.3 ± 4.7	-7.1 ± 4.4	96.2 ± 4.8	$1.171(51)\times10^{-19}$
3	-80.7 ± 5.2	0.6 ± 4.7	104.1 ± 5.6	$1.176(50)\times10^{-19}$
4	-72.3 ± 4.2	1.3 ± 3.9	95.4 ± 4.3	$1.292(52)\times10^{-19}$
5	-77.1 ± 5.1	-8.3 ± 4.7	106.1 ± 5.7	$1.220(50)\times10^{-19}$
6	-71.3 ± 3.5	-3.5 ± 3.4	84.8 ± 3.3	$1.405(57)\times10^{-19}$

Table 5.5: The fitting results for each frequency regions, for 26th Oct., 2016.

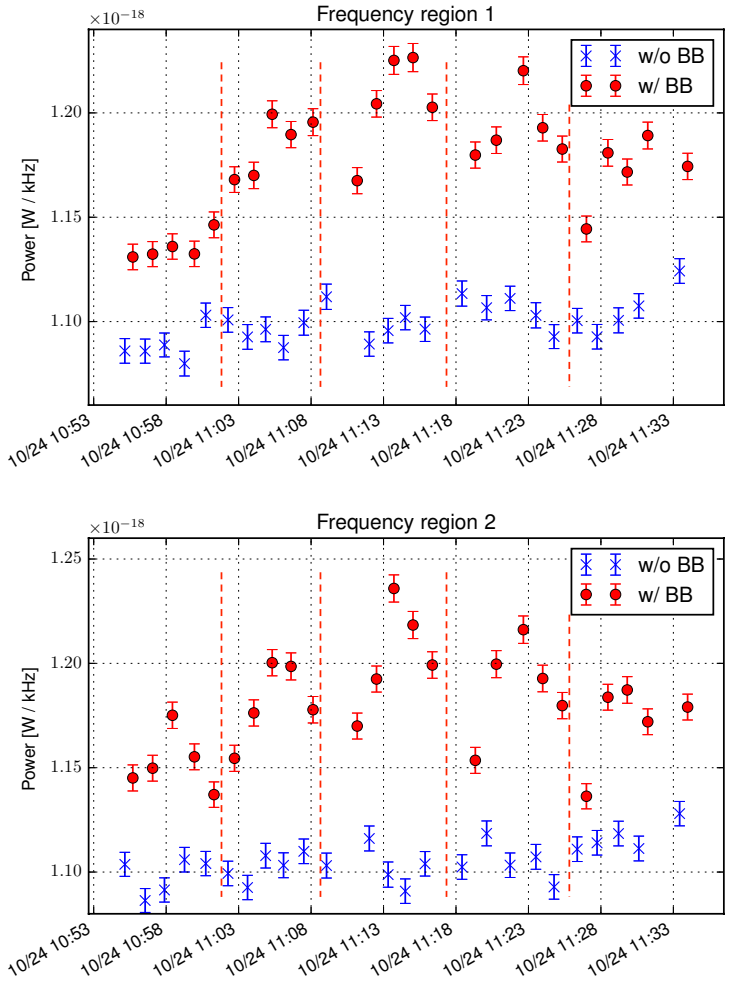

Figure 5.12: Examples of measured powers for each location. They are results for frequency region 1 (top panel) and 2 (bottom panel). Order of points follows Fig. 5.11.

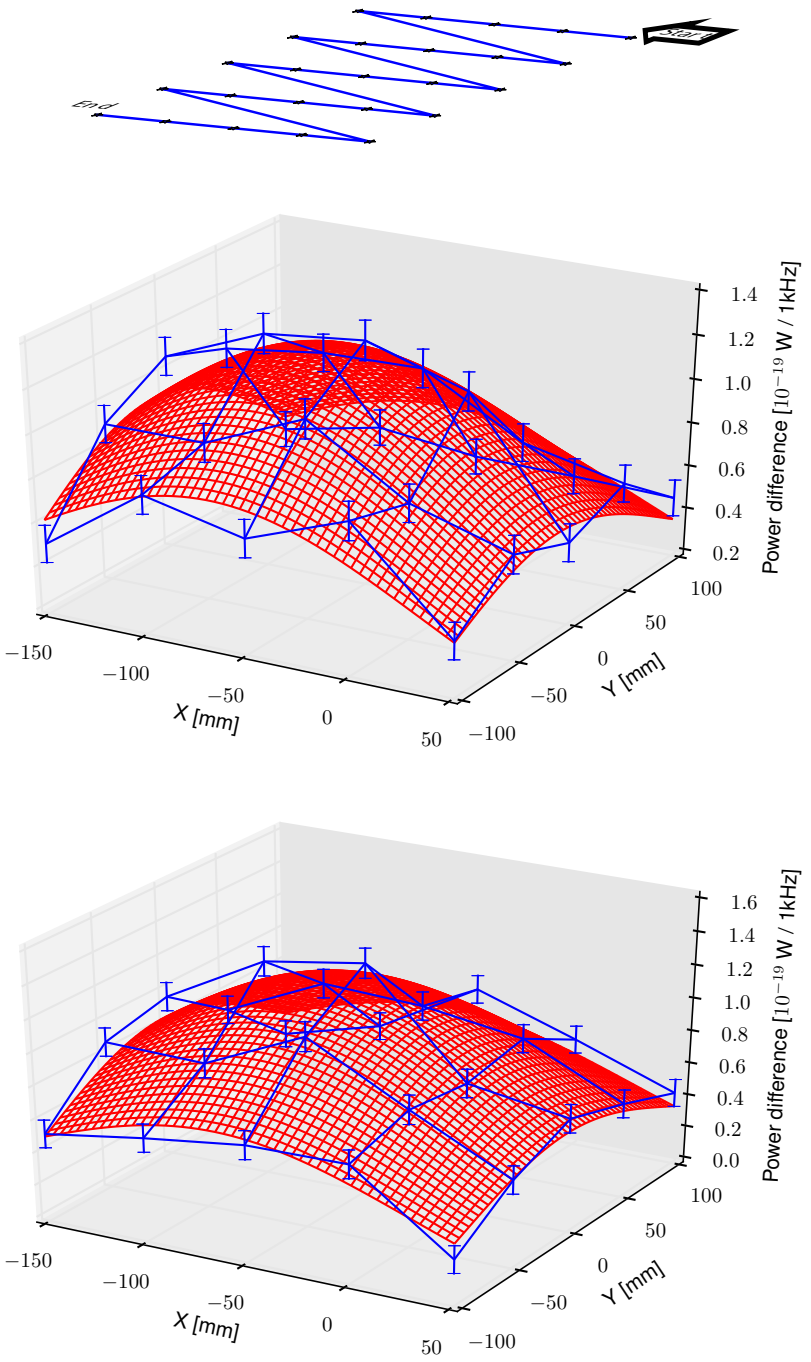

Figure 5.13: Fit results for the frequency region 1 (middle panel) and 2 (bottom panel). The top panel shows the order of measurements in the same manner as Fig. 5.11. They are measurement on 24th October. The blue points are measured data, and red surface is the fit result.

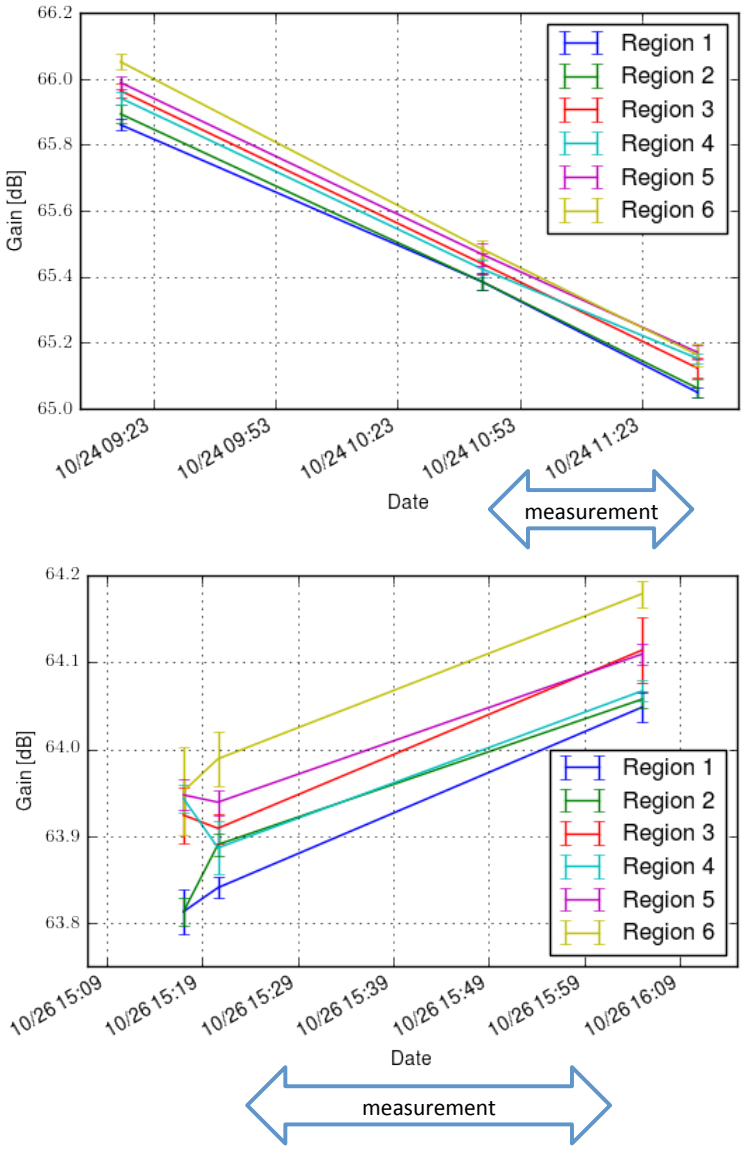

Figure 5.14: The amplifier gain calibration results for antenna measureemnt. The antenna measurement was conducted in the time range designated as arrows. We use half number of difference for systematics. We use the maximum value of 6 regions, $\Delta G = 0.17$ dB for 24th Oct. and $\Delta G = 0.10$ dB for 26 th Oct.

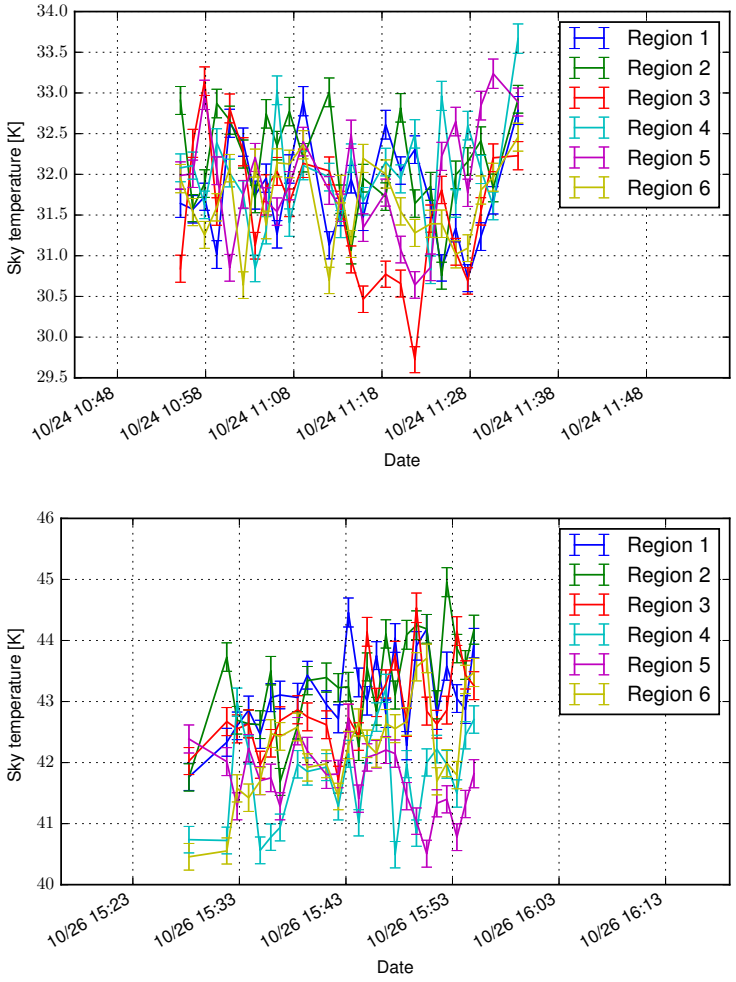

Figure 5.15: The sky temperature calculated from measurement data without blackbody source, for each frequency regions. The top panel shows the results for measurement on 24th Oct. 2016, and the bottom panel shows that for measurement on 26th Oct. 2016.

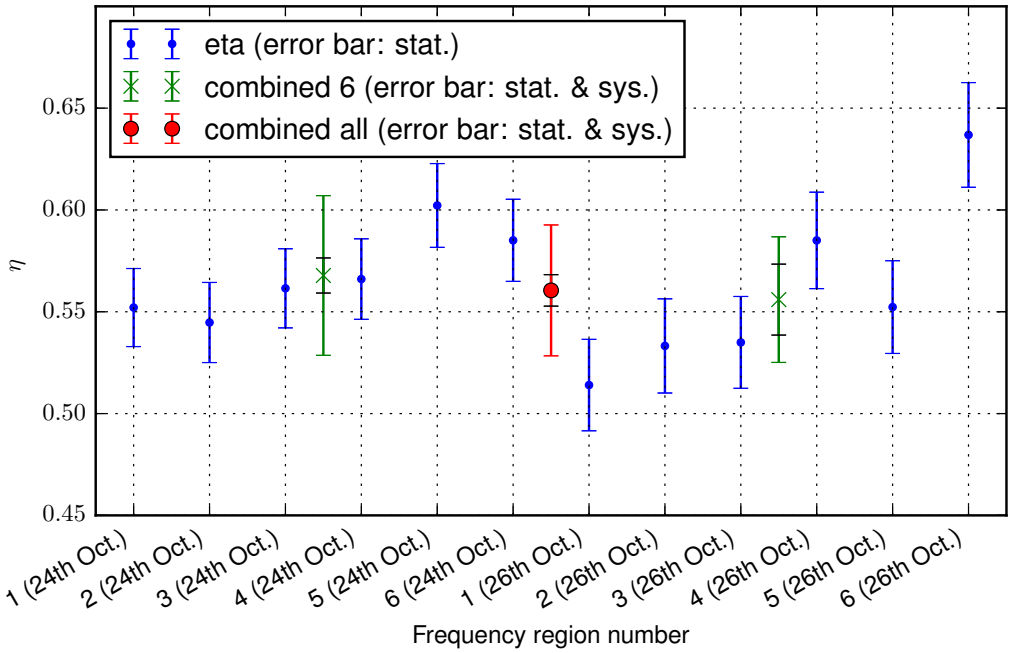

Figure 5.16: Measured results of the antenna efficiency (η) for each frequency region for each day. Small circles (blue) are individual results. Cross markers (green) are combined results for each day. The black error bars of combined results show the statistical error, and colored error bars include systematics from amplifier gain (G), sky temperature ($T_{\rm sky}$), and black body source temperature ($T_{\rm BB}$). The statistical error is larger in 26th Oct, whereas the systematic error is larger in 24th Oct. A large circle marker (red) is all combined result including systematic errors of solid angle (Ω). The result $\eta = 0.560 \pm 0.032$ is consistent with the typical value for conical horn antenna (≈ 0.5).

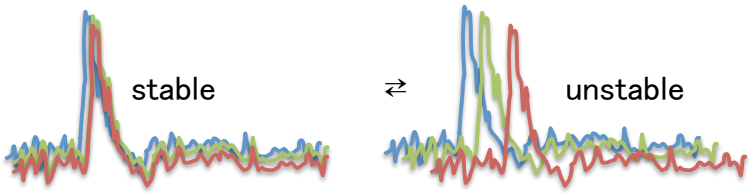

Figure 5.17: Schematics about the effect of frequency response instability. If the frequency response is stable (left), the noise component is averaged out with multiple runs. On the other hand, if the frequency response is unstable (right), the HPCDM peak is smeared out. This results in the bias to the power of the signal.

5.3 Frequency response

The frequency response is important because of following two reasons,

- Instability for the frequency response potentially smear the height of the signal shape, as shown schematically in Fig. 5.17. It results in inefficiency for the mixing angle χ,
- The signal peak represents the HPCDM mass.

The signal analyzer is the only unit to vary the frequency response. A built-in oscillator used for down conversion of input signals is the most critical part to cause such instabilities. This is because that the oscillator is sensitive for the variation of the ambient temperature in general. In this section, we first quote the uncertainty of the absolute value. Then we measure the instability of frequency response of spectrum analyzer, using a signal source.

5.3.1 Absolute uncertainty

For spectrum analyzer

For the absolute value, the catalog specification is the most conservative number of its systematic uncertainty. From Tab.3.6, we obtain

$$\begin{aligned}\Delta\nu_{\text{abs}} &\leq \nu \times [(\text{the time from last measurement}) \times (\text{aging rate}) \\ &\qquad + (\text{initial accuracy})] \\ &= 28\text{GHz} \times [2\ \text{year} \times (1 \times 10^{-6}/\text{year}) + 1.4 \times 10^{-6}] \\ &= 95\text{kHz}.\end{aligned}$$

For calibration source

Here we also quote the absolute uncertainty of Vector Network Analyzer (N5224A, Agilent), which we use as a signal source in the instability measurement. The relevant specification of the source is summarized in Table 5.6. We expect absolute frequency precision to be less than

$$\begin{aligned}\Delta\nu_{\mathrm{abs,VNA}} &\leq \nu \times [(\text{the time from last adjustment}) \times (\text{aging rate}) \\ &\qquad + (\text{initial accuracy})] \\ &= 28\mathrm{GHz} \times [2\ \text{year} \times (0.1 \times 10^{-6}/\text{year}) + 1 \times 10^{-6}] \\ &= 34\mathrm{kHz}.\end{aligned}$$

This is the upper bound of the calibration, which corresponds to the uncertainty of the HPCDM mass as follows,

$$\Delta m_{\gamma'} = h \times \Delta\nu_{\mathrm{abs,VNA}} = 1.4 \times 10^{-10}\mathrm{eV}. \tag{5.13}$$

The drift of the generated signal from the VNA is guaranteed to be very small. Therefore, we ignore the frequency drift of signal source [1].

5.3.2 Instability

We evaluate effects associated with the ambient temperature change. We monitor the measured frequency with changing the ambient temperature while the signal generator is maintained in the stable condition. The spectrum analyzer has a built-in thermometer. The setup of this calibration is shown in Fig. 5.18. The settings of the spectrum analyzer is identical to them for HPCDM search. We use a Vector Network Analyzer (N5224A, Agilent) as a signal source. The instability of the output signal is negligible as shown in Table 5.6. We generate a monotone signal at 28.003 GHz, of -30 dBm. We insert an attenuator of 10 dB at the input port of the spectrum analyzer.

Measurement

We measured the uncertainties for the frequency response on 5th Dec. 2016 (5.19 and 5.20). Shutter was opened a 11:05 to lower the temperature around the spectrum analyzer. The temperature inside spectrum analyzer changed from 40.25 to 27.75 ℃ (Fig. 5.21). The rate of temperature change is about 30 ℃/hour, which is tighter condition compared with the condition for the

[1] if we still calculate it, $\Delta f_{\mathrm{drift,VNA}} = 1.4\mathrm{kHz}$, for temperature from -10 to 70 ℃.

HPCDM search (0.8℃/hour) as shown in Fig. 6.34. During this measurement, the peak position remained the 1 kHz frequency bin (Fig. 5.22). The difference between the frequency specified by source and the frequency reported by spectrum analyzer is 1 kHz, which is much less than $\Delta\nu_{\mathrm{abs,VNA}}$ = 34 kHz. We also conclude the frequency stability is below 1 kHz. This corresponds to 0.9% uncertainty for the power of HPCDM signal, which is negligible as discussed in 6.5.5.

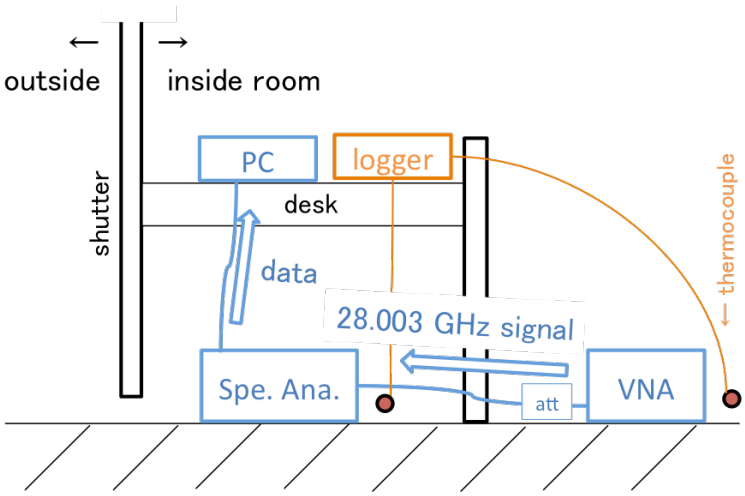

Figure 5.18: Schematics of the setup for frequency instability. VNA generates a monotone wave of 28.003 GHz. The spectrum analyzer measures attenuated signal at -40 dBm. The VNA was maintained in the stable room temperature condition. Temperature of the spectrum analyzer was varied by opening and closing of the shutter. The cold air entered there by opening it.

Description	Specification	Typical
Frequency range	10 MHz – 43.5 GHz	
Frequency resolution	1 Hz	
Frequency accuracy	±1 ppm	
Frequency stability		± 0.05 ppm, −10 – 70 ℃
		± 0.1 ppm/year max.

Table 5.6: Relevant specification of the Vector Network Analyzer (N5224A, Agilent) used as signal source.

Figure 5.19: Picture of the setup described in Fig. 5.18. The front instrument is VNA used as generate a monotone signal. Spectrum analyzer is under the desk, and surrounded by boards. The shutter in the back was opened to lower ambient temperature around the spectrum analyzer.

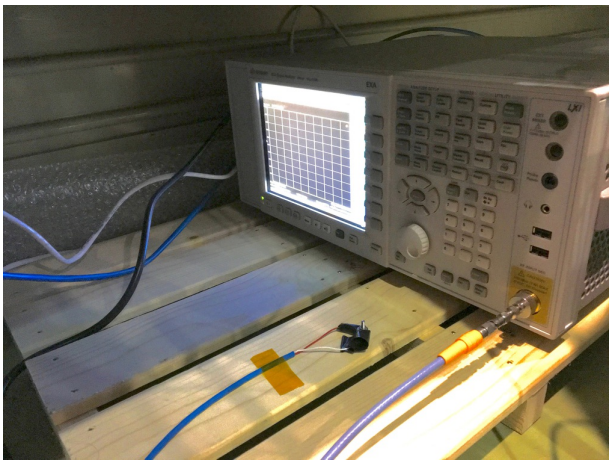

Figure 5.20: Picture of spectrum analyzer under the desk in Fig.5.19. A thermocouple to measure environmental temperature is also shown (the temperature shown in Fig. 5.21 is not from this thermometer, but one built in the spectrum analyzer).

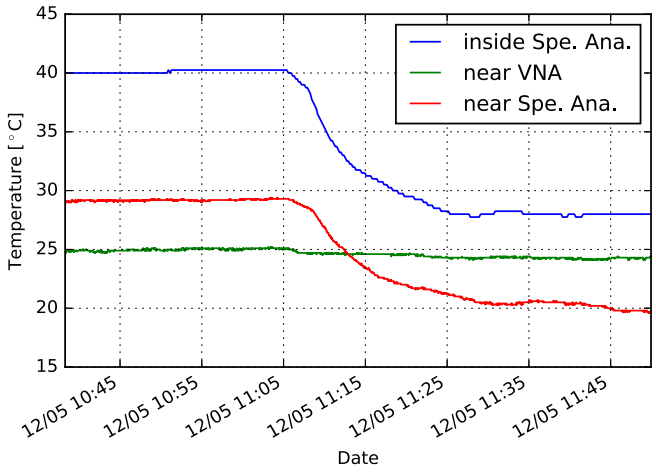

Figure 5.21: The temperature inside the spectrum analyzer during the frequency precision measurement. The temperature dropped as the shutter near the spectrum analyzer was opened at 11:05. Also the ambient temperatures near the spectrum analyzer and signal source (VNA) are shown.

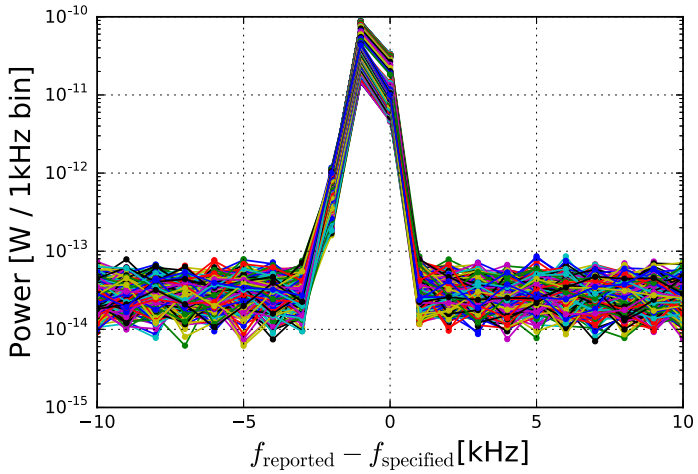

Figure 5.22: The data corresponding to Fig. 5.21. The horizontal axis is difference between the frequency specified by source and the frequency reported by spectrum analyzer. The absolute frequency precision is 1 kHz, which is within the specification of spectrum analyzer and VNA. The instability of frequency position is less than 1 kHz.

Chapter 6

Analysis and systematic errors

In this chapter, we describe the methodology of analysis and systematic errors.

6.1 Data selection

To ensure the quality of measurement data, we selected out runs by the following three selection criteria.

1. Responsivity is stable within ± 7.7%

   We require that the drift of the responsivity is less than the uncertainty of CDM density, 7.7% ($\rho_{\mathrm{CDM,local}} = 0.39 \pm 0.03 \mathrm{GeV/cm^3}$). We employ the linear interpolation model for the responsivity application to data. The conservative boundary condition is selecting runs whose responsivity varied less than ± 7.7 % from the middle of run. It corresponds to the less than 0.64 dB change. The changes between two successive calibrations are shown in Tab. 6.1.

2. Measured power is stable within 7.7%

   Instability of weather change the condition of measurement. We selected runs where the ratio max(power) / min(power) < 1.077.

3. Receiver temperature is stable within 7.7%

   The receiver temperature should be stable. Large change of it indicates malfunctions of the system such as dew condensation of the aperture window. We select runs receiver temperature smaller than 1.077 of (the minimum number in all calibrations).

Calibration Dates \ Region #	The systematic error for amplifier gains [%] 1	2	3	4	5	6	
2016-10-26 16:31:28, 10-26 19:28:57	3.52	3.02	2.58	2.42	3.62	3.30	
2016-10-26 19:28:57, 10-26 21:54:51	1.96	1.99	1.48	2.95	1.64	2.08	
2016-10-26 21:54:51, 10-27 04:50:51	10.70	10.95	11.06	11.29	11.19	11.24	
2016-10-27 04:50:51, 10-27 07:29:45	1.09	1.42	1.61	2.17	1.28	1.44	
2016-10-27 07:29:45, 10-27 12:00:22	10.91	10.96	10.96	10.23	11.16	11.15	
2016-10-27 12:00:22, 10-27 14:26:36	0.76	0.83	0.30	1.18	0.50	0.20	
2016-10-27 14:26:36, 10-27 16:44:08	4.29	4.54	4.78	4.76	4.17	3.93	
2016-10-27 16:44:08, 10-27 18:34:39	9.52	9.44	8.78	9.01	9.10	9.39	
2016-10-27 18:34:39, 10-27 19:39:13	0.68	0.59	1.23	1.75	1.81	1.93	run 1
2016-10-27 19:39:13, 10-27 21:34:22	2.72	3.49	2.28	2.60	2.43	2.17	run 2
2016-10-27 21:34:22, 10-27 23:41:04	1.74	0.99	1.66	1.44	1.29	1.28	run 3–5
2016-10-27 23:41:04, 10-28 02:03:32	5.13	5.40	5.50	4.32	5.16	5.51	run 6
2016-10-28 02:03:32, 10-28 03:03:29	2.38	2.18	2.30	2.83	2.63	2.27	run 7
2016-10-28 03:03:29, 10-28 04:03:42	0.29	0.67	0.87	0.17	0.52	0.05	run 8
2016-10-28 04:03:42, 10-28 05:30:38	1.20	0.92	1.38	1.65	1.01	2.16	run 9
2016-10-28 05:30:38, 10-28 07:01:18	1.05	1.58	1.71	1.58	1.89	2.45	
2016-10-28 07:01:18, 10-28 08:33:58	3.55	2.92	3.61	3.34	2.49	3.25	
2016-10-28 08:33:58, 10-28 10:05:34	0.51	0.35	0.15	0.11	0.64	0.25	
2016-10-28 10:05:34, 10-28 11:34:20	0.22	0.64	1.13	1.49	0.66	0.77	

Table 6.1: The systematic error for gains, calculated as half of difference between two successive gain calibration results, for each of 6 frequency regions. They are less than 7.7 % for selected runs. For raw values of gain, see Tab. 5.1.

We select 9 runs for our analysis (Tab. 6.2). The system temperature as a function is shown in Fig. 6.3. Background noise level is maintained to be low and stable for the selected runs. We repeat a series of measurements of 6 frequency regions as mentioned in Sec. 4.2. We average the data for each region for each run, i.e., we have 6 sub-runs for each run. Therefore, we have 54 sub-runs in total. Examples of the data for sub run is shown in Fig. 6.2. The noise characteristic for them is shown in Fig. 6.3, by checking the data in Fourier space.

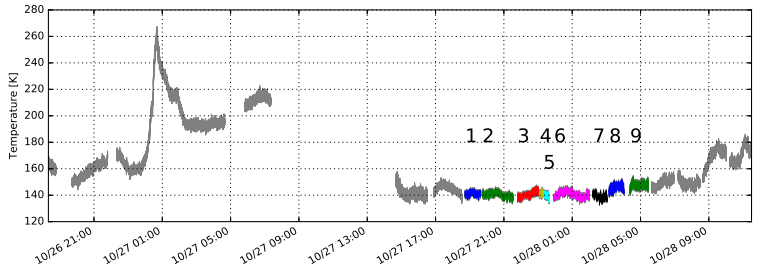

Figure 6.1: Loading temperature $T_{\mathrm{load}} = T_{\mathrm{sys}} - T_{\mathrm{rec}}$ as a function of time. Selected data sets are indicated with color points. Data selection ensures low background noise condition as well as the stability of data.

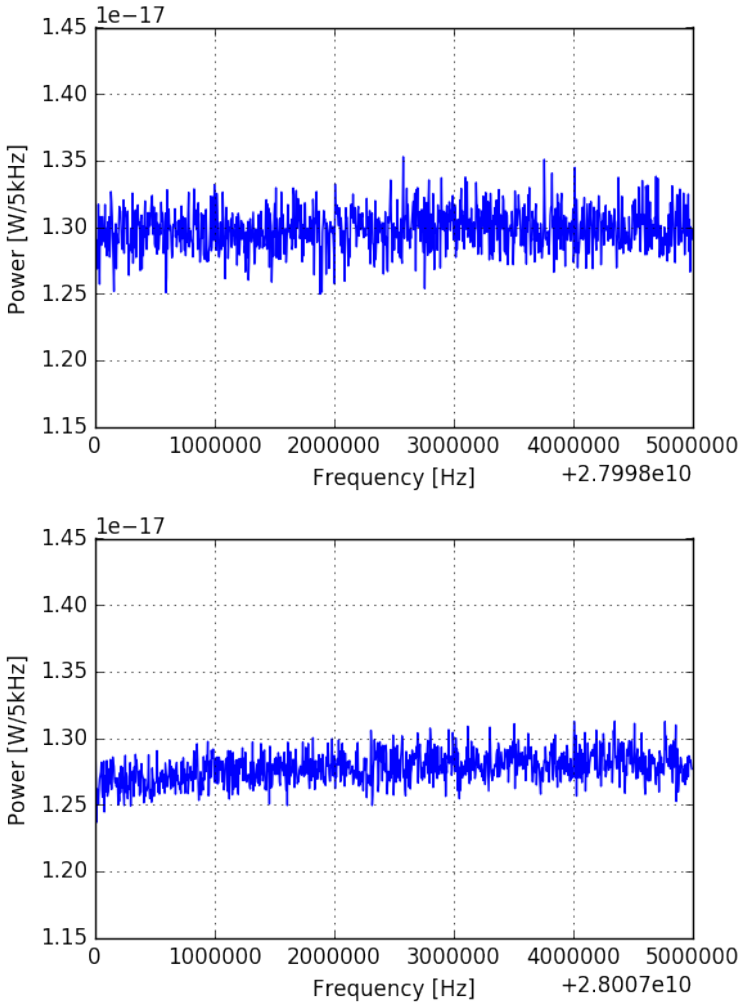

Figure 6.2: Examples of selected data. Top is subrun 1 (run 1, frequency region 1) and bottom is subrun 12 (run 2, frequency region 6).

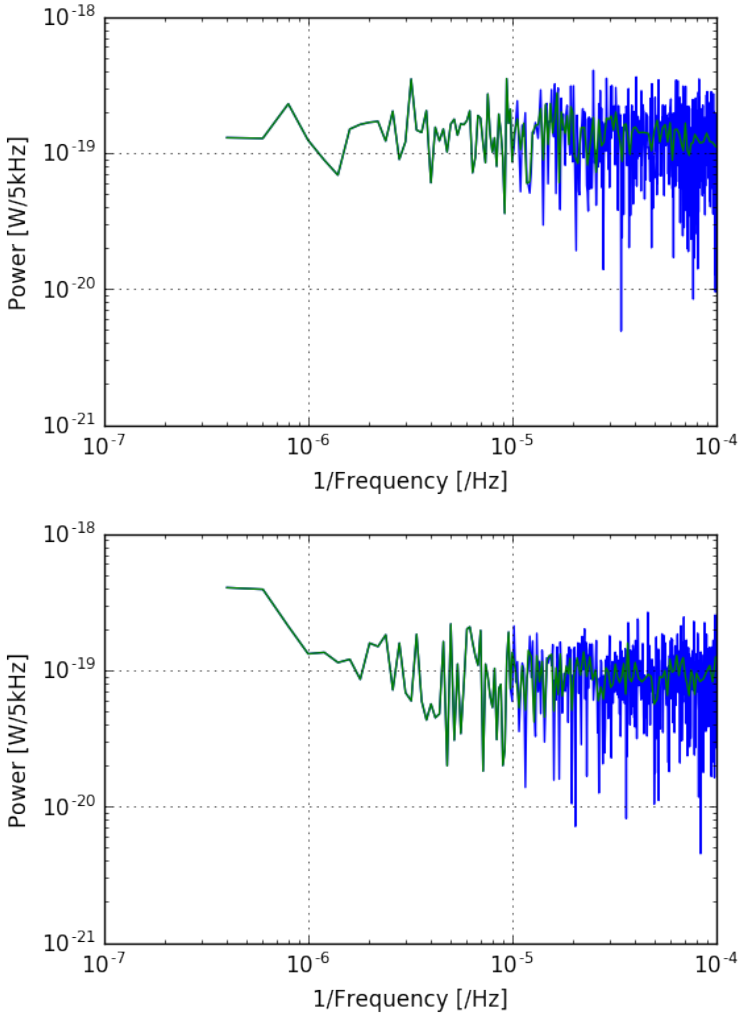

Figure 6.3: The data of Fig. 6.2, viewed in Fourier space to check noise characteristics. The Fourier transformed spectra are shown in blue. Green is averaged spectrum to be smooth. Top figure is for subrun 1 (run 1, frequency region 1) and bottom is for subrun 12 (run 2, frequency region 6). For white noise, this flat spectrum is expected. We see an effect of drift in bottom panel, as a slope upward to the left. The average of rightmost 200 points ($\gtrsim 6\times10^{-5}$ /Hz) is identified as the level of white noise, and used as measurement error in fitting HPCDM peak.

run #	started time	number of repeats
1	2016-10-27 18:44:10	301
2	2016-10-27 19:44:05	603
3	2016-10-27 21:48:05	406
4	2016-10-27 23:05:56	56
5	2016-10-27 23:18:57	118
6	2016-10-27 23:56:08	692
7	2016-10-28 02:13:07	274
8	2016-10-28 03:10:00	291
9	2016-10-28 04:23:03	363

Table 6.2: Selected runs for the analysis. It takes 12 seconds to measure the data for 6 regions. We continuously repeat this data taking. Number of repeats between responsivity calibrations is almost proportional to the length of run.

6.2 Methodology of signal extraction

6.2.1 Extraction for each sub-run

We extract the HPCDM signal by the least-square fit for each sub-run. For HPCDM signal we use binned probability density function (PDF) with the analysis bin width (5 kHz): $f_{\rm sig}(\nu)$. We model the baseline gradient (i.e., background noise distribution) with one dimensional polynomial, $a\nu + b$, where a and b are floating parameters. We extract powers of HPCDM signal (P) for each frequency (ν_0) by using following PDF,

$$f(\nu; P, a, b; \nu_0) = P \cdot f_{\rm sig}(\nu; \nu_0) + (a\nu + b). \tag{6.1}$$

The peak shape depends on the hidden photon mass $m_{\gamma'}$, and we use the peak shape using $m_{\gamma'}$ corresponding to the bin ($m_{\gamma'} = \nu_0$). An example of the fit with Monte Carlo data is shown in Fig. 6.4. Fit range is 240 kHz; 60 kHz to the left, and 180 kHz to the right. We use 48 bins for fit. For measurement error, we used the white noise component of the data, by using the average of rightmost 200 points in Fourier space (Fig. 6.3, 6.8). We assume the measurement error is same for all bins. We scan the signal powers with changing ν_0 in the range of each sub-run data. We obtain the powers ($P \pm \Delta P$) for each frequency.

6.2.2 Accumulation of results for each sub-run

We combine the results of each sub-run. We simply take weighted average of for each frequency [3]. Suppose we have a set of measurement results,

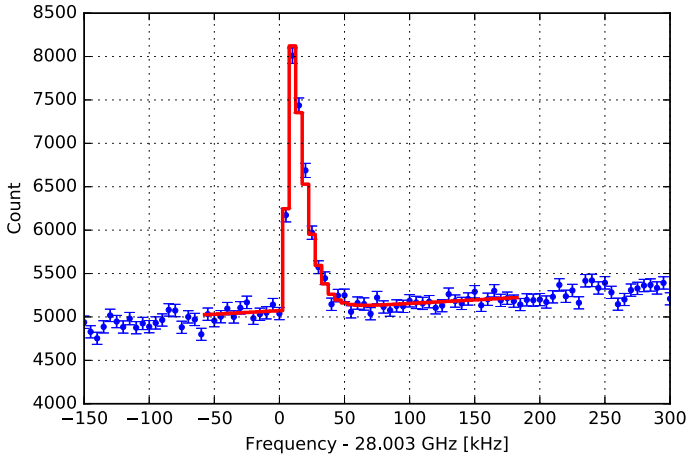

Figure 6.4: An example of fit (red solid line) for Monte Carlo data (blue points) based on PDF of Eq. (6.1). The fit range is 60 kHz (12 bins) to the left of peak and 180 kHz (36 bins) to the right of the peak, 48 bins in total.

$x_i \pm \delta x_i$ and we want to combine them. We calculate it by the standard weighted average,

$$\bar{x} \pm \delta\bar{x} = \frac{\sum_i w_i x_i}{\sum_i w_i} \pm (\sum_i w_i)^{-1/2}. \tag{6.2}$$

Then, we calculate $\chi^2 = \sum w_i(\bar{x} - x_i)^2$ to check the consistency among the values. The expected value for χ^2 is $N-1$ for measurement with Gaussian error. We check compare the value $\chi^2/(N-1)$ with 1. If $\chi^2/(N-1) \gg 1$, we associate the result as unaccounted systematic error, and rescale the error $\delta\bar{x}$ by a factor

$$S = [\chi^2/(N-1)]^{1/2}. \tag{6.3}$$

If S $\gg$ 1, the results are not statistically consistent. There are three possible cases under this situation[41].

- some (or all) results are wrong,
- some (or all) results have underestimated errors,
- the results do not represent the same quantity (systematic errors).

Though it is best to resolve these contributions, it is not straightforward. In our case, we cannot investigate them before unblinding results, and transient

spike noises may have some effects on results. We cannot determine their contributions only from statistics, therefore we assume all results have underestimation in their errors and multiply by the same scale factor S. Note the central value $\bar{x}$ is not affected by this procedure.

The distribution of scale factor S

Let us assume errors are underestimated for all results. If we write $S = \max(1, S_+) \equiv \max(1, \sqrt{\chi^2_{k=N-1}/(N-1)})$. When X_i is independent random variables which follow standard normal distribution,

$$Y_k = \sqrt{\sum_{i=1}^{k} X_i^2} \tag{6.4}$$

is referred to as chi distribution. Chi distribution is the square root of chi-squared distribution.

Assume we have N independent normally distributed random variable, with the common mean $\mu = 0$ and standard deviation δx_{true}. When we take the weighted average assuming the error δx_{given}, S_+ obeys chi distribution times a factor:

$$S_+ \sim Y_{N-1} \cdot \frac{1}{\sqrt{N-1}} \cdot \frac{\delta x_{\text{true}}}{\delta x_{\text{given}}} \tag{6.5}$$

$$(= \sqrt{(\text{reduced chi square})} \cdot \frac{\delta x_{\text{true}}}{\delta x_{\text{given}}}). \tag{6.6}$$

We examined the distribution of S by toy Monte Carlo samples. We use 50 random variable, with the mean $\mu = 0$ and standard deviation $\delta x_{\text{true}} \neq 1$. We apply weighted average assuming error to be 1 ($\delta x_{\text{given}} = 1$). We use 1000 different seeds to obtain the distribution of S. The result for $\delta x_{\text{true}} = 0.95$ (overestimation of error) and $\delta x_{\text{true}} = 1.05$ (underestimation of error) are shown in Fig. 6.5. The distribution of S has a sharp peak at 1 for the case of overestimation (no rescaling). On the other hand, S corrects the error in the case of underestimation.

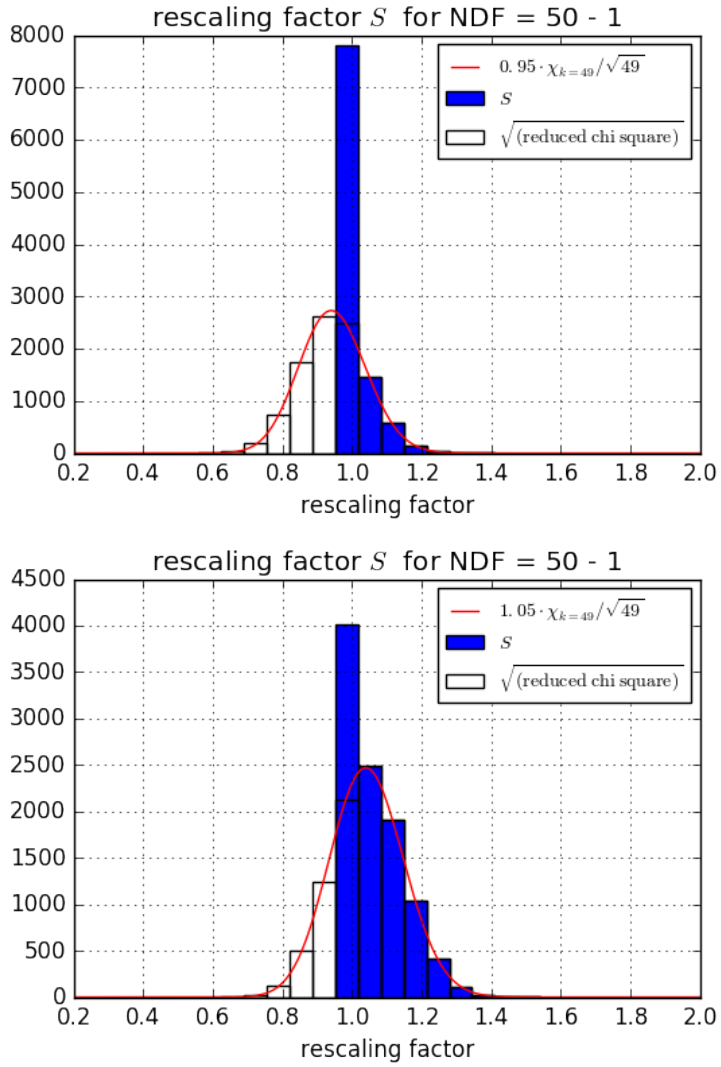

Figure 6.5: The distribution of the scale factor S from toy Monte Carlo simulation, with wrong errors. The blue histogram shows the distribution of S. The blank histogram shows the distribution of S_+, which is not clipped at 1. The red curve shows the chi distribution, which describes S_+.

6.3 Validations prior to unblinding results

6.3.1 Null tests

Validation tests before opening the box are sometimes useful to check hidden systematics in data. We make "null sample" as shown in Fig. 6.6. We use the null samples for the analysis validation. We confirm stationarity of data quality among sub-runs (Fig. 6.14) as well as the no bias in the null samples. The example of null samples are shown in Fig. 6.7. Their noise characteristic is shown in Fig. 6.8, by checking the null sample in Fourier space.

Figure 6.10 shows the combined results of 2752 points of P and ΔP. We use this result for checking possible biases in our analysis. We use the fact the fitting result should be zero-consistent if there is no signal. We want to check

- fit result P is not biased from zero.
- the error distribution is as expected ($P/\Delta P$ is symmetric).
- if there is effect of accidental spike noises.

Figure 6.9 shows the distribution of error, $P/\Delta P$. We fit this histogram using bins ≥ 10 counts, and obtained the average $\mu = -0.002 \pm 0.020$ and standard deviation $\sigma = 0.998 \pm 0.015$. This is consistent with standard Gaussian distribution. with There are three points with $P/\Delta P > 3$, which agrees well with 3.7 from 2752 points from standard Gaussian distribution. The regions around these three "peaks" are shown in Fig. 6.11–6.13.

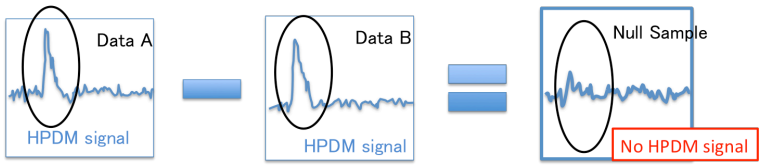

Figure 6.6: Schematics of null sample. We divide measurement data in a run into two, and subtract one from another. The noise remains. However, HPCDM signal is canceled out in this "null sample". We can increase number of noise-only samples by changing the criteria to divide the data.

Stationarity of the width of $P/\Delta P$ distribution

For the same motivation with the check of χ^2, we further checked outliers. by checking the distribution width of $P/\Delta P$ i.e. std($P/\Delta P$). We compare it

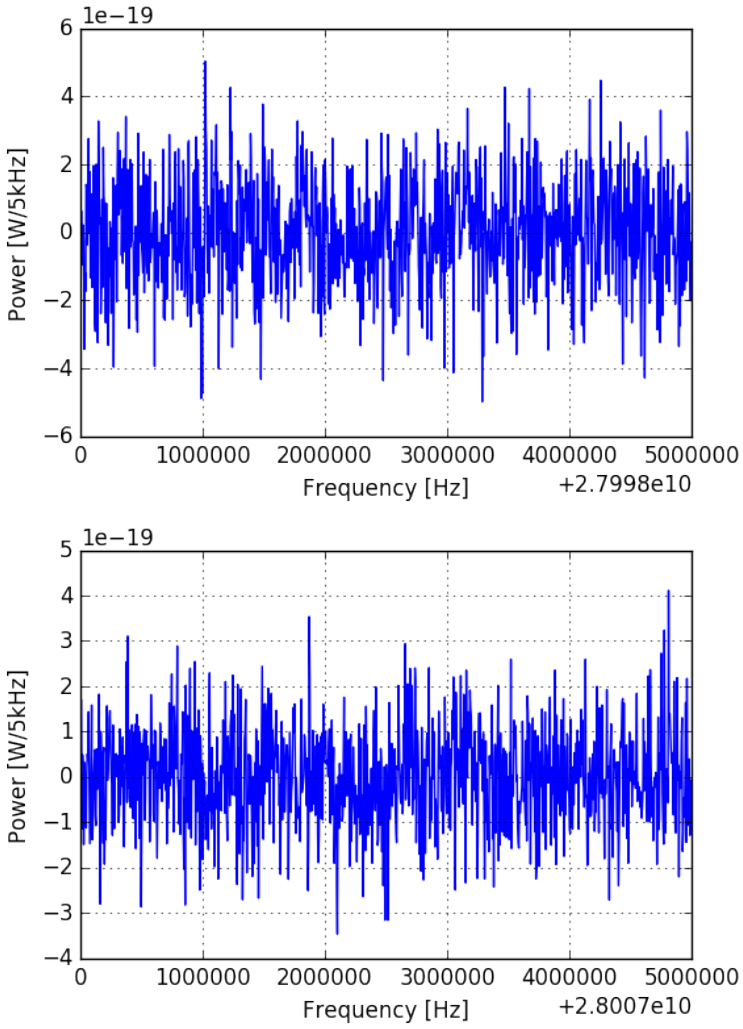

Figure 6.7: Examples of null sample. Top is a null sample made from data of subrun 1 (run 1, frequency region 1) and bottom is one from subrun 12 (run 2, frequency region 6).

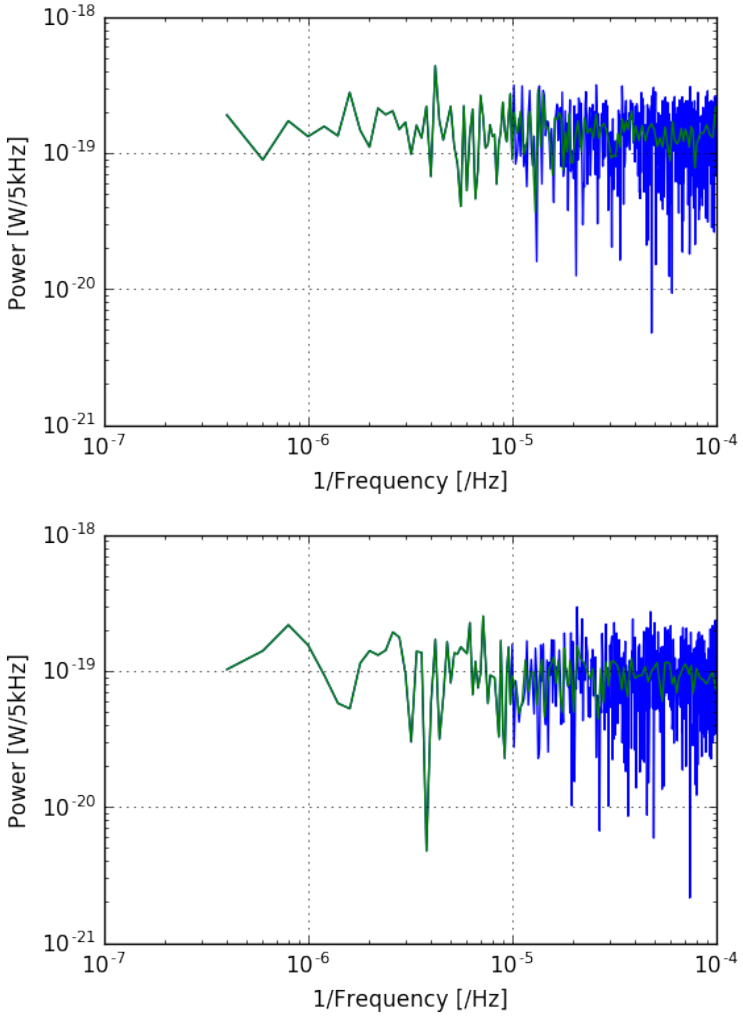

Figure 6.8: The null sample of Fig. 6.7, viewed in Fourier space to check noise characteristics. The Fourier transformed spectra are shown in blue. Green is averaged spectrum to be smooth. Above is subrun 1 (run 1, frequency region 1) and bottom is subrun 12 (run 2, frequency region 6). For white noise, this spectrum is flat. The average of rightmost 200 points ($\gtrsim 6 \times 10^{-5}$ /Hz) is considered as the level of white noise, and used as measurement error in fitting HPCDM peak.

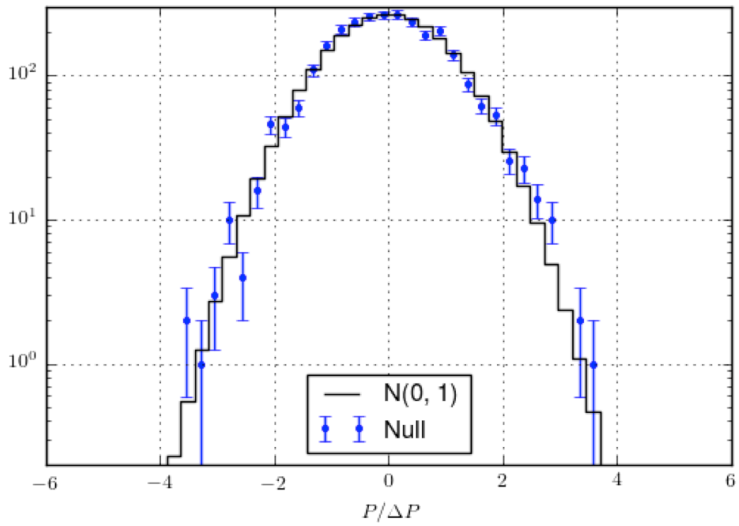

Figure 6.9: The $P/\Delta P$ distribution for fitting results in Fig. 6.10. It is fitted with Gaussian distribution $N(\mu, \sigma)$ using bins with ≥ 10 counts, and obtained results is consistent with standard Gaussian distribution: $\mu, \sigma = -0.002 \pm 0.020, 0.998 \pm 0.015$.

with the same variable calculated for null data. We normalize the values using the first of 54 values, to see its stationarity among sub runs, without seeing effect of broadening of the distribution, which may be caused by outliers in $P/\Delta P$ distribution from HPCDM signal or common mode noise. We do not observe significant difference among the data and null samples as shown in Fig. 6.15.

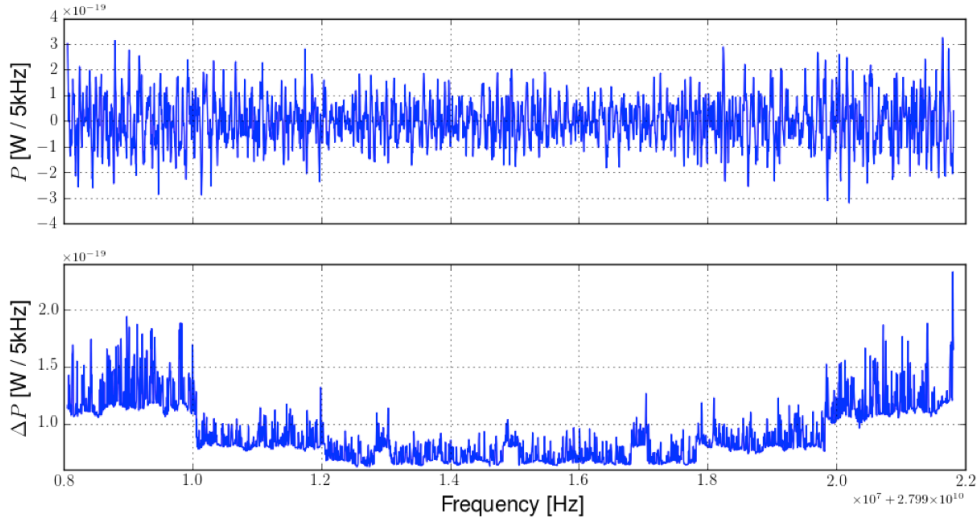

Figure 6.10: The combined results of 54 null samples. No significant power is observed in 2752 frequency bins. The level of ΔP reflects of difference of statistics from overwrapping of frequency range (Fig. 4.3)

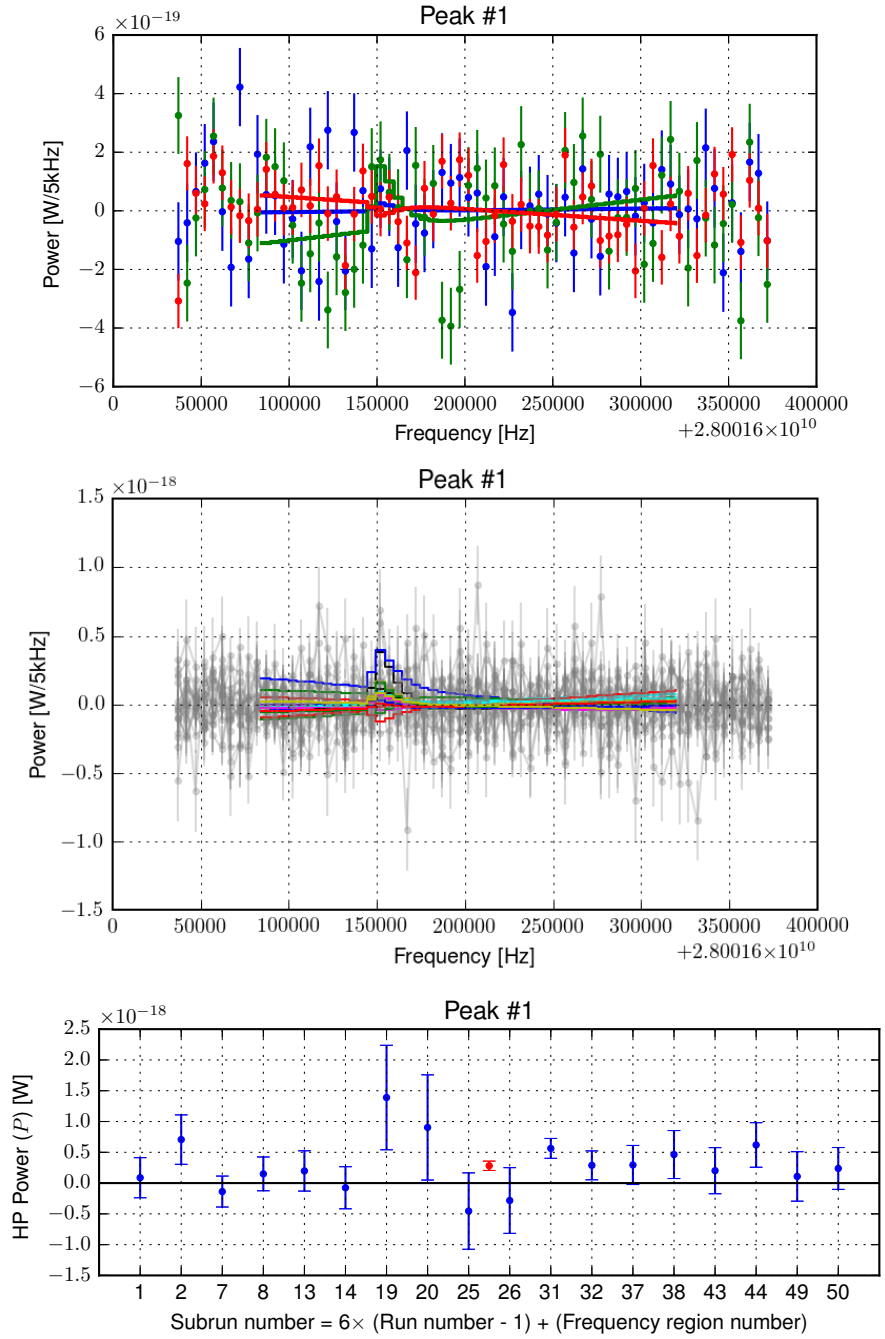

Figure 6.11: The fit results for #1 of 3 peaks exceeding 3σ for null sample. Top panel shows the first three subrun data in this frequency region (dot) and fitting results (solid line, the same color as data). The middle panel shows all subrun data in gray, and fit results in colored solid lines. The bottom panel shows fit results P, ΔP for each subrun in blue dots, and combined results in red.

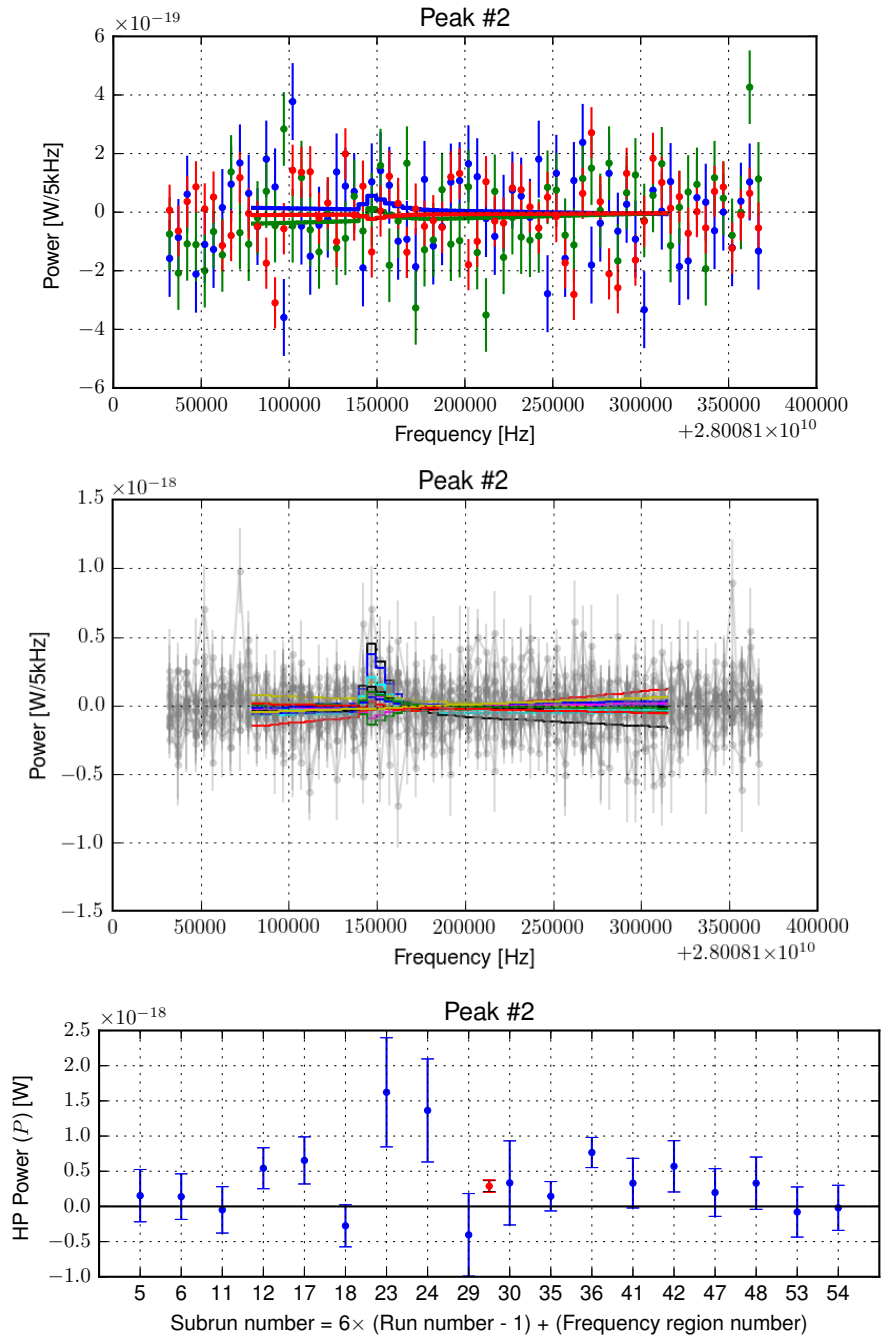

Figure 6.12: The fit results for #2 of 3 peaks exceeding 3σ for null sample. The top panel shows the first three subrun data in this frequency region (dot) and fitting results (solid line, the same color as data). The middle panel shows all subrun data in gray, and fit results in colored solid lines. The bottom panel shows fit results P, ΔP for each subrun in blue dots, and combined results in red. The error bar for combined results is rescaled by $S = 1.27$ (the error bar before rescaling is shown in black).

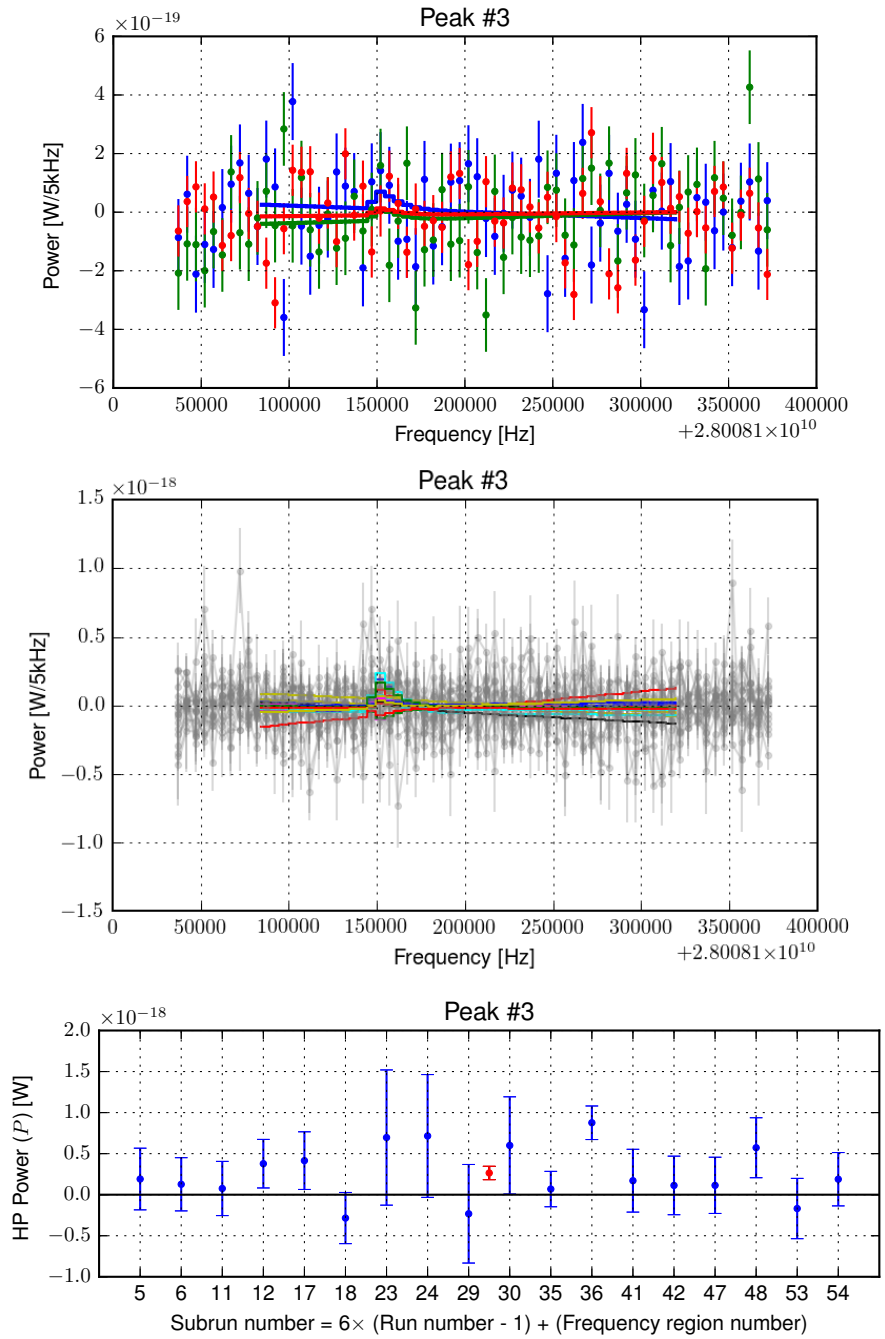

Figure 6.13: The fit results for #3 of 3 peaks exceeding 3σ for null sample. The top panel shows the first three subrun data in this frequency region (dot) and fitting results (solid line, the same color as data). The middle panel shows all subrun data in gray, and fit results in colored solid lines. The bottom panel shows fit results P, ΔP for each subrun in blue dots, and combined results in red. The error bar for combined results is rescaled by $S = 1.06$ (the error bar before rescaling is shown in black).

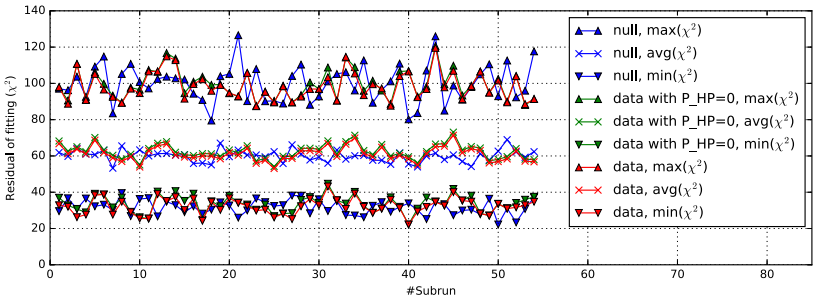

Figure 6.14: The chi-square plot for data sanity check. Max, average, minimum of about 100 values of χ^2 are designated by symbols $\triangle, \times$ and $\triangledown$ respectively. Results from different methods are compared: blue, red, green corresponds to null sample, data, data with modified fitting (P fixed to be zero). We observe no apparent discrepancy among sub runs.

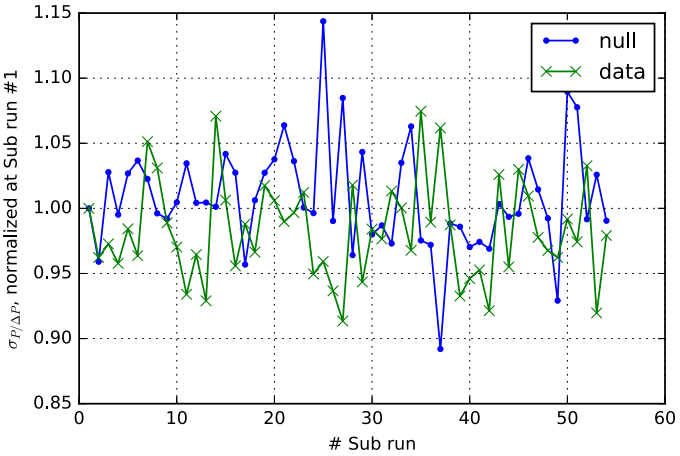

Figure 6.15: Widths of $P/\Delta P$ distributions, among 54 sub runs. We found no apparent outlier among them.

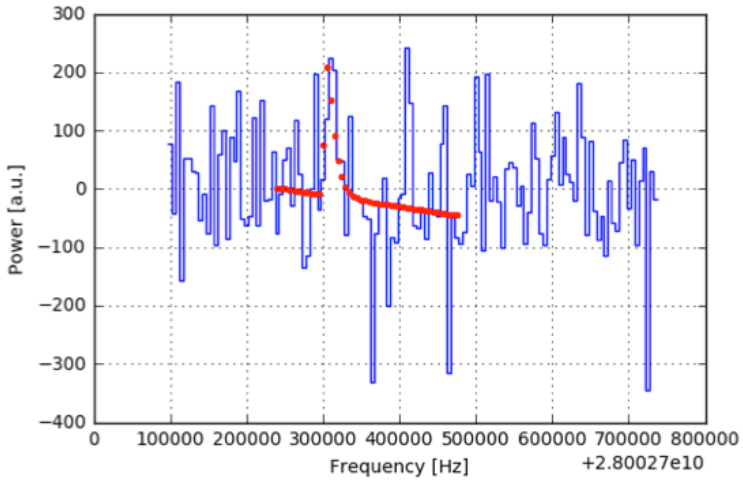

Figure 6.16: An example of generated MC data and fit. $P_{\text{given}} = 1000$ is used in this data.

6.4 Estimation of errors

We check if the fitting error ΔP represents the actual distribution of fitting results, using Monte Carlo samples.

6.4.1 White noise

We generate a Monte Carlo data of noise and HPCDM signal. First we assume white noise. We generate a Gaussian noise of width 100. We add the HPCDM signal of strength P_{given}. We change P_{given} and check the consistency between the fitting error ΔP_{fit} and the actual distribution std(P_{fit}). An example of data and fit is shown in Fig. 6.16. We use 6 different P_{given}: 0, 200, 400, 600, 800, 1000. We check the distribution of fit result P_{fit} using 1000 different random seeds. The histogram of the difference $P_{\text{given}} - P_{\text{fit}}$ for each P_{given} is shown in Fig. 6.17, 6.18. Figure 6.18 also shows the ratio of std(P_{fit}) and average(ΔP_{fit}). From these 6 points, std(P_{fit}) $= 246.4 \pm 0.4$ and average(ΔP_{fit}) $= 247.8 \pm 3.4$. Therefore the fitting error ΔP_{fit} is consistent with actual distribution.

6.4.2 Drift noise

Instruments like amplifiers and detectors suffer drift noise (1/f noise), in addition to white noise. It obeys power-law when viewed in Fourier space (which is obtained by re-Fourier transformation of the original FFT data), as

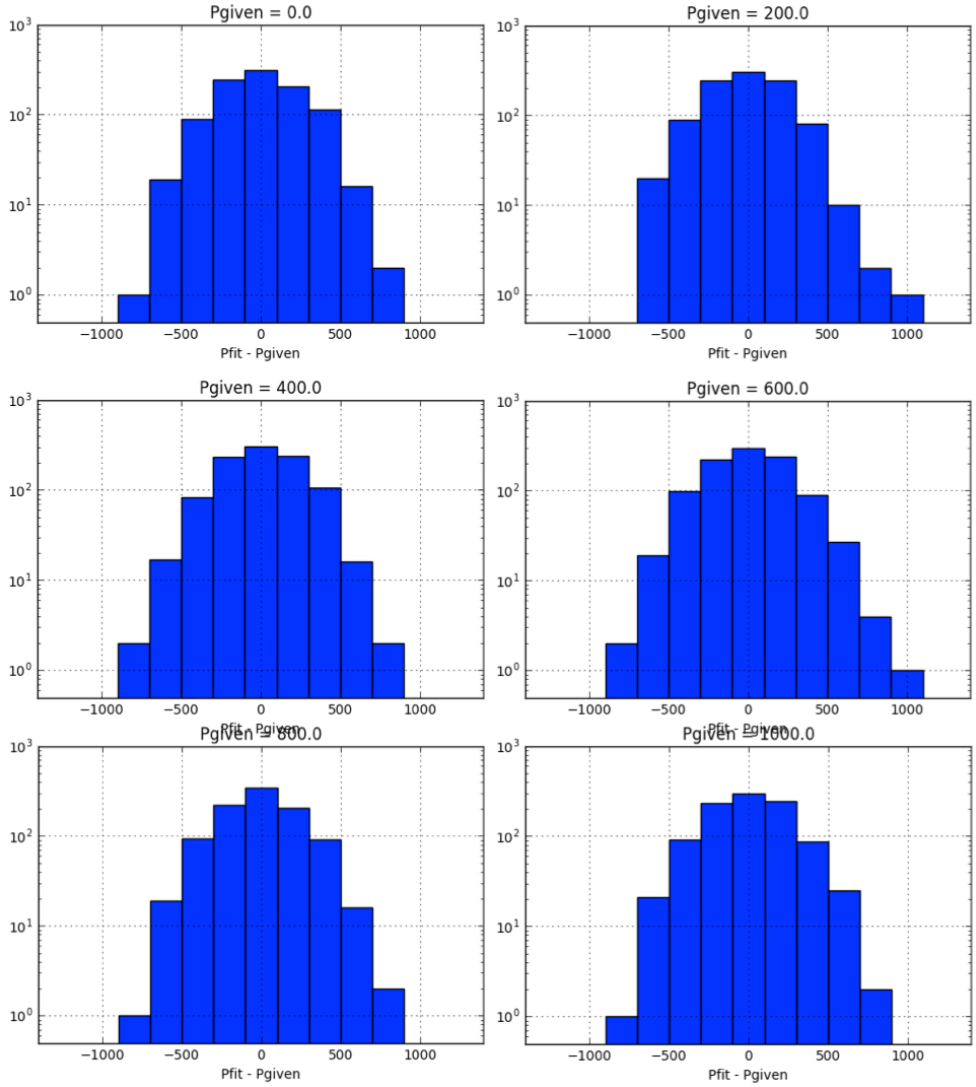

Figure 6.17: The difference of the given power P_{given} and the fit result P_{fit}, for each P_{given}., for white noise.

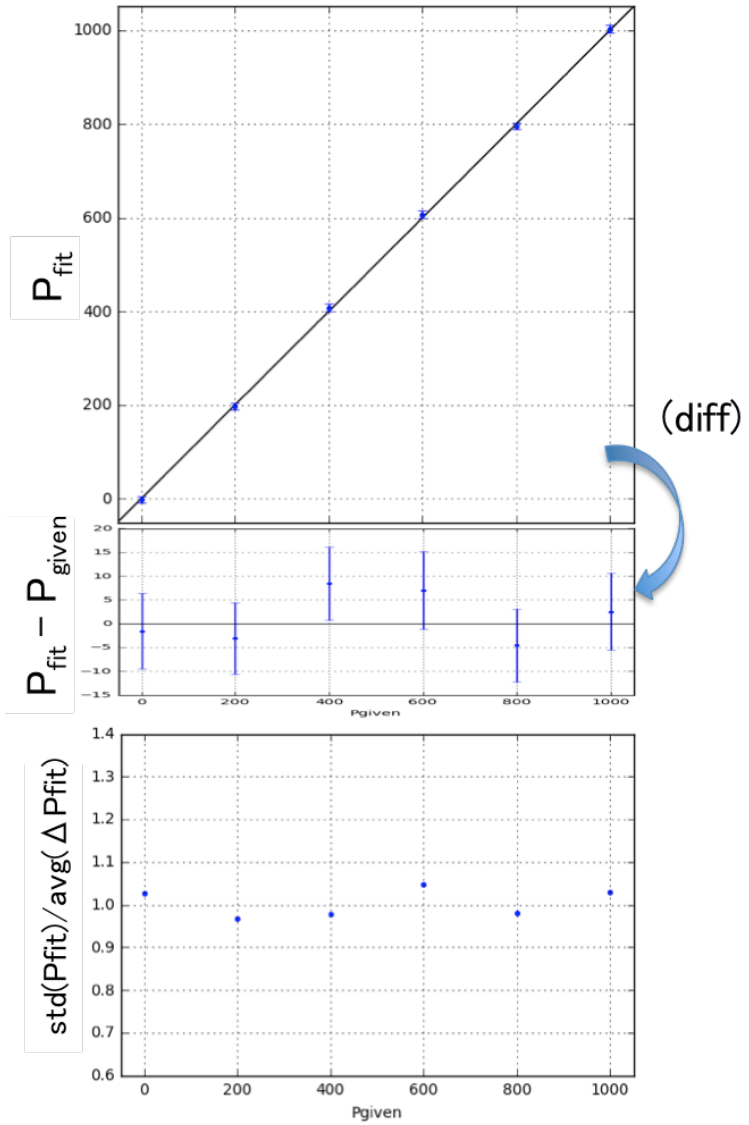

Figure 6.18: The fitting results for white noise Monte Carlo data. The top and middle panels show the consistency between P_{given} and P_{fit}. The bottom panel shows the actual distribution of P_{fit} and fitting error ΔP_{fit}. The fitting error is consistent with the actual distribution.

shown in Fig. 6.19. The index α typically have value between 1 and 2. The point where drift component reaches the same level as white noise is called "knee". The spectrum can be specified by two parameters i.e. α and the knee position, when white noise level is fixed. Figure 6.20 schematically shows how to generate drift noise. First we generate a white noise spectrum. Next we switch to Fourier space. Then we deform the spectrum by power-law. Finally we go back from Fourier space to obtain the drift noise.

We check the consistency between the fit error $\Delta P_{\rm fit}$ and the actual distribution of fit result by fitting Monte Carlo data. We combine three components to make the Monte Carlo data. The first and second are white noise with standard deviation 100 and HPCDM signal of $P_{\rm given}$, as same as Sec. 6.4.1. We add drift noise as the third component, with specified α and knee position. We use 7 different position of knee: 1/(50kHz), 1/(100kHz), 1/(200kHz), 1/(400kHz), 1/(800kHz), 1/(1600kHz), 1/(3200kHz). We use 3 different α: 1.0, 1.5, 2.0. We check the distribution of fit result $P_{\rm fit}$ using 1000 different seeds. We use 6 different $P_{\rm given}$: 0, 200, 400, 600, 800, 1000. We check the distribution of fit result $P_{\rm fit}$ using 1000 different random seeds. Figure 6.21 and 6.22 shows the case of $\alpha = 2.0$ and knee positions of 1/100kHz. In the presence of drift noise, the $P_{\rm given}$ is consistent with $P_{\rm fit}$. However, std($P_{\rm fit}$) is significantly larger than fitting error average($\Delta P_{\rm fit}$). Figure 6.23 shows the dependence of this deviation on drift knee and α. For small α, the discrepancy between $P_{\rm fit}$ and $\Delta P_{\rm fit}$ arises even when the knee is low.

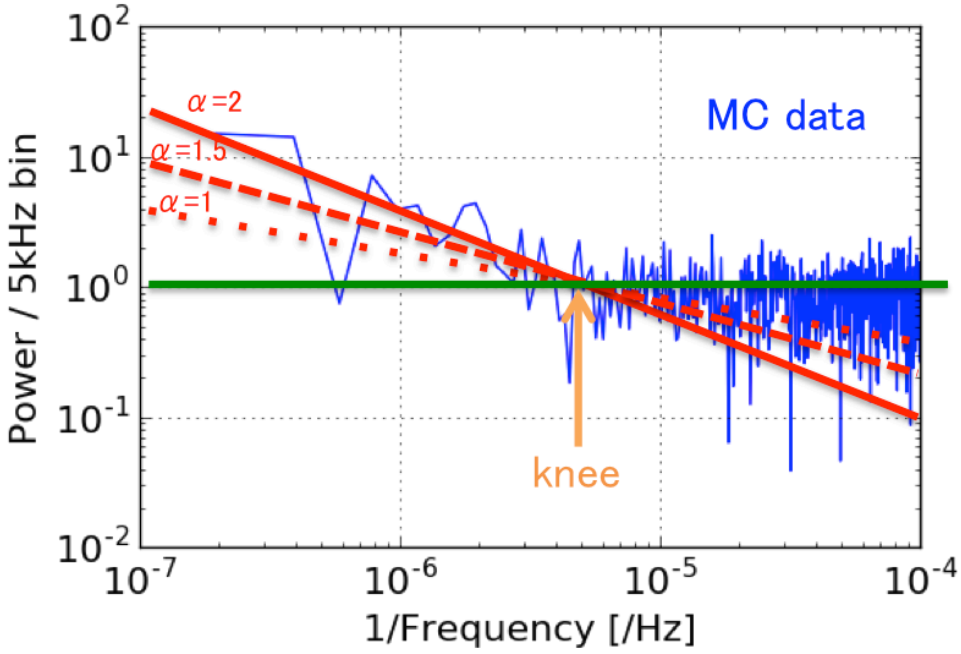

Figure 6.19: The schematic of drift noise in Fourier space (obtained by re-Fourier transformation of the original FFT data). The drift component (red) obeys power law. The index α typically have value between 1 and 2. The point where the drift component crosses white noise level (green) is called "knee".

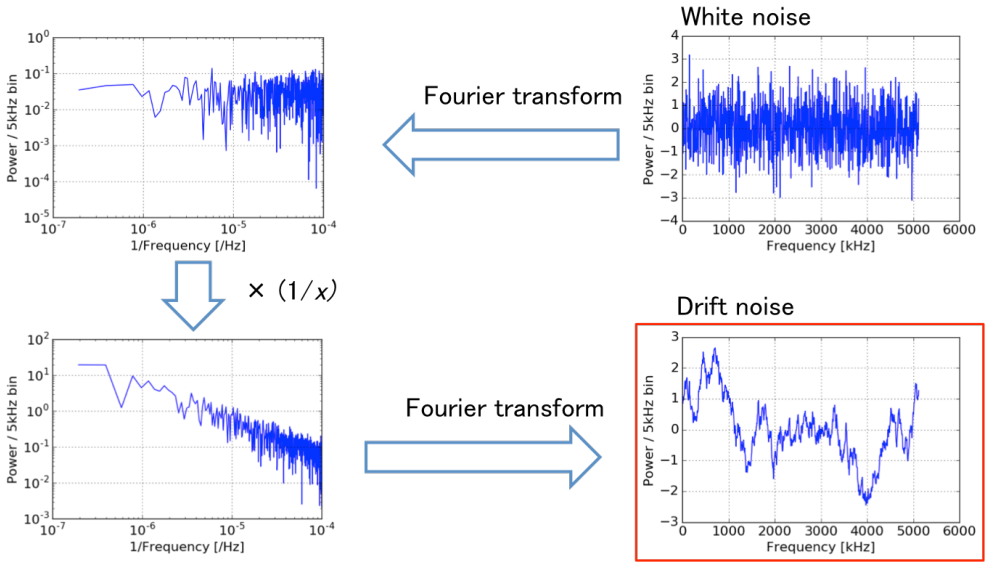

Figure 6.20: The schematic about generating drift noise.

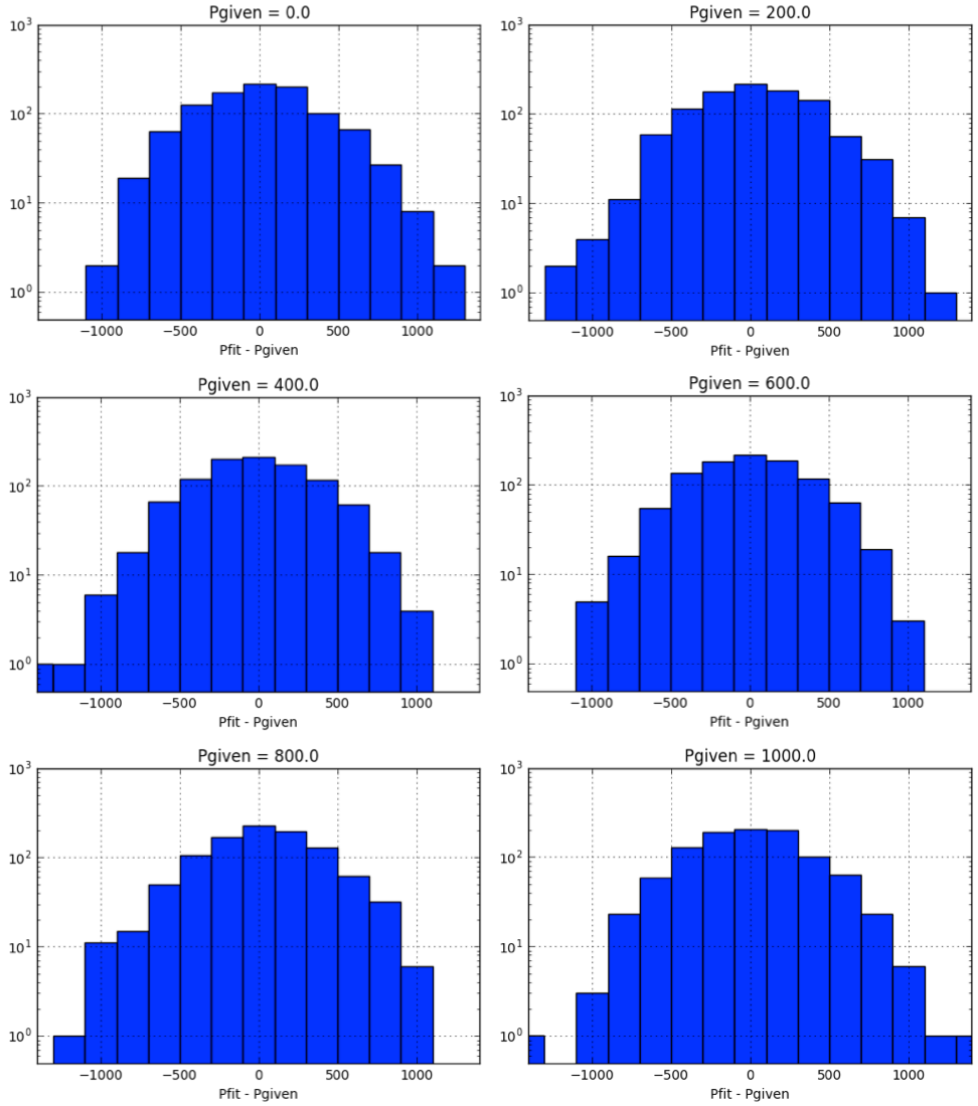

Figure 6.21: The difference of the given power P_{given} and the fit result P_{fit}, for each P_{given}. The MC data is composed of white noise (width 100), drift noise ($\alpha = 2$ and knee 1/100kHz), and HPCDM signal.

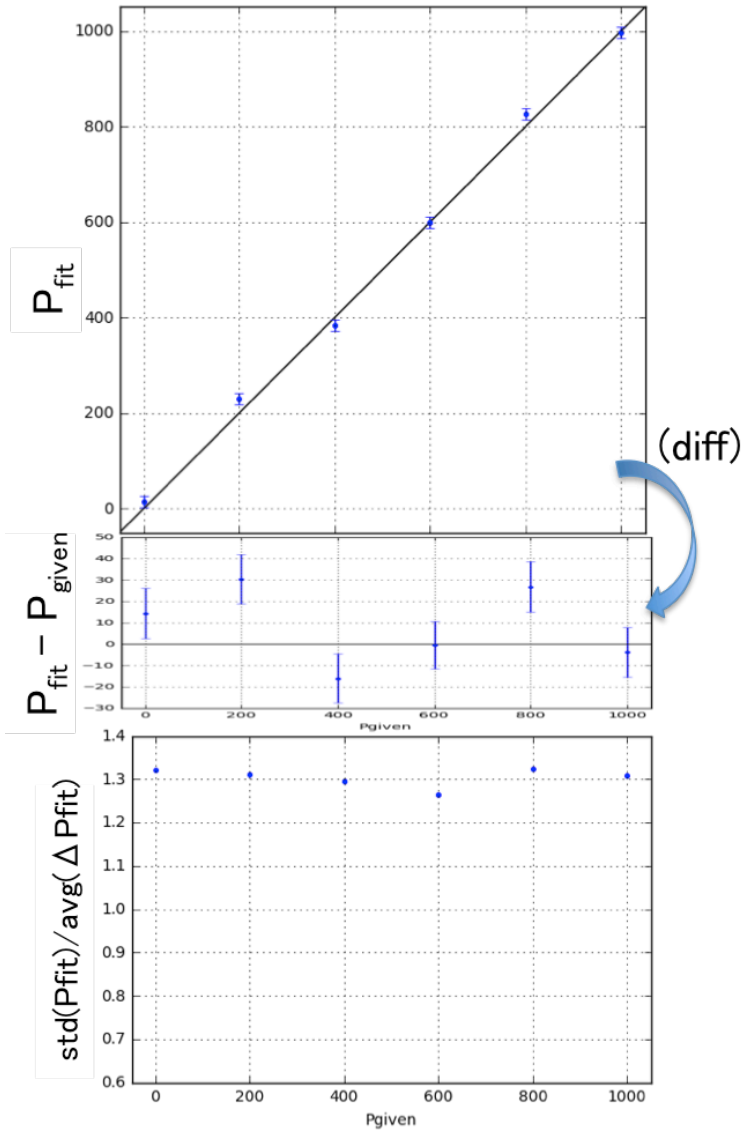

Figure 6.22: The fitting results for Monte Carlo data with drift noise ($\alpha = 2$ and knee 1/100kHz). The top and middle panels show the consistency between P_{given} and P_{fit}. The bottom panel shows the actual distribution of P_{fit} and fitting error ΔP_{fit}. Contrary to the white noise case (Fig. 6.22), the fitting error is under estimated in the presence of drift noise.

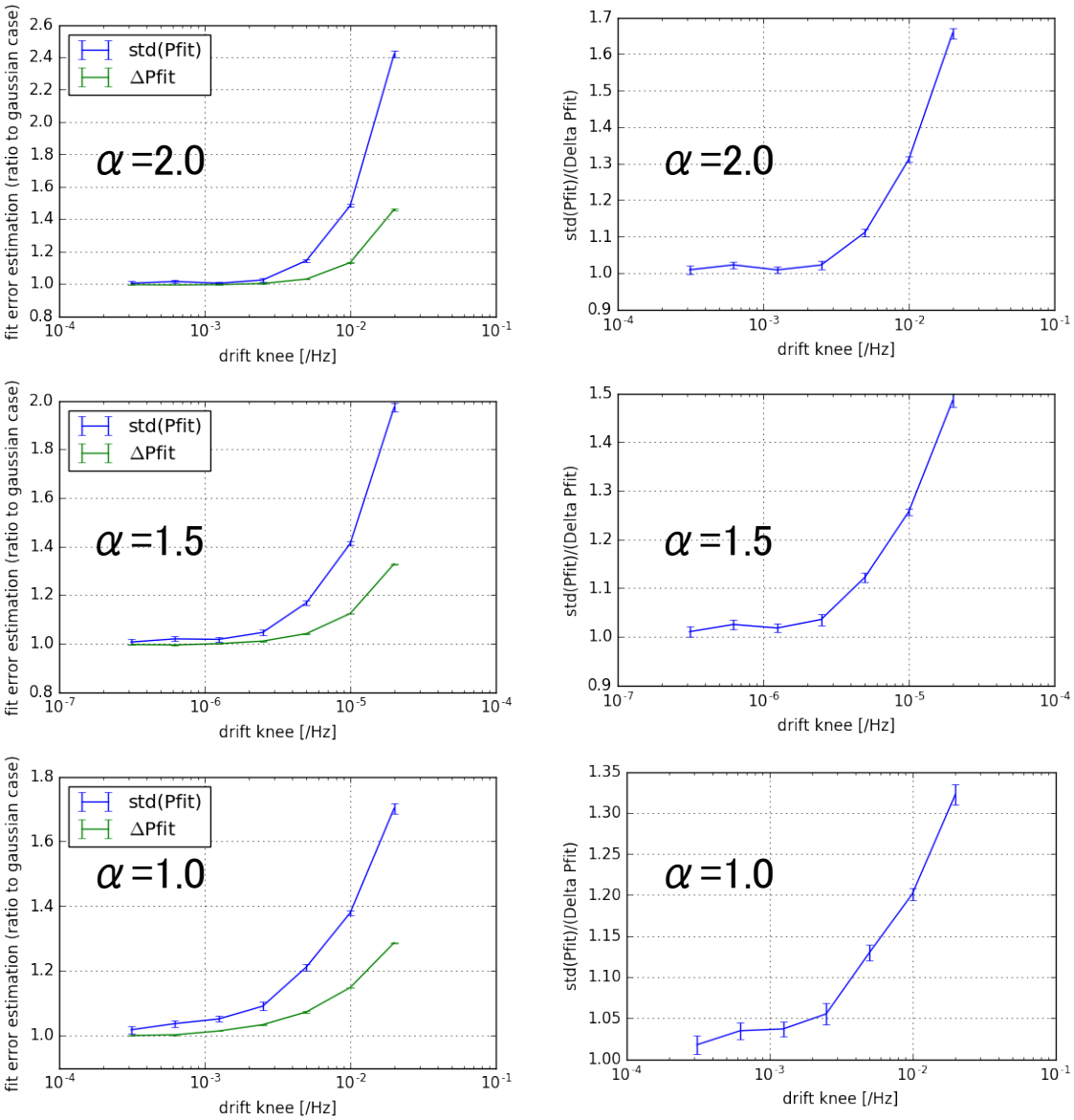

Figure 6.23: The dependence of discrepancy between the distribution of fit result $P_{\rm fit}$ and fitting error $\Delta P_{\rm fit}$, on α knee position of drift noise. The left panels show standard deviation of $P_{\rm fit}$ and average of $\Delta P_{\rm fit}$ in 6 points, whereas the right panels show the ratio of the two. For small α, the discrepancy arises even when knee is low.

6.5 Systematic errors

6.5.1 Flatness of mirror

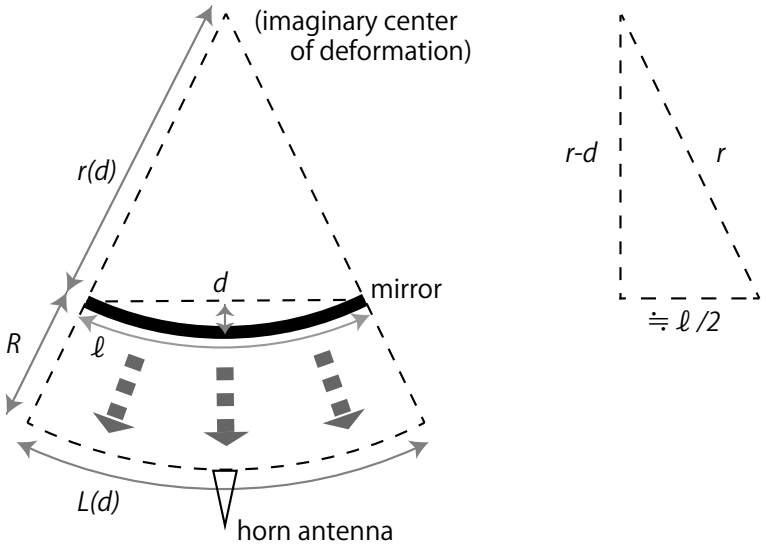

Figure 6.24: Deformation of mirror reduces the collection efficiency of the converted photons. Mirror deforms by d by its weight, changing its shape from line to circular arc.

In our setup, mirror is suspended horizontally at its 4 corners. It can deform by its weight ($\sim$ 4kg). Assuming two dimensional modeling, the deformation is approximately circular arc, as shown in Fig. 6.24. The plane wave from mirror becomes spherical. This weakens the power flux by a factor of $\frac{l}{L}$ in two dimensional model, where l is the width of mirror, and L is some width larger than l (Fig. 6.24). In three dimensional case, this weakening occurs in the two orthogonal directions. Therefore, the collection efficiency is reduced by a factor of $\left(\frac{l}{L}\right)^2$ in our experiment. The radius r of the circular arc is a function of d and l, where d is the deformation at the center of the mirror. L is also a function of d and R, where R is the distance between the mirror and the horn antenna. The deformation d is much smaller than

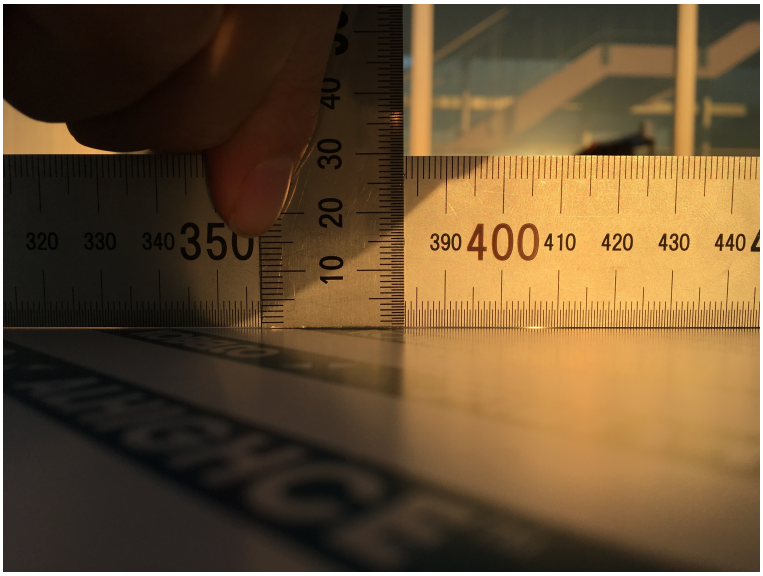

Figure 6.25: The deformation of mirror that we used is small and we conclude it less than 0.5 mm.

l. The dimension of spherical wave is written as follows,

$$r^2 = r^2 - 2rd + d^2 + \left(\frac{l}{2}\right) \tag{6.7}$$

$$\therefore r = \frac{d}{2} + \frac{l^2}{8d}, \tag{6.8}$$

$$\frac{L}{R+r} = \frac{l}{r} \tag{6.9}$$

$$\therefore \frac{L(d=0)}{L(d)} = 1/\left(1 + \frac{R}{\frac{d}{2} + \frac{l^2}{8d}}\right). \tag{6.10}$$

The deformation d of a plate whose both side are supported as modeled in Fig. 6.26 ,

$$\delta = 5Fl^3/384EI, \tag{6.11}$$

$$I = bh^3/12, \tag{6.12}$$

where F is the force which acts uniformly on the plane, I is a value called moment of inertia of area which describes, E is the Young's modulus which is $70.6\times10^9\mathrm{N/m^2}$ for aluminum A5052 we use. Calculating F from the density of aluminum $\rho = 2.68$ g/cm^3 and the constant of gravitational acceleration $g = 9.8$ m/s^2, and substituting $L = 500$mm , we obtain $\delta = 0.15$ mm. As

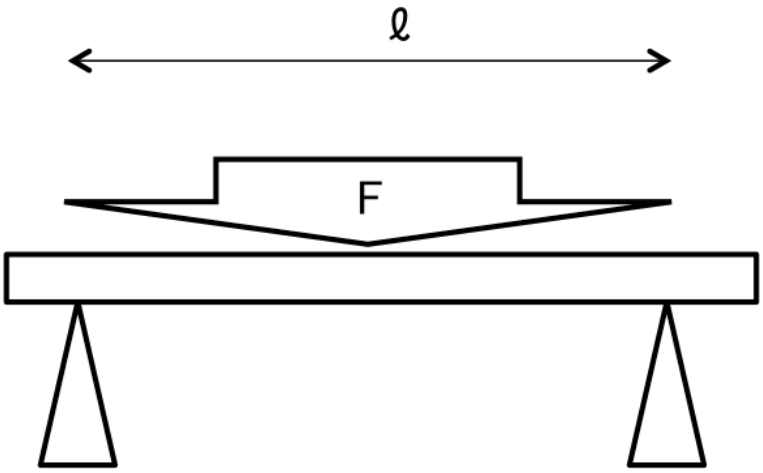

Figure 6.26: Schematic of deformation of a plate

this deformation occurs both direction of mirror, we take twice of this value: $d = 2\delta = 0.29$ mm.

We directly measure the deformation d at the center of mirror. We obtain the upper bound, $d < 0.5$ mm. This is consistent with above calculation (i.e. $d = 0.29$ mm) . We conservatively take $d = 0.5$ mm in our calculation.

Using $R = 1030$mm, $L = 500$ mm, and $d < 0.5$ mm in Eq. (6.7), we obtain the loss of power by mirror deformation is $1 - (L(d = 0)/L(d))^2 < 1.63\%$.

6.5.2 The surface roughness of the mirror

If the plane has some irregularity, it causes a phase error of

$$\delta = 2\pi\frac{\varepsilon}{\lambda}, \tag{6.13}$$

where λ is the wavelength. The effect of this phase error is discussed by Ruze [42, 43]. Assuming the deviation obeys Gaussian distribution of standard deviation σ_δ, the effective power is degraded as

$$P_{\text{eff}} = P_0 e^{-\sigma_\delta^2}, \tag{6.14}$$

$$\sigma_\delta = 2\pi\frac{\sigma_\varepsilon}{\lambda}, \tag{6.15}$$

where P_0 is the total power if there is no phase error.

Roughness of the mirror surface of material is defined by using a parameter R_a as shown in Fig. 6.27. It is the average of the absolute value of irregularity. If the height of surface is $Z(x)$ at position x, it is defined as $R_a = \frac{1}{l_r}\int_0^{l_r} |Z(x)|dx$, where l_r was the length where height is measured along.

Assuming the $Z(x)$ obeys Gaussian distribution $\frac{1}{\sqrt{2\pi}\sigma_\varepsilon}e^{-z^2/(2\sigma_\varepsilon^2)}$, Ra can be converted into σ_ε,

$$R_a = \int \frac{1}{\sqrt{2\pi\sigma}} e^{-x^2/(2\sigma_\varepsilon^2)}|z|dz \tag{6.16}$$

$$= \sqrt{2/\pi}\sigma_\varepsilon. \tag{6.17}$$

We measured the roughness on the surface using a surface roughness measurement machine (SURFCOM, ACCRETECH, Fig. 6.28), as shown in 6.29. The printout of measurement result is shown in Fig. 6.30. We repeated the measurement 4 times and used the worst value. We obtain

$$P_{\text{eff}} = P_0 \times (1 - 9.55 \times 10^{-10}), \tag{6.18}$$

which is negligible effect.

6.5.3 Alignment and the angular dispersion of HPCDM

The beam width of the horn antenna is $\theta_{1/2} = 12.52 \pm 0.05$ deg (Eq. 5.12). The alignment precision of mirror and horn is within 0.03 deg. The plane wave converted from HPCDM itself has angular dispersion of 10^{-3}rad $=$ 0.06deg, from its velocity dispersion $\beta \sim 10^{-3}$. These angular uncertainty corresponds to the loss of $1 - 2^{-0.03/(12.25/2)} = 0.33\%$ and $1 - 2^{-0.06/(12.25/2)} =$ 0.66%, respectively.

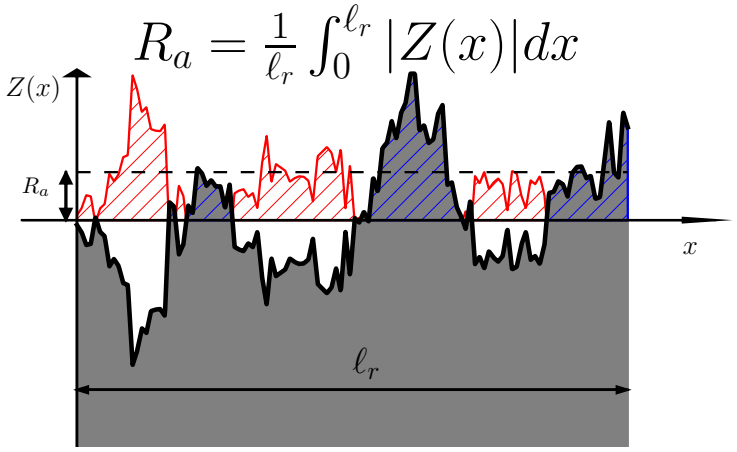

Figure 6.27: Definition of surface roughness parameter R_a. Heights of surface at each location are described by $Z(x)$. R_a is an average of absolute value of distance from average.

6.5.4 Amplifier gain

We used linear model for gain variation as explained in Sec. 5.1. As we selected out data by imposing the systematic bias lower than 7.7%, we conservatively assign the error from responsivity to be 7.7%. The ratio of gains for each of two successive calibrations are summarized in Tab. 6.1.

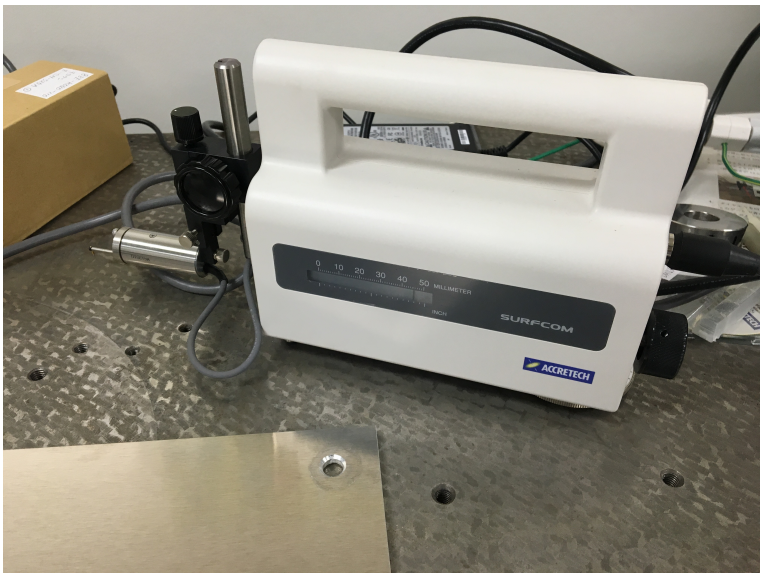

Figure 6.28: The surface roughness measurement machine we used

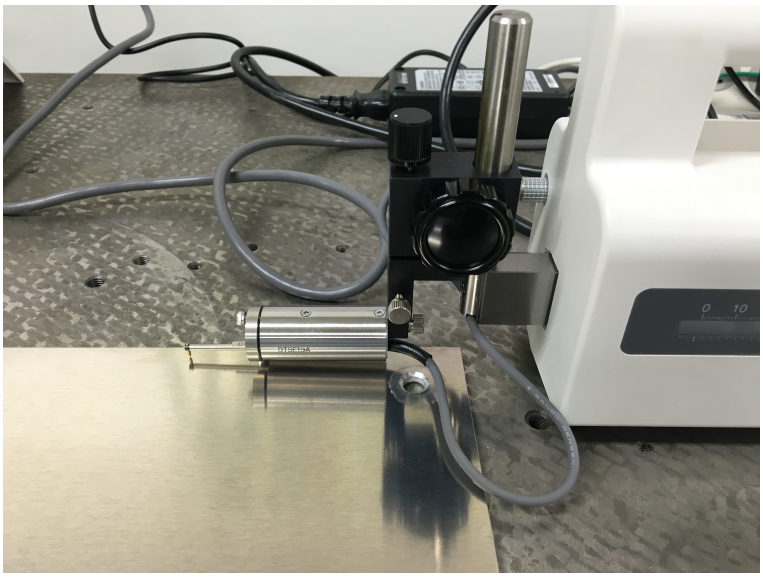

Figure 6.29: The measurement of surface roughness.

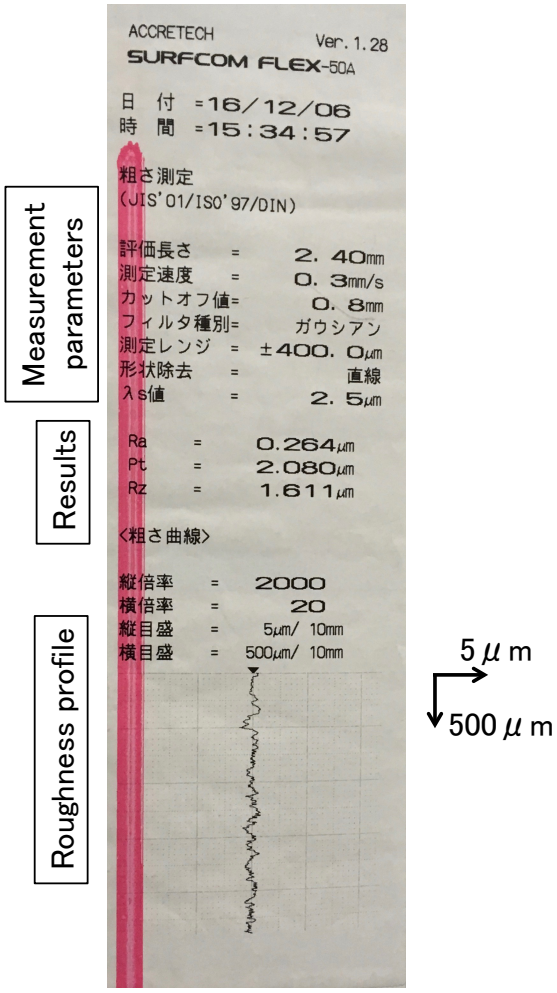

Figure 6.30: The parameters and results of surface roughness measurement. We measured the surface roughness 4 times and used the worst result, i.e. the result of the largest R_a, shown here. The bottom is the plot of roughness profile. The top part shows the measurement parameters. The length measured along (evaluation length) is 2.40 mm, with measurement speed of 0.3 mm/s. A filter of two cutoffs, 2.5 μm and 0.8mm, are applied to obtain the roughness profile. The shape of this filtering is of Gaussian form. The measurement range for the surface roughness is $\pm 400.0 \mu$m. The baseline is linearly detrended. The middle part shows the roughness parameters obtained from the measurement. The parameter $R_a = 0.264 \mu$m is the surface roughness parameter defined in Fig. 6.27. $R_z = 1.611 \mu$m is the difference of the maximum and the minimum point in the roughness profile. $P_t = 2.080 \mu$m is also difference of maximum and the minimum calculated for (instead of roughness profile) primary profile which is obtained applying only the lower cutoff.

6.5.5 Possible fit biases

Pseudo Monte Carlo samples for the bias study

To study biasing from fitting procedure, we prepare Monte Carlo data, in the following steps.

(1). For HPCDM signal, we generate a list of random frequencies according to the distribution, assuming v_E, ν_0 as parameter.

(2). For random noise, we generate a list of random frequencies from uniform distribution.

(3). We make histogram of the frequencies by binning, using the binwidth of 5kHz.

An example of the generated data is shown in Fig. 6.31. To examine the biasing in estimation of signal power P, we specify a specific power $P_{\rm given}$ in generating Monte Carlo data, and take the ratio to the fitting result $P_{\rm fit}$. We used $P_{\rm given} = 10000$ throughout this biasing study. We generated noise of 100 counts per 1 kHz. We used 10 different seeds.

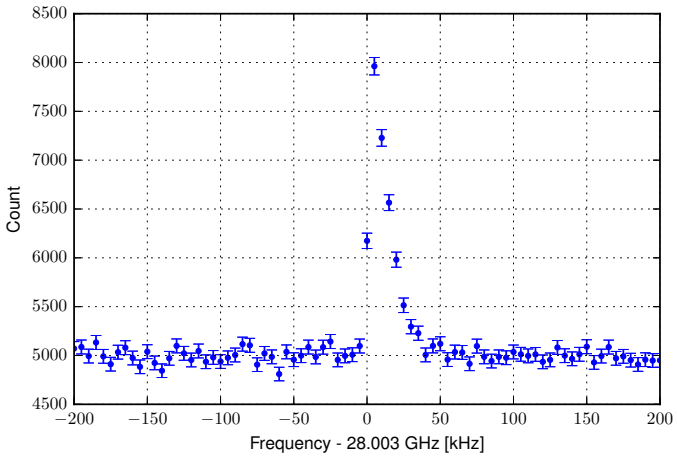

Figure 6.31: The example of signal generated by Monte Carlo, at $\nu_0 = 28.003$ GHz. The generated frequencies are binned 5 kHz.

Effects of frequency bin

As shown in Fig. 6.32, finite frequency resolution of 5 kHz causes the uncertainty. This effect is examined by changing ν_0. We examined this effect by

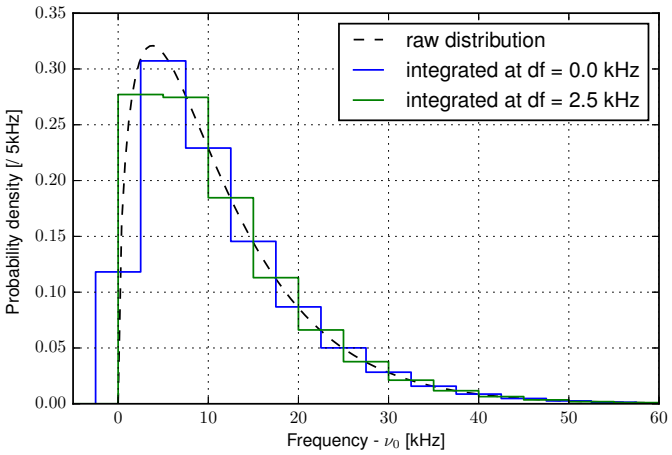

Figure 6.32: The shape of distributions, for different integration starting point.

generating Monte Carlo data of slightly different peak positions. Then, we fit them. Fig. 6.33 shows biases as a function of shift frequency. The P is estimated least when the peak locates the boundary of bins, bias of -4.8%. The green solid line in Fig. 6.32 corresponds it. We conservatively assign this value as one of systematic errors.

Possible instability in frequency response

When frequency response of measurement is instable, the signal would be smeared out and degrading the sensitivity to power P, hence deteriorating sensitivity of the mixing angle χ.

We examined the effect of frequency instability by generating data by Monte Carlo. We add a random variable of uniform distribution of width $f_{\rm blur}$ to the each frequency generated step (1) in 6.5.5. We follow steps (2) (3) unchanged. Examples of blurred signal generated, for $f_{\rm blur}$ =0.1, 0.3, 1.0, 3.0, 10.0, 30.0, 100.0 kHz, are shown in Fig. 6.35.

Fit results with changing seeds are shown in Fig 6.36. We already confirmed blur $<$ 1 kHz in Sec. 5.3. Therefore, the bias is $0.69 \pm 0.58\%$. Their sum of quadrature is conservatively assigned as the systematic error, $\sqrt{0.69^2 + 0.58^2} = 0.90$.

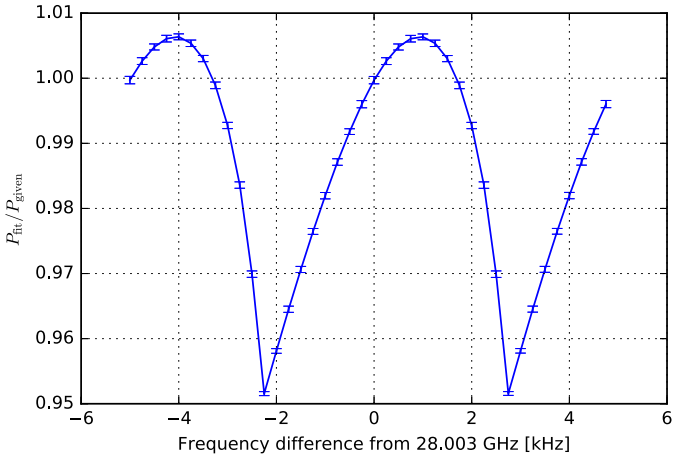

Figure 6.33: The bias in signal power estimation from peak position, relative to 5kHz binning boundaries. The error bar is assigned by standard deviations for 10 different random Monte Carlo seeds. The bias has the same period with the bin width 5 kHz, and largest when the edge of the peak locates at the middle of 5kHz bin boundary (the case shown green in Fig. 6.32) .

6.5.6 Error distribution

Distribution of error potentially causes bias. In particular, upper limit calculation is sensitive to it. It is worthwhile to check if the distribution is consistent with the standard Gaussian distribution. We use null sample for this study of the effect of $P/\Delta P$ distribution for confidence level. We have 2975 fit results $P/\Delta P$ in each null sample. We calculate the 95 % percentile for each null sample. We have 10 null samples by using 10 different seeds. The results for each sample are shown in Fig. 6.37. We estimate the position of 95% level to be $(P\Delta/P) \times (1.658 \pm 0.037)$. This is consistent with Gaussian case. We conservatively assign the systematic error with the ratio of the estimation of this error 0.037 to the value Gaussian case 1.645, 0.037/1.6448 = 2.3 %. This systematic error is also incorporated in our upper limit calculation in chapter 7.

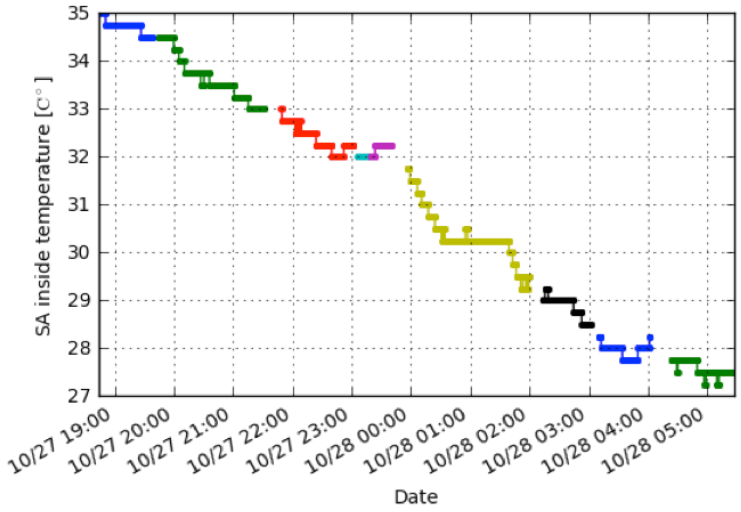

Figure 6.34: The temperature inside the spectrum analyzer during the HPCDM search. The colors corresponds to each run shown in Fig. 6.1. The rate of temperature change is low by more than a magnitude compared to that in frequency precision measurement (Fig. 5.21).

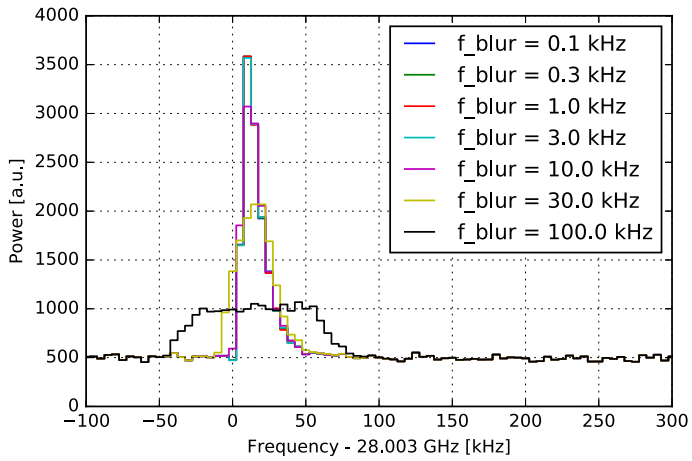

Figure 6.35: The smearing effect of HPCDM peak from blur of various size, made by changing Monte Carlo signal data using a uniform distribution.

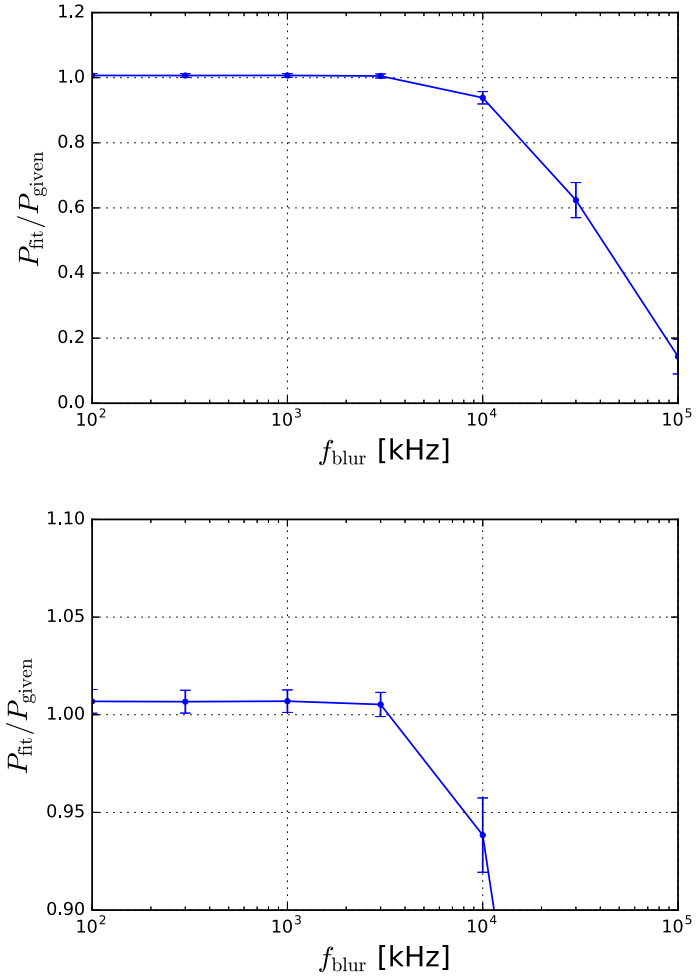

Figure 6.36: The bias in signal power estimation from blur in frequency, obtained by applying fitting procedure to the smeared shapes in Fig. 6.35. The bottom plot is enlarged figure above. In case of $f_{\rm blur} = 1$ kHz, the bias is $0.69 \pm 0.58\%$. Their sum of quadrature is conservatively assigned as the systematic error.

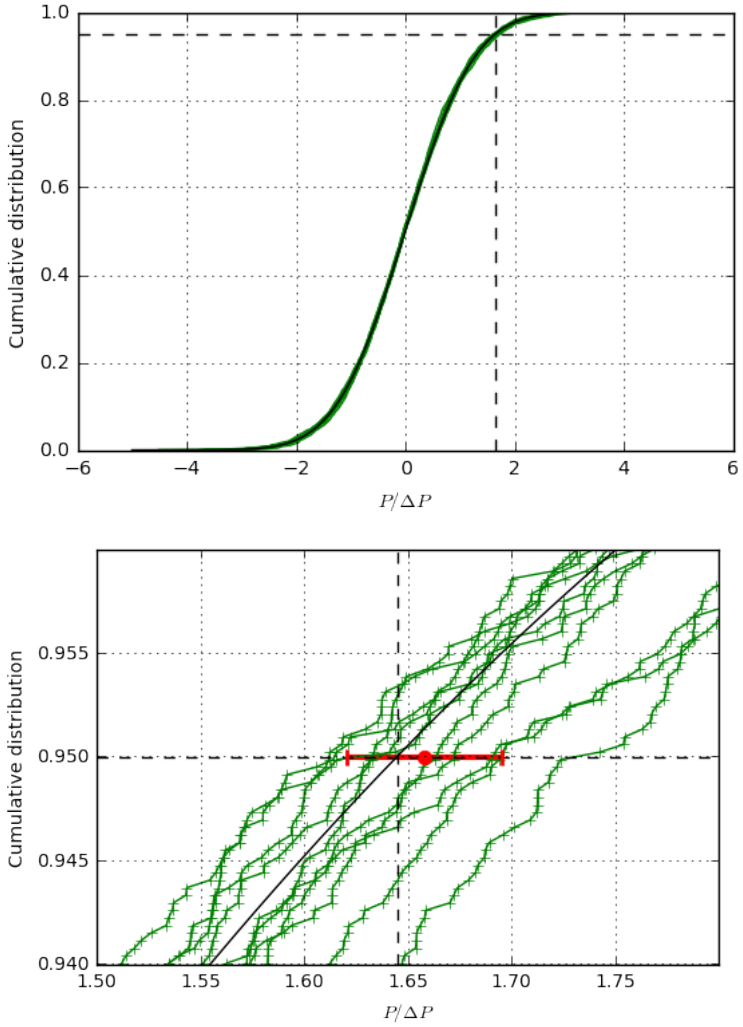

Figure 6.37: The cumulative distribution for Gaussian distribution (black solid line) and null sample results (green). The bottom is enlarged figure. The 95 % percentile of null samples are consistent with the standard Gaussian distribution within 2.3 % precision.

6.5.7 Summary of systematic errors

The systematic error for power of HPCDM signal is summarized in Tab. 6.3. Total uncertainty for the power is $\sqrt{10.8^2 + 1.8^2} = 10.9$ %. Systematic error for error distribution is 2.3 % (Sec. 6.5.6). In case of zero signal hypothesis, we combine these systematic errors. It is 11.0 % for the calculation of 95 % confidence level.

The systematic error for hidden photon mass $m_{\gamma'}$ is negligible: it is 1.2 ppm, (i.e. 1.4×10^{-10} eV) in our scan range.

Source of error	Error [%]	Loss [%]
Mirror flatness		1.6
alignment		0.33
DM angular dispersion		0.67
roughness		9.6×10^{-8}
reflectivity		0.079
Horn antenna ($A_{\rm eff}$)	5.7	
Responsivity (G)	7.7	
Frequency response	0.90	
Binning effects and fit bias	4.8	
Total	10.8	1.8

Table 6.3: Summary of systematic biases for signal power, which affects the sensitivity for HPCDM power P.

Chapter 7

Results and discussion

7.1 The distribution of fit result and rescale factors

As we checked the validity of analysis and sanity of data, we unblinded the data, i.e. conducted fitting procedure described in Sec. 6.2.1. for each of 54 subruns, then combined them. An example of fit for a subrun is shown in Fig. 7.1. We combined results of 54 subruns to obtain final search results. We fit the distribution of $P/\Delta P$ by Gaussian for 9 runs using bins ≥ 10 counts. The example for run 1 is shown in Fig. 7.2. The results for 9 runs are summarized in Fig. 7.3. The result of standard deviation $\sigma = 1.047 \pm 0.005$ indicates the under estimation of error.

The data has drift component. Figure 7.4 shows examples of fit to determine the drift component of subrun. The obtained parameters for all of 54 subruns are summarized in Fig. 7.5. This suggests $\alpha \sim 1.5$ and knee position 10^{-6}–10^{-5} Hz^{-1}, consistent with 5% underestimation of error by drift component (the middle panel of Fig.6.23).

This underestimation of 5% is corrected by the weighted average procedure. Figure 7.6 shows the rescaling factor S. There exist a region where 9 data is combined, one where 18 data is combined, and one where 27 data is combined. The distributions of S is common within each of these regions, and shown in Fig. 7.7–7.9.

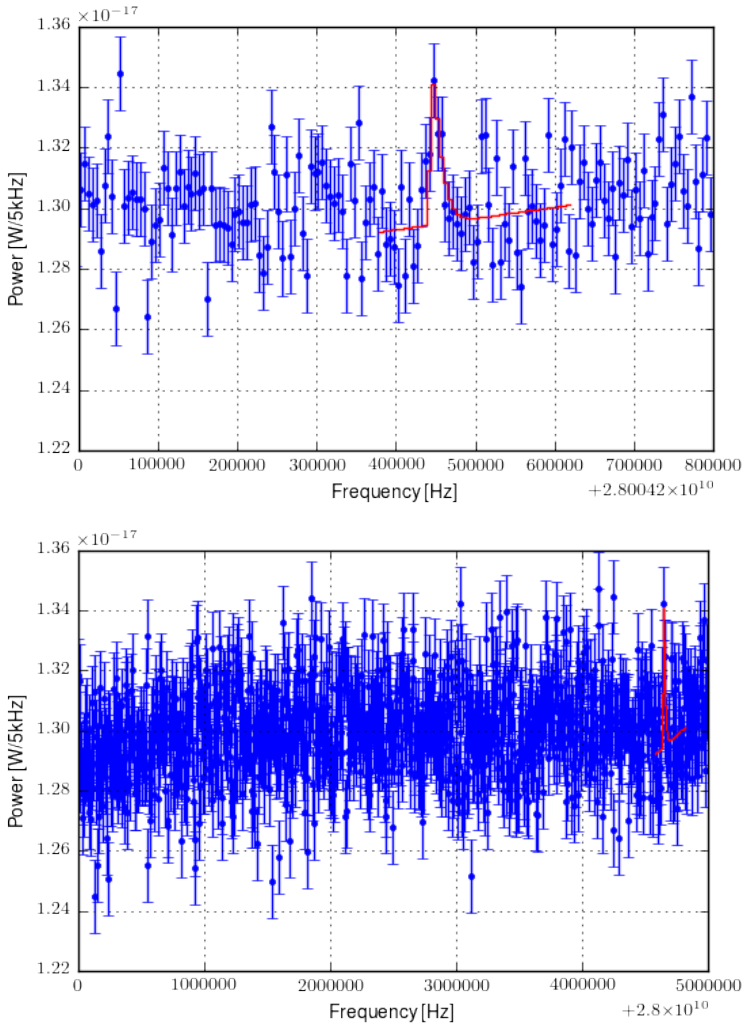

Figure 7.1: An fitting result for subrun 1 (run 1, frequency region 1). The top panel shows the zoom up around fitting region, and the bottom panel shows the position of fit range in the entire subrun 1 data.

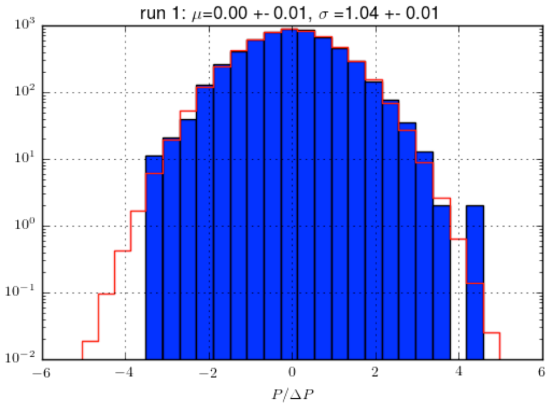

Figure 7.2: The distribution of $P/\Delta P$ of run 1 (subrun 1 to 6). Blue histogram shows the data, and the red solid line shows the result of fit by Gaussian using bins with ≥ 10 counts. The mean $\mu = 0.00 \pm 0.01$ is consistent with zero, whereas the standard deviation $\sigma = 1.04 \pm 0.01$ is larger than one.

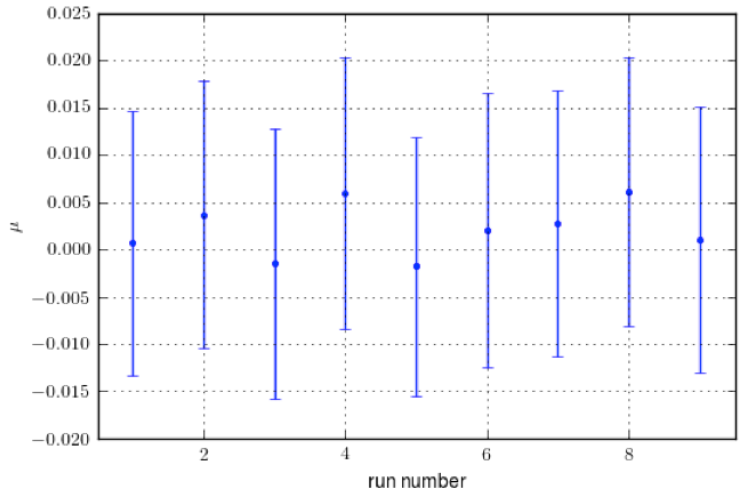

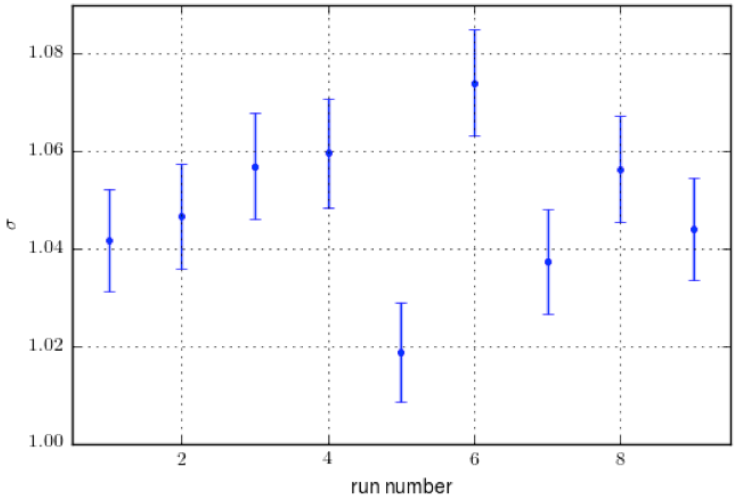

Figure 7.3: The distribution of $P/\Delta P$ for each of 9 runs. The mean $\mu = 0.002 \pm 0.004$ is consistent with zero, whereas the standard deviation $\sigma = 1.047 \pm 0.005$ is larger than one by 5 %, indicating underestimation of error.

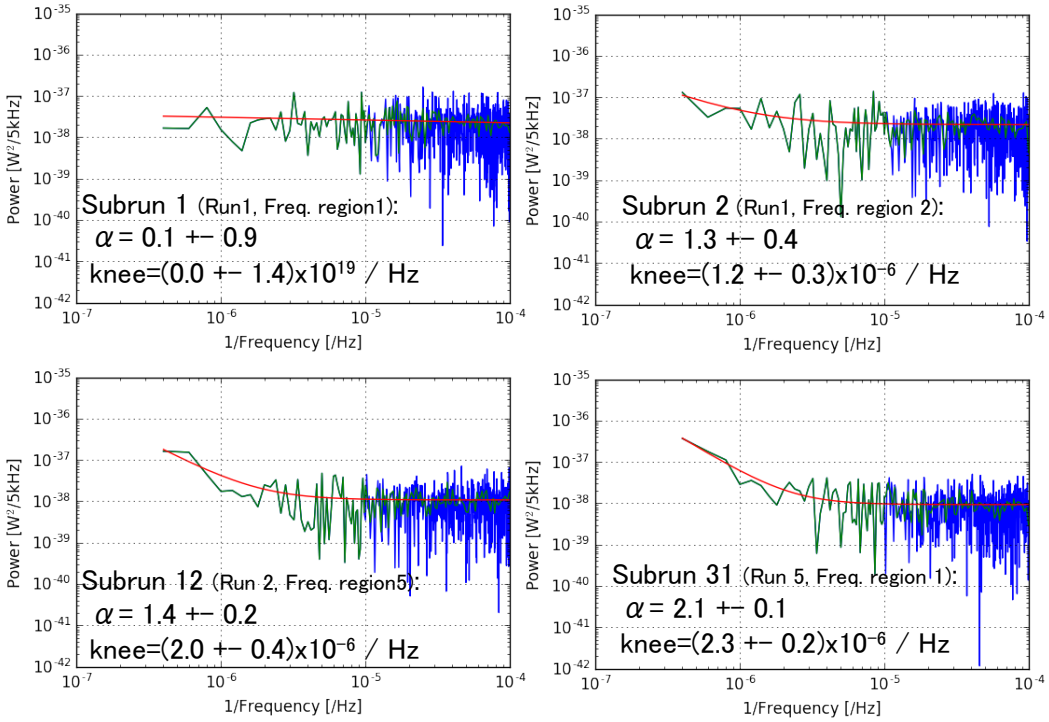

Figure 7.4: Examples of fit result of subruns to obtain the parameters of drift component. The blue curve shows the data of subrun in Fourier space, and Green shows averaged curve to be smooth. The red curve shows fit result.

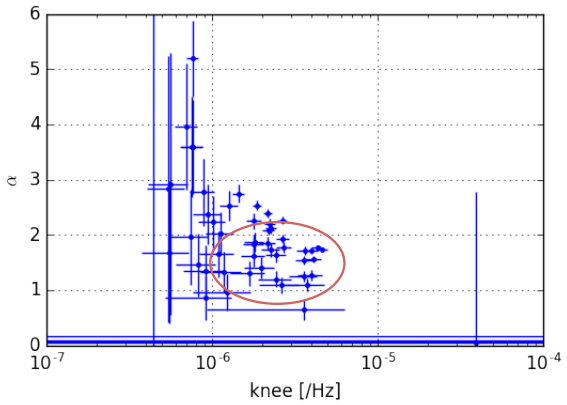

Figure 7.5: The distribution of parameters of drift component for 54 subruns. The region with small error suggests $\alpha \sim 1.5$ and knee position 10^{-6}–10^{-5} Hz^{-1}, consistent with 5% underestimation of error by drift component (the middle panel of Fig.6.23).

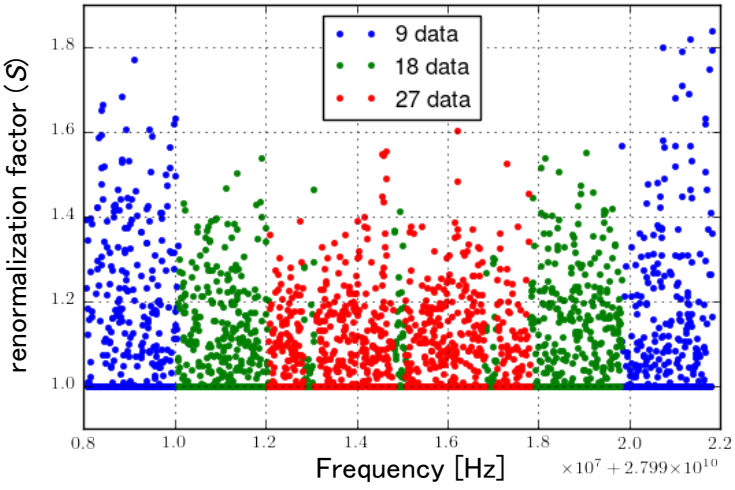

Figure 7.6: The rescaling factors, with different color corresponding different number of subruns to be combined (see Fig. 4.3).

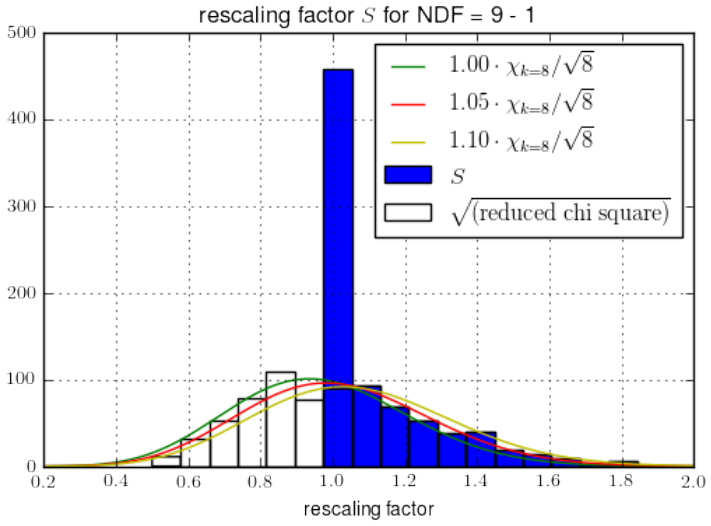

Figure 7.7: The distribution of rescaling factor S (blue histogram) in the region where 9 results are combined (blue in Fig. 7.6). The transparent histogram shows the rescaling factor without clipping at 1 as in Fig. 6.5. The solid curves shows the chi distributions. The curve with 1.05 % (red, 5% under estimation of error) well describes the distribution.

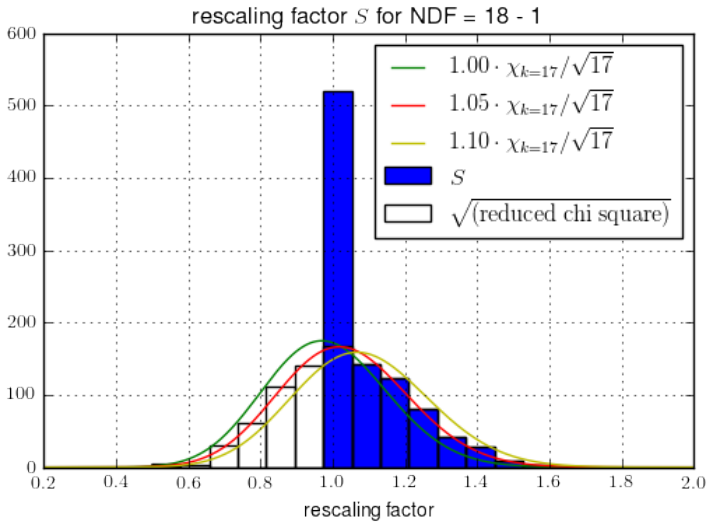

Figure 7.8: The distribution of rescaling factor S (blue histogram) in the region where 18 results are combined (green in Fig. 7.6). The transparent histogram shows the rescaling factor without clipping at 1 as in Fig. 6.5. The solid curves shows the chi distributions. The curve with 1.05 % (red, 5% under estimation of error) well describes the distribution.

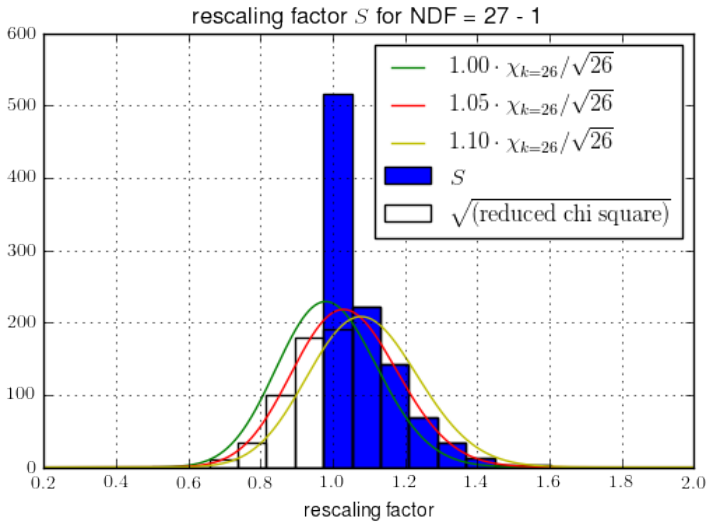

Figure 7.9: The distribution of rescaling factor S (blue histogram) in the region where 27 results are combined (red in Fig. 7.6). The transparent histogram shows the rescaling factor without clipping at 1 as in Fig. 6.5. The solid curves shows the chi distributions. The curve with 1.05 % (red, 5% under estimation of error) well describes the distribution.

7.2 Search results

The search results are shown in Fig. 7.10. No significant excess is found. Figure 7.11 shows $P/\Delta P$ distribution. This is well consistent with the Gaussian distribution as confirmed in the null tests. Consistency with the null tests are also shown in Fig. 7.12.

Local p-values for seven samples in 2752 frequency bins exceed 3σ while the expectation assuming Gaussian distribution is 3.71 samples: 3.03σ, 3.05σ, 3.21σ, 3.46σ, 3.69σ, 3.70σ, 3.88σ for each. They are shown in Fig. 7.14–7.18. The count obeys Possion statistics. The survival function of Poisson distribution with $\lambda = 3.71$ gives a probability for 7 events or more to exceed (PTE) 3σ,

$$\sum_{k=7}^{\infty} \lambda^k e^{-k}/k! = 0.0359. \tag{7.1}$$

This is at most 2.10σ significance for the case of null signal. For the sample with the largest local p-value (3.88σ i.e., $p_{\rm local} = 7.67 \times 10^{-5}$), PTE is

$$1 - (1 - p_{\rm local})^{2752} = 0.19,$$

which corresponds to 0.88σ significance. We also check the $P/\Delta P$ distribution is consistent with null sample results(Fig. 7.12 and 7.13). We confirm that the error distribution is consistent with the analysis validation of the null tests. We conclude there is no significant excess from zero-signal hypothesis.

7.3 Upper limits

As described in 2.4.1, the sensitivity to χ is written in following formula,

$$\chi_{\rm sens} = 4.5 \times 10^{-14} \left(\frac{P_{\rm DM}}{10^{-23}{\rm W}}\right)^{\frac{1}{2}} \left(\frac{0.3{\rm GeV/cm^3}}{\rho_{\rm HP}}\right)^{\frac{1}{2}} \left(\frac{1{\rm m^2}}{A_{\rm eff}}\right)^{\frac{1}{2}} \left(\frac{\sqrt{2/3}}{\alpha}\right). \tag{7.2}$$

We assume HPCDM comprises the entire part of dark matter ($\rho_{\rm HP} = \rho_{\rm DM}$). We use value $\rho_{\rm CDM,local} = 0.39$ GeV/cm^3 as quoted in Chap. 2.1. The calibration in 5.2.4 gives the effective area, $A_{\rm eff} = 1.48 \times 10^{-3}{\rm m}^2$. The evolution of the direction of HPCDM field is parameterized by α (see 2.4.1). We assume the random direction, in which $\alpha = \sqrt{2/3}$. In case of no systematic effect, we would set the 95% confidence upper limit for the power P of HPCDM by

$$P_{\rm limit} = \max(0, P) + 1.65\Delta P. \tag{7.3}$$

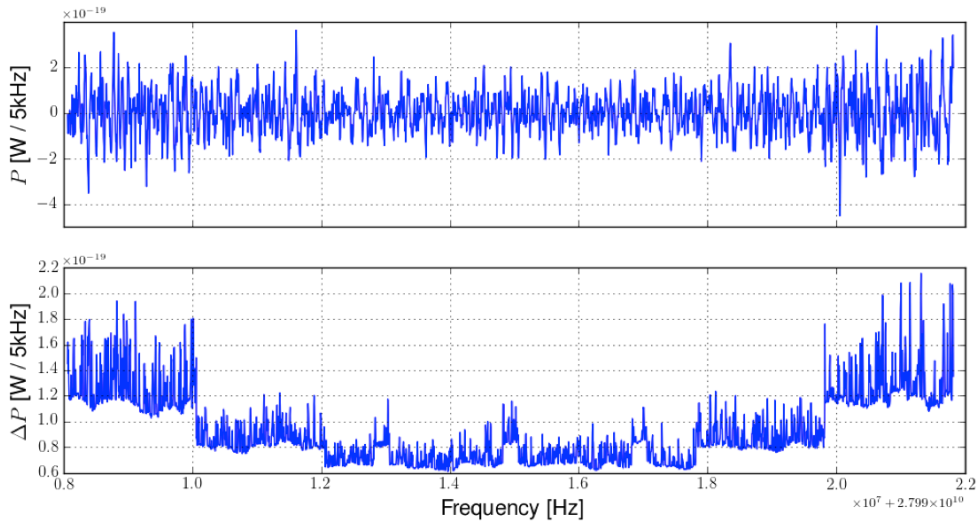

Figure 7.10: The combined results of 54 sub-runs. No significant power is observed in 2752 frequency bins. The level of ΔP reflects of difference of statistics from overwrapping of frequency range (Fig. 4.3)

We have to multiply the power of factor two because the antenna receives only one polarizations of two,

$$P_{\mathrm{DM}} = 2 \times P_{\mathrm{limit}}. \tag{7.4}$$

We set 95 % confidence level limits for the mixing angle χ, as shown in Fig. 7.26 and 7.27). Here, we incorporate the systematic uncertainty of 11 % which is summarized in which is summarized in Sec. 6.5.7. The limits are $\chi < 1.54 - 3.9 \times 10^{-10}$ at the mass range between 115.79 μeV and 115.84 μeV.

7.4 Discussion and future prospects

The low noise level of 200 K effective thermal load enabled us to reach an unprecedented sensitivity, despite small effective area and short measurement time. This was realized by combining techniques for low noise instruments for astronomical observation, and also by the setup of using the blue sky as background.

As prospects, larger A_{eff} will greatly increase the available parameter space. By using a optics of effective area 1 m^2 would increase sensitivity to χ by a factor of $(1\mathrm{m}^2 \ / \ 1.48 \times 10^{-3}\mathrm{m}^2)^{\frac{1}{2}} = 26$. Broadening the search frequency span from 14 MHz to 10 GHz diminishes the sensitivity by a factor

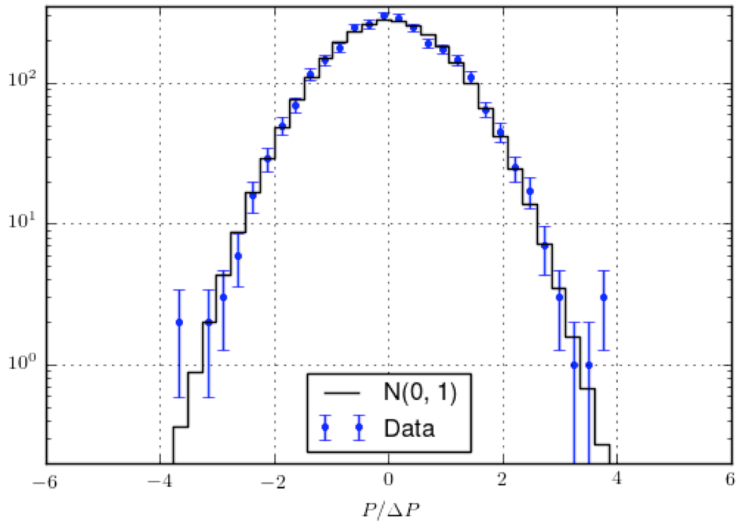

Figure 7.11: The $P/\Delta P$ distribution for fit results in Fig. 7.10. It is fitted with Gaussian distribution $N(\mu, \sigma)$ using bins with ≥ 10 counts, and obtained results is consistent with standard Gaussian distribution: $\mu, \sigma = -0.01 \pm 0.02, 1.00 \pm 0.02$.

of $(10\text{GHz}/14\text{MHz})^{1/4} = 2.9$. Together we can search a 10 GHz span, without changing total measurement time, with sensitivity increase of a factor 8.9, as shown in Fig. 7.28. We can extend the mass region by changing the specifications for the detection frequency. For example, a cassegrain reflector antennas of diameter 1.22 m is commercially available for 18 – 110 GHz[44]. We, however, have to study the effect of near field effect for this case. for diameter $\sim$ 1 m, the far field condition requires the distance between mirror and the antenna $d > 2D^2/\lambda = 200$m, which is not realistic. Instead we can use a lens of 30 cm diameter (which is also commercially available), for which the far field condition requires $d > 2D^2/\lambda = 18$ m, which is easier to realize. The similar experimental approach will cover up to 10^{-3} eV region in future.

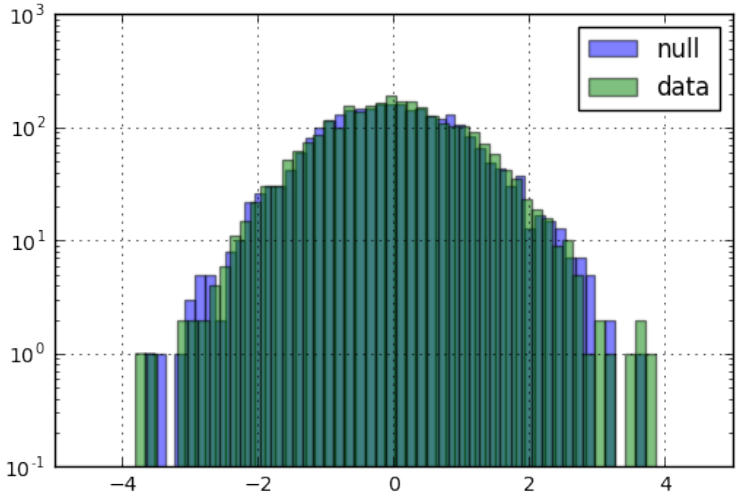

Figure 7.12: The comparison of $P/\Delta P$ for null sample and data. In Sec. 6.3.1 we observed that, the $P/\Delta P$ distribution from null sample is consistent with the standard Gaussian distribution. We check the difference between the distribution for data and null sample. We see no apparent discrepancy in the two distributions.

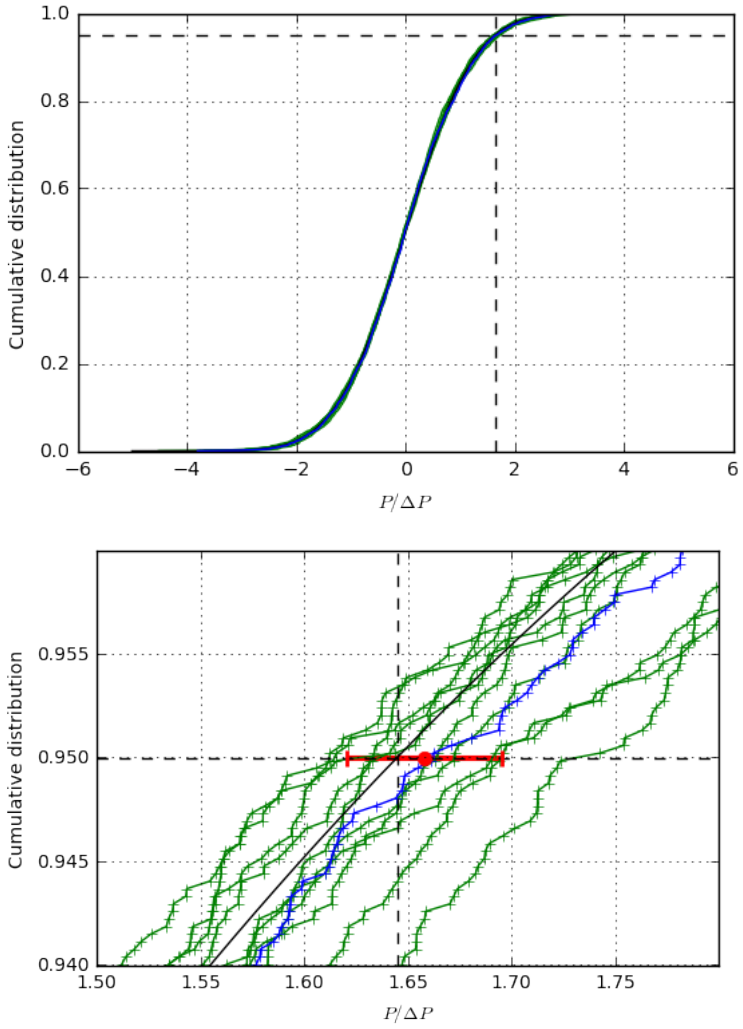

Figure 7.13: The same cumulative distribution of Fig. 6.37, but also the cumulative distribution of the result is shown in blue. The 95% percentile is consistent with Gaussian case (black), within the error estimated with Gaussian (red). We can see the 95 % percentile is consistent with the result for null sample result. They are zoomed up in Fig. 7.15–7.18.

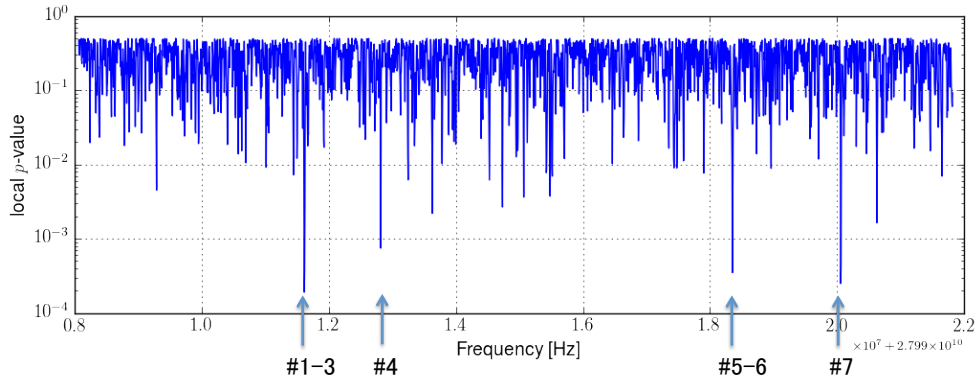

Figure 7.14: The distribution of local p-values. The position of 7 peaks exceeding 3σ significance is also designated.

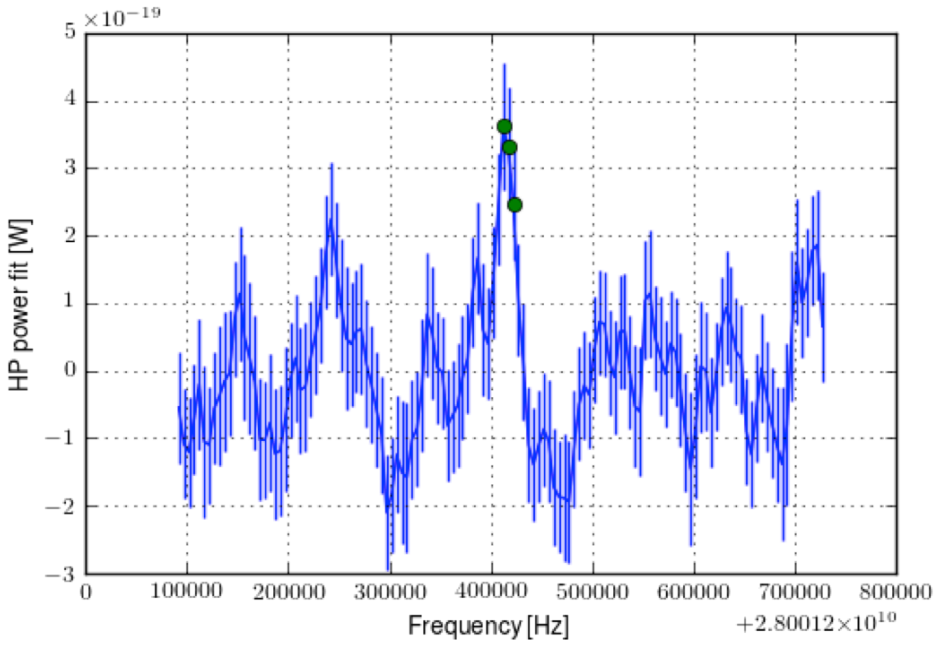

Figure 7.15: The peak #1 – 3 of 7 peaks exceeding 3σ (green circle). These are adjacent to each other.

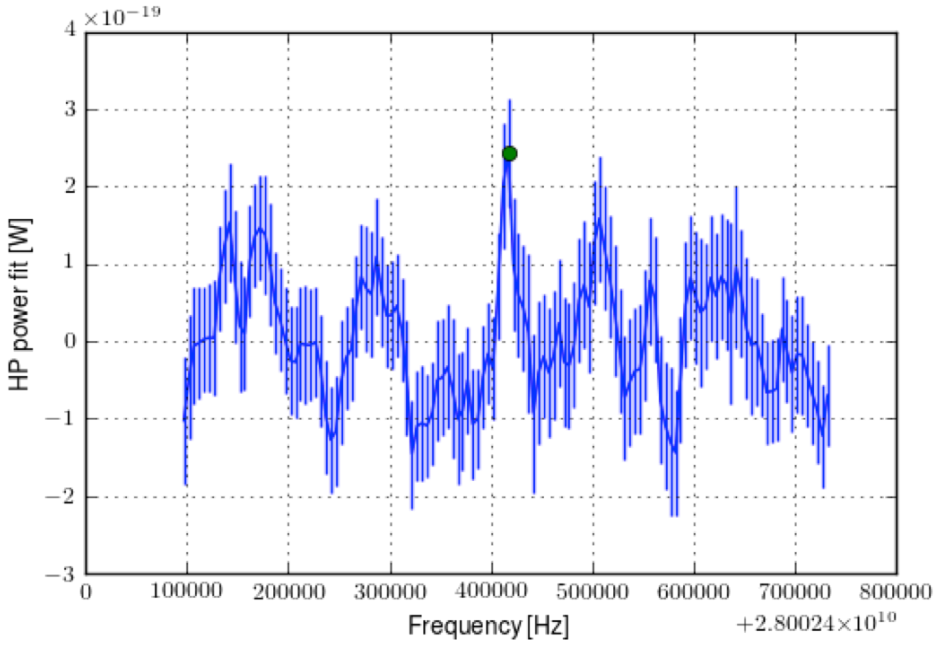

Figure 7.16: The peak #4 of 7 peaks exceeding 3σ (green circle).

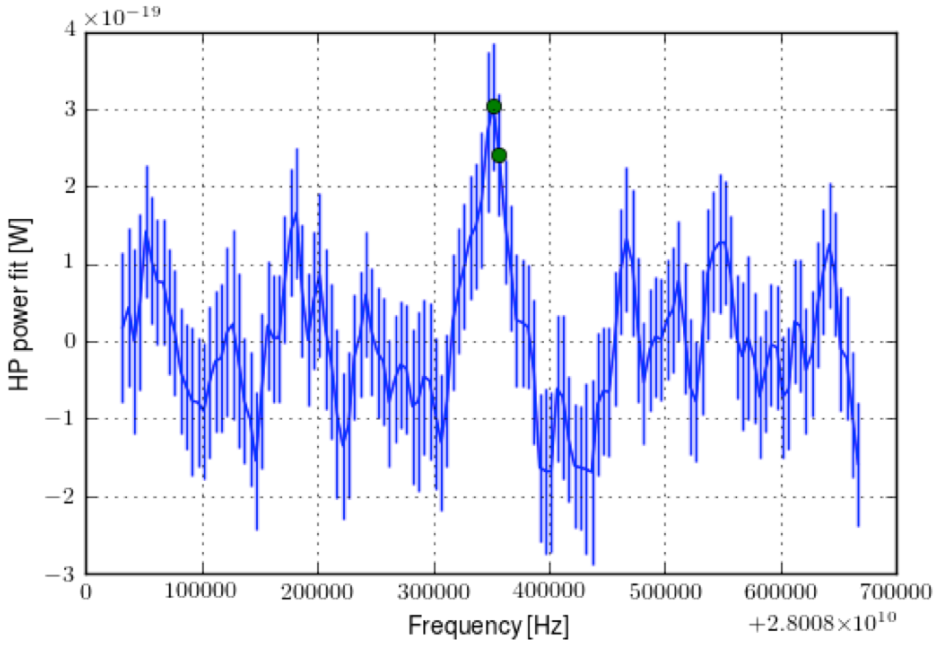

Figure 7.17: The peak #5 and #6 of 7 peaks exceeding 3σ (green circle). These are adjacent to each other.

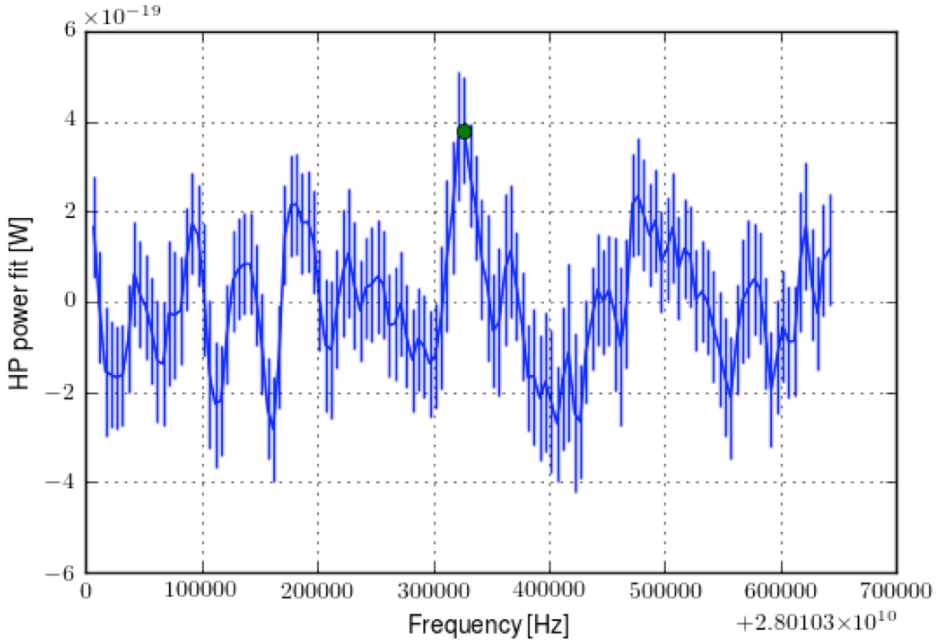

Figure 7.18: The peak #7 of 7 peaks exceeding 3σ (green circle).

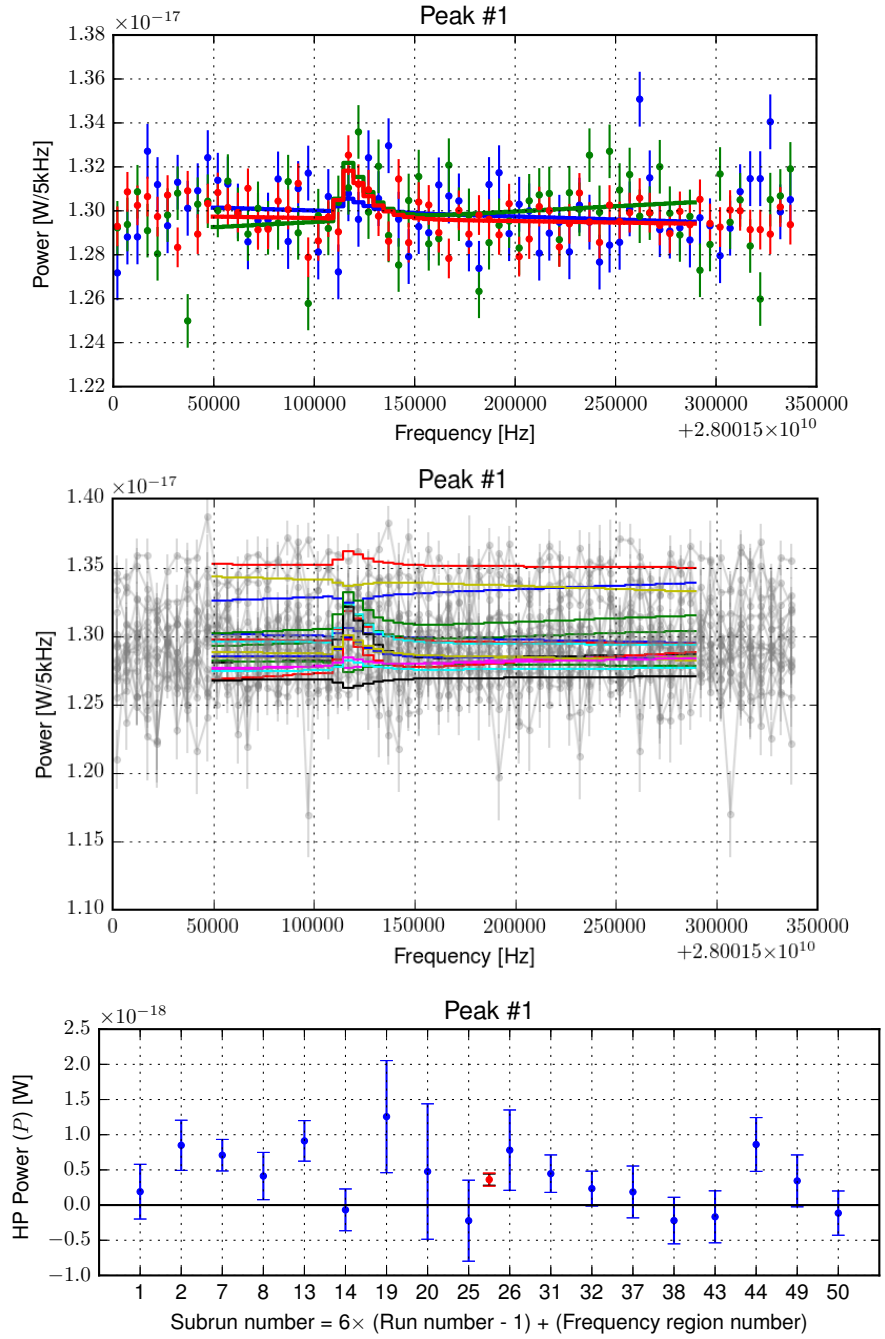

Figure 7.19: The fit results for #1 of 7 peaks exceeding 3σ. The top panel shows the first three subrun data in this frequency region (dot) and fitting results (solid line, the same color as data). The middle panel shows all subrun data in gray, and fit results in colored solid lines. The bottom panel shows fit results P, ΔP for each subrun in blue dots, and combined results in red. The error bar for combined results is rescaled by $S = 1.34$ (the error bar before rescaling is shown in black).

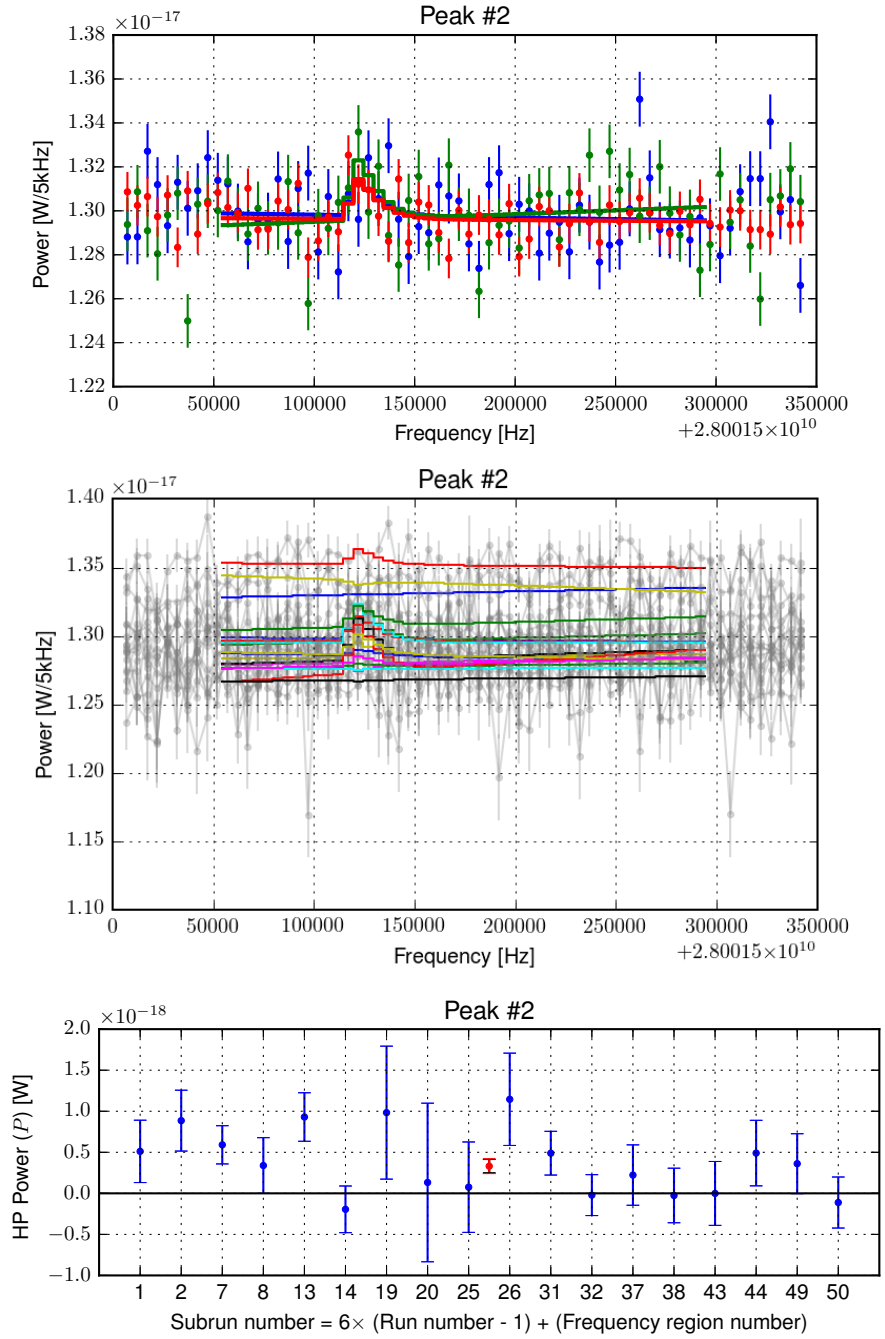

Figure 7.20: The fit results for #2 of 7 peaks exceeding 3σ. The top panel shows the first three subrun data in this frequency region (dot) and fitting results (solid line, the same color as data). The middle panel shows all subrun data in gray, and fit results in colored solid lines. The bottom panel shows fit results P, ΔP for each subrun in blue dots, and combined results in red. The error bar for combined results is rescaled by $S = 1.22$ (the error bar before rescaling is shown in black).

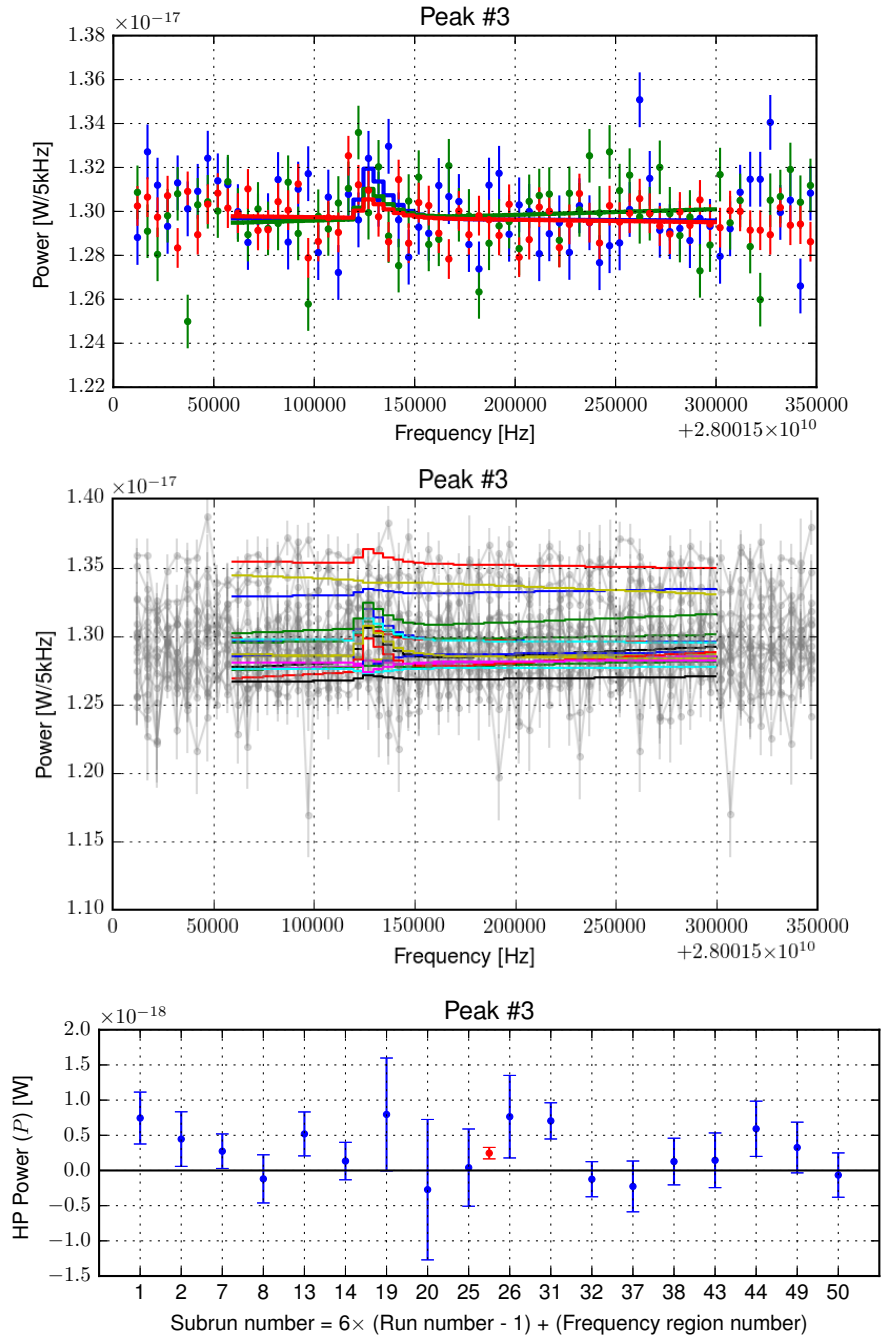

Figure 7.21: The fit results for #3 of 7 peaks exceeding 3σ. The top panel shows the first three subrun data in this frequency region (dot) and fitting results (solid line, the same color as data). The middle panel shows all subrun data in gray, and fit results in colored solid lines. The bottom panel shows fit results P, ΔP for each subrun in blue dots, and combined results in red.

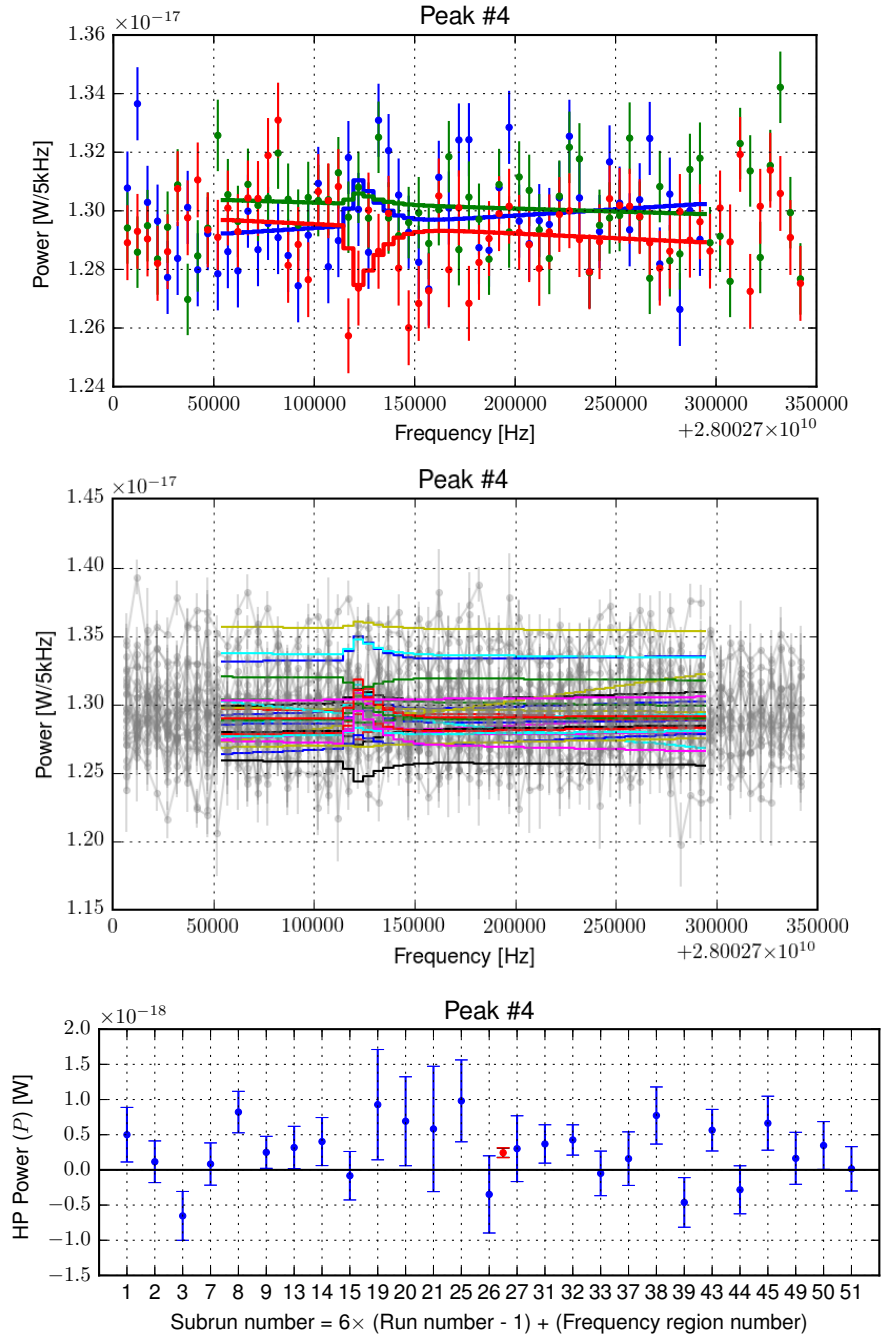

Figure 7.22: The fit results for #4 of 7 peaks exceeding 3σ. The top panel shows the first three subrun data in this frequency region (dot) and fitting results (solid line, the same color as data). The middle panel shows all subrun data in gray, and fit results in colored solid lines. The bottom panel shows fit results P, ΔP for each subrun in blue dots, and combined results in red. The error bar for combined results is rescaled by $S = 1.14$ (the error bar before rescaling is shown in black).

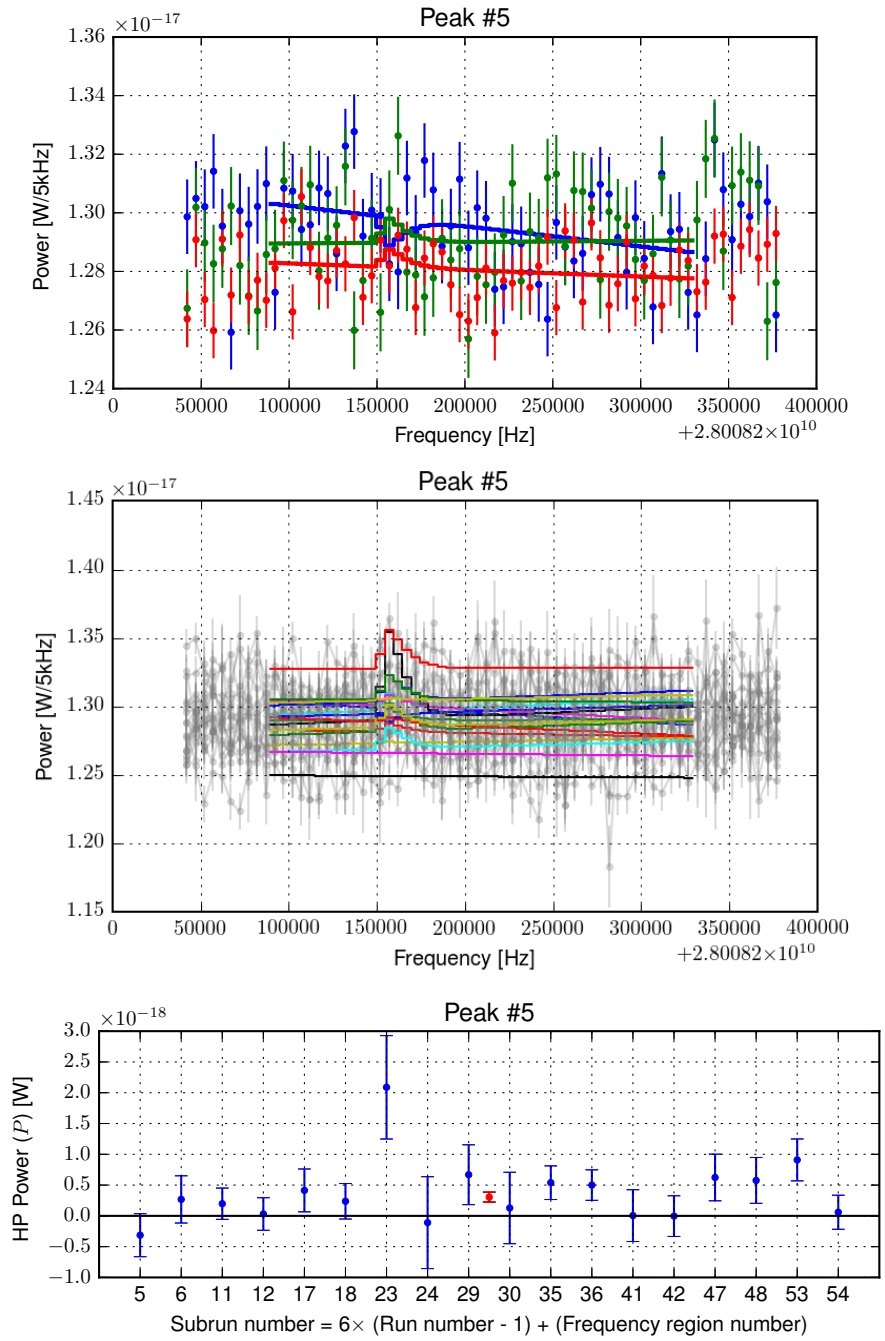

Figure 7.23: The fit results for #5 of 7 peaks exceeding 3σ. The top panel shows the first three subrun data in this frequency region (dot) and fitting results (solid line, the same color as data). The middle panel shows all subrun data in gray, and fit results in colored solid lines. The bottom panel shows fit results P, ΔP for each subrun in blue dots, and combined results in red. The error bar for combined results is rescaled by $S = 1.06$ (the error bar before rescaling is shown in black).

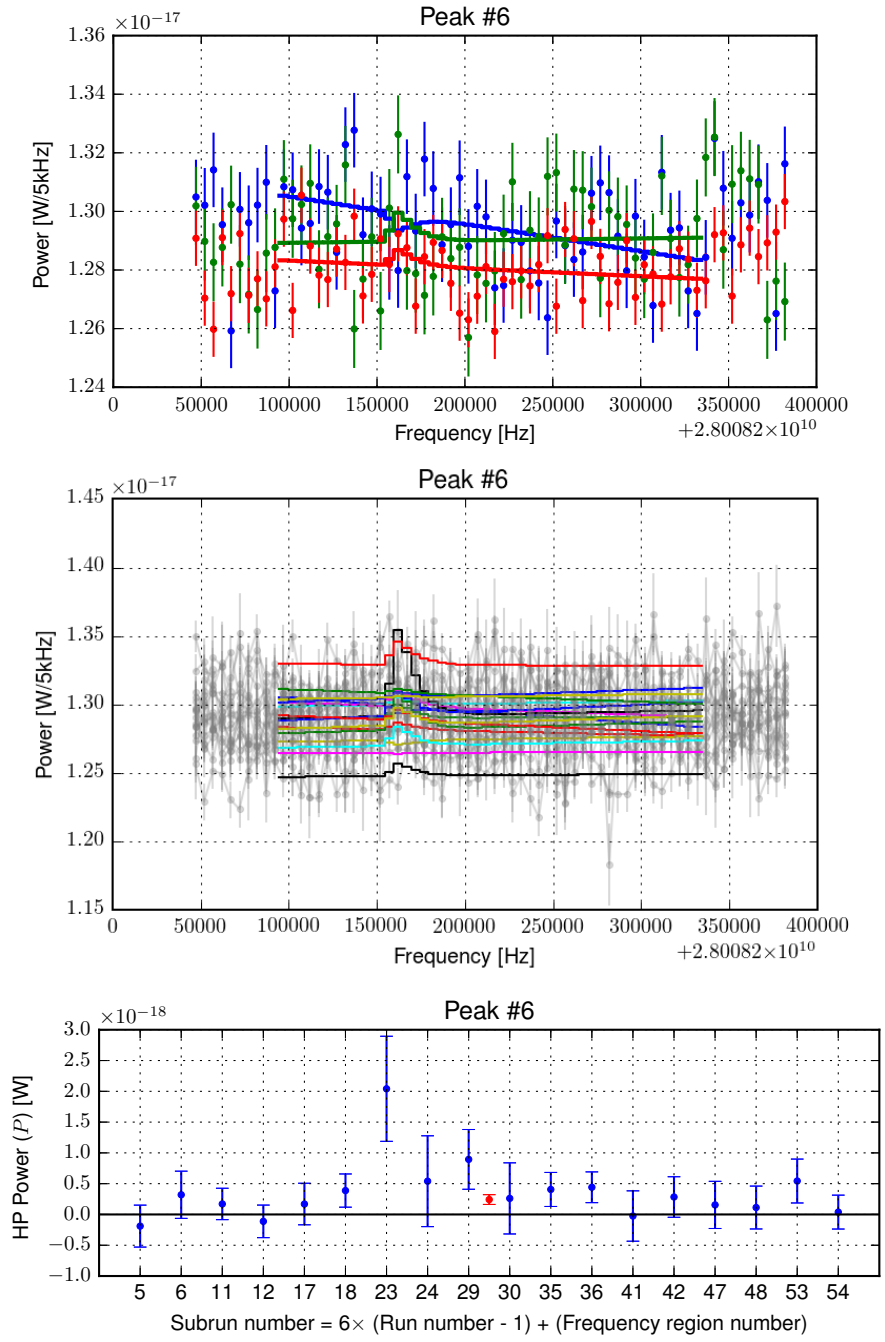

Figure 7.24: The fit results for #6 of 7 peaks exceeding 3σ. The top panel shows the first three subrun data in this frequency region (dot) and fitting results (solid line, the same color as data). The middle panel shows all subrun data in gray, and fit results in colored solid lines. The bottom panel shows fit results P, ΔP for each subrun in blue dots, and combined results in red.

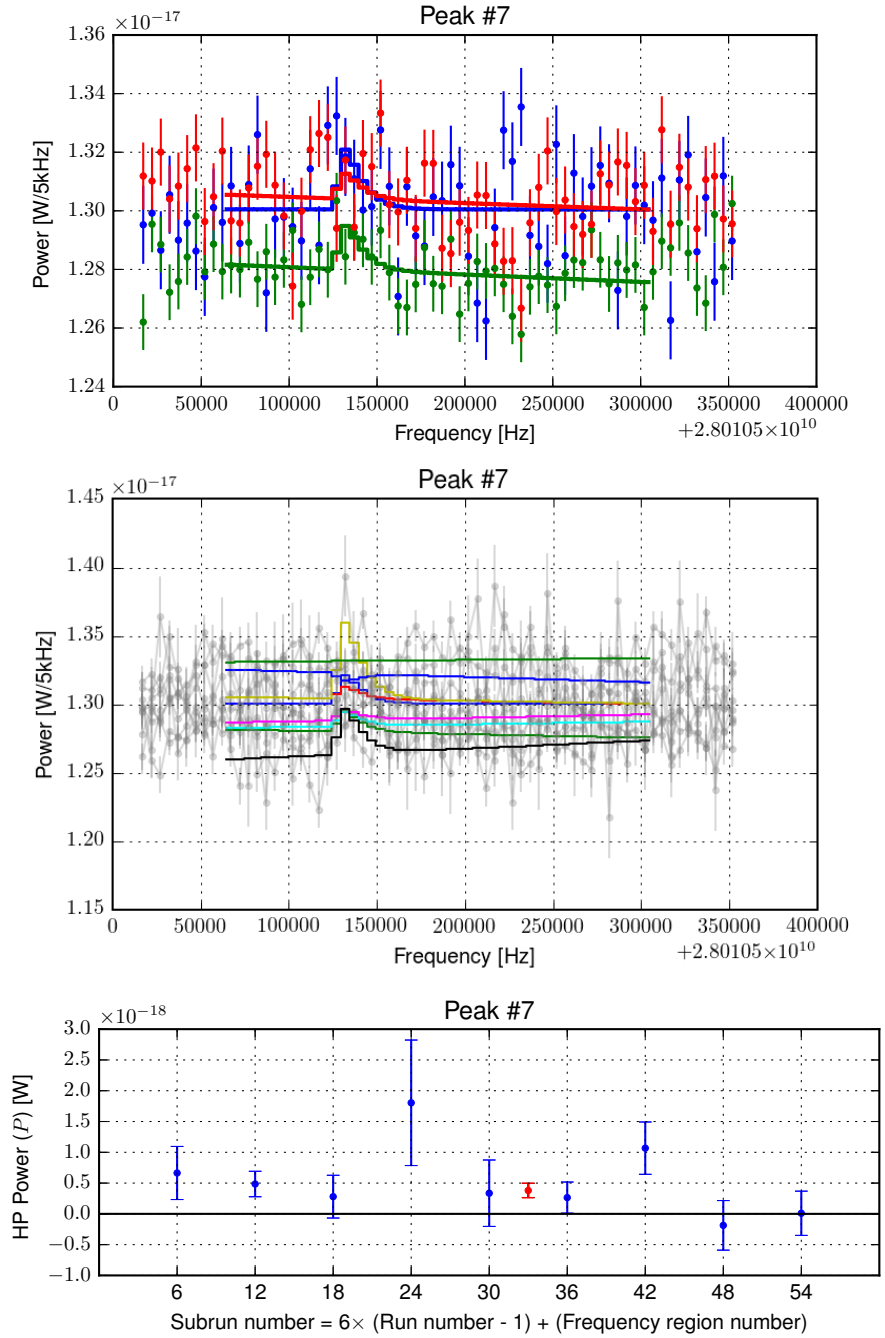

Figure 7.25: The fit results for #7 of 7 peaks exceeding 3σ. The top panel shows the first three subrun data in this frequency region (dot) and fitting results (solid line, the same color as data). The middle panel shows all subrun data in gray, and fit results in colored solid lines. The bottom panel shows fit results P, ΔP for each subrun in blue dots, and combined results in red. The error bar for combined results is rescaled by $S = 1.08$ (the error bar before rescaling is shown in black).

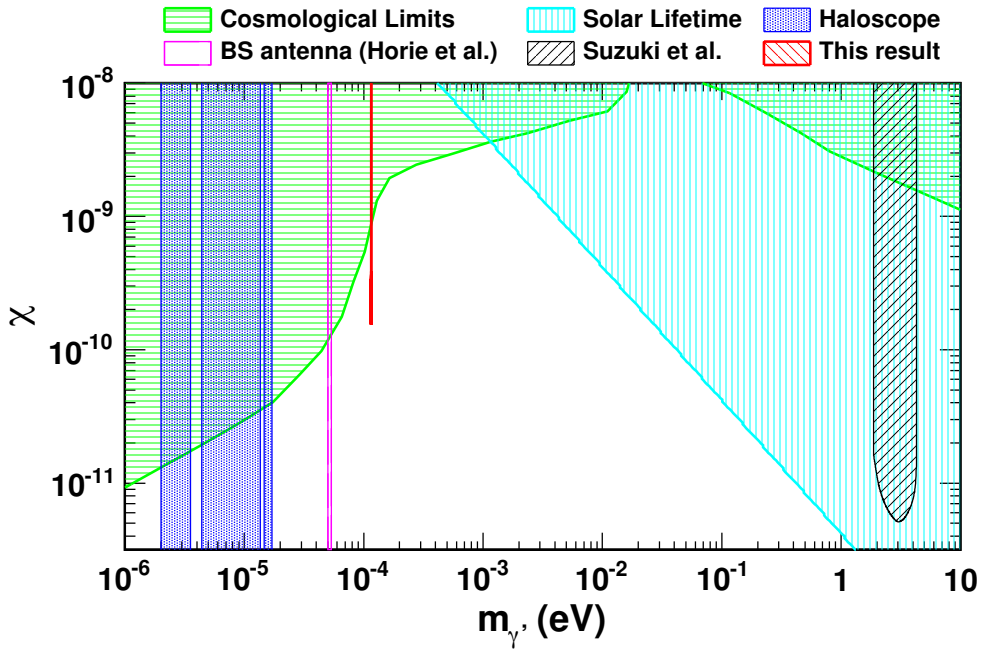

Figure 7.26: The result described in this thesis.

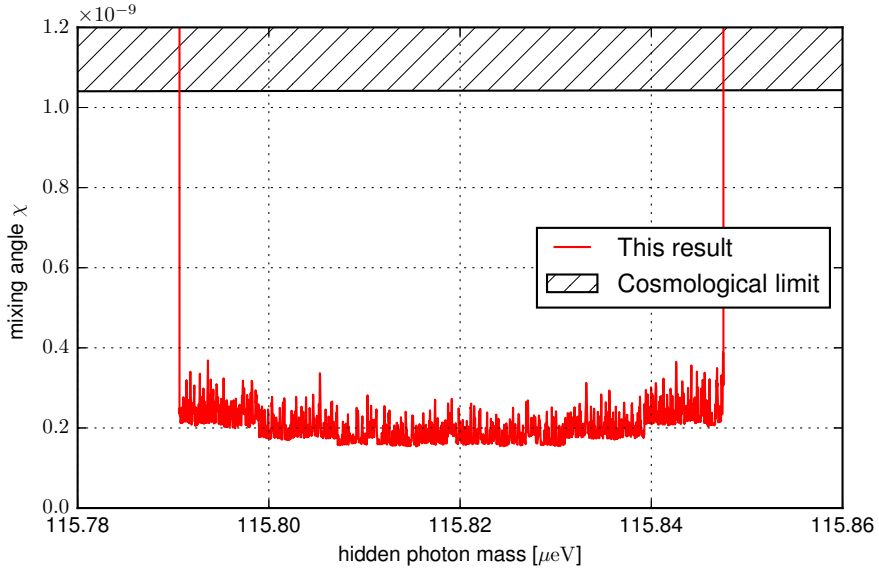

Figure 7.27: The result described in this thesis.

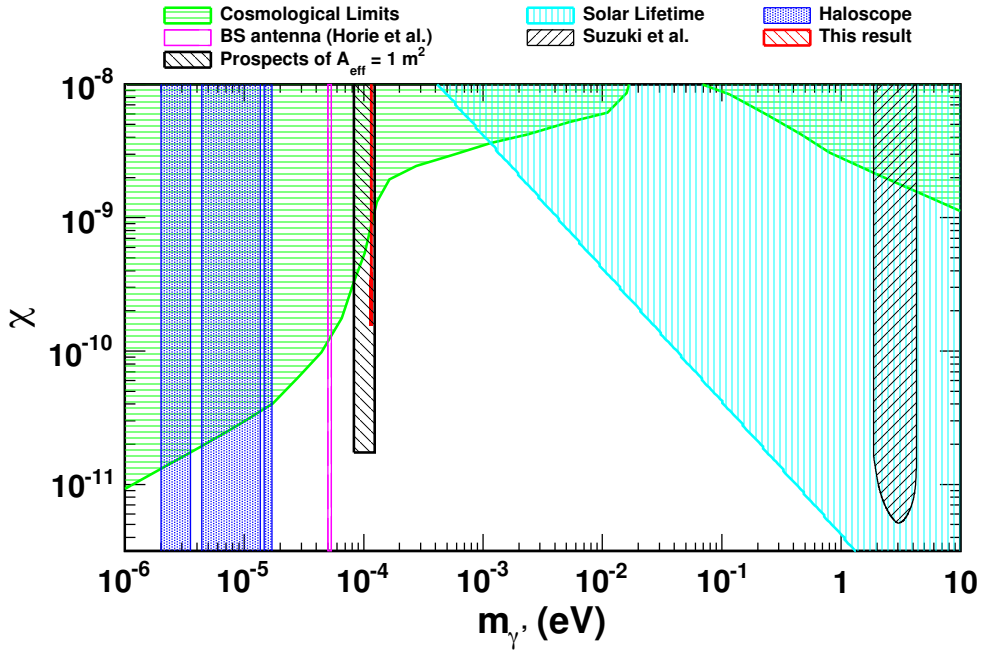

Figure 7.28: Expected sensitivity (black solid, hatched as \\\ ), assuming with optics of $A_{\rm eff} = 1{\rm m}^2$, with the same measurement time $O(1$ day): $\chi = 1.73 \times 10^{-11}$ in mass range 82.7μeV – 124.1 μ eV.

Chapter 8

Conclusions

We search for the hidden photon cold dark matter at the mass region around 10^{-4} eV: 115.79 μeV – 115.84 μeV. This mass range corresponds to 27.998 – 28.012 GHz radio waves for the conversion photon on the surface of the aluminum mirror. The experimental sensitivity to the mixing parameter χ is improved with the fourth root of observation time. It is also improved with the square root of the system temperature of the instruments. We employ the low system temperature setup, and we achieve the sensitivity to search HPCDM below the cosmological constraints. The combination of the cryogenic receiver and the low thermal radiation condition under the atmospheric radiation provides us the low system temperature of 200 K which is about the half of past experiment in close mass region. In data sets of two days with 26 cm^2 aperture, we did not detect HPCDM, and we set the upper limits: $\chi < 1.5$–3.9×10^{-10} at 95% confidence level. This is the most stringent limit to date at this mass region. Our results also give a prospects that the similar instruments with large aperture ($\sim$ 1m^2) improve the sensitivity for χ approximately one order of magnitude. It is also possible to extend the mass region of the search. We establish the experimental method for the particle physics based on the technologies for the radio-astronomy.

Acknowledgment

First of all, I am sincerely grateful to Prof. M. Minowa, who was my supervisor until his retirement. His for advising and encouraging me in a various way. I also deeply thank to Y. Inoue, for critical suggestions and discussions. I'm deeply indebted to Prof. S. Yamamoto for supporting me to continue studying after Prof. Minowa's retirement. I want to deeply thank to Prof. O. Tajima. Without his persistent help this thesis would not have been possible. I am sincerely grateful to T. Nagasaki for useful discussion the about millimeter wave measurements. This work was not possible without his permitting us to diverting KUMODeS for this HPCDM search. I'm deeply indebted to S. Oguri for many discussions and suggestions. I further thank J. Suzuki for useful discussion and suggestions, from his experience in searching for hidden photon. I further thank all members of CMB group at KEK. Finally, I wish to express my deep gratitude to my family.

My research in UTokyo is supported by Advanced Leading Graduate Course for Photon Science (ALPS) at the University of Tokyo. This research is supported by START (Program for Creating STart-ups from Advanced ResearchandTechnology). It was partially supported by Grants-in-Aid for Scientific Research from The Ministry of Education, Culture, Sports, Science, and Technology, Japan (KAKENHI) 16K13809 and 26247045.

Bibliography

[1] P. A. R. Ade *et al.*, "Planck 2013 results. XVI. Cosmological parameters," arXiv:1303.5076.

[2] K. G. Begeman, A. H. Broeils, R. H. Sanders, "Extended rotation curves of spiral galaxies: Dark haloes and modified dynamics," *Mon. Not. Roy. Astron. Soc.* **249** (1991) 523.

[3] K. Olive, "Review of Particle Physics," *Chinese Phys. C* **38** (2014) 090001.

[4] P. Arias *et al.*, "WISPy cold dark matter," *JCAP* **1206** (2012) 013, arXiv:1201.5902.

[5] A. Golovnev, V. Mukhanov, V. Vanchurin, "Vector inflation," *JCAP* **06** (2008) 009, arXiv:0802.2068 [astro-ph].

[6] D. Horns *et al.*, "Searching for WISPy cold dark matter with a dish antenna," *JCAP* **1304** (2013) 016, arXiv:1212.2970 [hep-ph].

[7] J. Suzuki *et al.*, "Hidden photon CDM search at Tokyo," in *11th Patras Work. Axions, WIMPs WISPs Zaragoza, Spain, June 22-26, 2015*. Sep, 2015. arXiv:1509.00785 [hep-ex].

[8] T. Horie, "Experimental search for hidden photon dark matter by using dish antenna method," PhD thesis, The University of Tokyo, 2015.

[9] R. Catena, P. Ullio, "A novel determination of the local dark matter density," *JCAP* **08** (2010) 004, arXiv:0907.0018 [astro-ph.CO].

[10] L. B. Okun, "LIMITS OF ELECTRODYNAMICS: PARAPHOTONS?," *Sov. Phys. JETP* **56** (1982) 502.

[11] B. Holdom, "Two U(1)'s and ϵ charge shifts," *Phys. Lett. B* **166** (1986) 196–198.

[12] K. Ehret, Others, "New ALPS Results on Hidden-Sector Lightweights," *Phys. Lett.* **B689** (2010) 149–155, arXiv:1004.1313 [hep-ex].

[13] J. Jaeckel, A. Ringwald, "The Low-Energy Frontier of Particle Physics," *Annu. Rev. Nucl. Part. Sci.* **60** (2010) 405–437, arXiv:1002.0329 [hep-ph].

[14] M. Schwarz *et al.*, "Results from the Solar Hidden Photon Search (SHIPS)," *JCAP* **08** (2015) 011, arXiv:1502.04490 [hep-ph].

[15] S. Andriamonje *et al.*, "An improved limit on the axion-photon coupling from the CAST experiment," *JCAP* **04** (2007) 010, arXiv:hep-ex/0702006 [hep-ex].

[16] J. Redondo, "Helioscope bounds on hidden sector photons," *JCAP* **07** (2008) 008, arXiv:0801.1527 [hep-ph].

[17] T. Mizumoto *et al.*, "Experimental search for solar hidden photons in the eV energy range using kinetic mixing with photons," *JCAP* **07** (2013) 013, arXiv:1302.1000 [astro-ph.SR].

[18] T. Mizumoto, "Experimental Search for solar hidden sector photons in the eV energy range using kinetic mixing with photon," PhD thesis, The University of Tokyo, 2010.

[19] H. An, M. Pospelov, J. Pradler, "Dark Matter Detectors as Dark Photon Helioscopes," *Phys. Rev. Lett.* **111** (2013) 041302, arXiv:1304.3461 [hep-ph].

[20] I. M. Bloch *et al.*, "Searching for Dark Absorption with Direct Detection Experiments," arXiv:1608.02123.

[21] O. Takachio, "Experimental Search for Hidden-Photon Cold Dark Matter Signatures in the O(10) keV mass range with XMASS-I," PhD thesis, The University of Tokyo, 2015.

[22] H. An, M. Pospelov, J. Pradler, "New stellar constraints on dark photons," *Phys. Lett. B* **725** (2013) 190–195, arXiv:1302.3884 [hep-ph].

[23] J. Redondo, G. Raffelt, "Solar constraints on hidden photons re-visited," *JCAP* **08** (2013) 034, arXiv:1305.2920 [hep-ph].

[24] A. E. Nelson, J. Scholtz, "Dark light, dark matter, and the misalignment mechanism," *Phys. Rev. D* **84** (2011) 103501, arXiv:1105.2812 [hep-ph].

[25] P. W. Graham, J. Mardon, S. Rajendran, "Vector dark matter from inflationary fluctuations," *Phys. Rev. D* **93** (2016) 103520, arXiv:1504.02102v1.

[26] J. Jaeckel, S. Knirck, "Directional resolution of dish antenna experiments to search for WISPy dark matter," *JCAP* **01** (2016) 005, arXiv:1509.00371 [hep-ph].

[27] J. Suzuki, "Experimetal search for hidden photon CDM in the eV mass range with a concave mirror," PhD thesis, The University of Tokyo, 2015.

[28] D. Veberič *et al.*, "Search for dark matter in the hidden-photon sector with a large spherical mirror," in *PoS*, vol. ICRC2015, p. 1191. Sep, 2015. arXiv:1509.02386.

[29] J. Redondo, M. Postma, "Massive hidden photons as lukewarm dark matter," *JCAP* **02** (2009) 005, arXiv:0811.0326 [hep-ph].

[30] J. Jaeckel, J. Redondo, "An antenna for directional detection of WISPy dark matter," *JCAP* **11** (2013) 016, arXiv:1307.7181 [hep-ph].

[31] A. Aguilar-Arevalo *et al.*, "First direct detection constraints on eV-scale hidden-photon dark matter with DAMIC at SNOLAB," arXiv:1611.03066.

[32] P. Arias *et al.*, "Extracting hidden-photon dark matter from an LC-circuit," *Eur. Phys. J. C* **75** (2015) 310, arXiv:1411.4986 [hep-ph].

[33] S. Chaudhuri *et al.*, "Radio for hidden-photon dark matter detection," *Phys. Rev. D* **92** (2015) 075012, arXiv:1411.7382.

[34] K. M. Cudworth, "The Local Galactic Escape Velocity Revisited: Improved Proper Motions for Critical Stars," *Astron. J.* **99** (1990) 590–594.

[35] C. S. Kochanek, "The Mass of the Milky Way," *Astrophys. J.* **457** (1996) 228, arXiv:astro-ph/9505068.

[36] T. Nagasaki *et al.*, "Monitoring System for Atmospheric Water Vapor with a Ground-Based Multi-Band Radiometer: Meteorological Application of Radio Astronomy Technologies," *J. Low Temp. Phys.* **184** (2016) 674–679.

[37] O. Tajima *et al.*, "Sensing of the atmospheric water vapor with millimeter wave spectrometer — KUMODeS," in *2016 Prog. Electromagn. Res. Symp.*, pp. 4157–4161. IEEE, Aug, 2016.

[38] `http://www.millitech.com/MMW-Antenna-StandardGainHorn.htm`

[39] `http://www.data.jma.go.jp/obd/stats/etrn/`

[40] J. Choi *et al.*, "Radio-transparent multi-layer insulation for radiowave receivers," *Rev. Sci. Instrum.* **84** (2013) , `arXiv:1306.5040`.

[41] A. H. Rosenfeld, "The Particle Data Group: Growth and Operations-Eighteen Years of Particle Physics," *Annu. Rev. Nucl. Sci.* **25** (1975) 555–598.

[42] J. Ruze, "Antenna tolerance theory – A review," *Proc. IEEE* **54** (1966) 633–640.

[43] J. Ruze, "The effect of aperture errors on the antenna radiation pattern," *Nuovo Cim.* **9** (1952) 364–380.

[44] `http://www.millitech.com/MMW-Antenna-Cassegrain.htm`